

Doctoral thesis

Doctoral theses at NTNU, 2022:395

Wei Wang

Electromagnetic Field Calculation and Power Loss Evaluation in Power Transformers

Analysis of Leakage Fields and Stray Losses
under Special Operation Conditions

NTNU
Norwegian University of Science and Technology
Thesis for the Degree of
Philosophiae Doctor
Faculty of Information Technology and Electrical
Engineering
Department of Electric Power Engineering



Norwegian University of
Science and Technology

Wei Wang

Electromagnetic Field Calculation and Power Loss Evaluation in Power Transformers

Analysis of Leakage Fields and Stray Losses
under Special Operation Conditions

Thesis for the Degree of Philosophiae Doctor

Trondheim, December 2022

Norwegian University of Science and Technology
Faculty of Information Technology and Electrical Engineering
Department of Electric Power Engineering



Norwegian University of
Science and Technology

NTNU

Norwegian University of Science and Technology

Thesis for the Degree of Philosophiae Doctor

Faculty of Information Technology and Electrical Engineering
Department of Electric Power Engineering

© Wei Wang

ISBN 978-82-326-6658-4 (printed ver.)

ISBN 978-82-326-6345-3 (electronic ver.)

ISSN 1503-8181 (printed ver.)

ISSN 2703-8084 (online ver.)

Doctoral theses at NTNU, 2022:395

Printed by NTNU Grafisk senter

Preface

This thesis is submitted in partial fulfilment of the requirements for the degree of philosophy doctor (PhD) at the Norwegian University of Science and Technology (NTNU) in Trondheim.

The PhD work has been carried out at the Department of Electric Power Engineering, between June 2017 and August 2020, with Prof. Arne Nysveen as main supervisors, Prof. Robert Nilssen and Dr. Niklas Magnusson as co-supervisor.

This work was performed as a part of the project "Thermal Modelling of Transformers" (project number: 255178) funded by the Research Council of Norway, Statnett, Hafslund and Lyse Nett.

Trondheim, November 2022

Wei Wang

Acknowledgements

This PhD work would not have been possible without the support and inspiration of a number of wonderful individuals — my sincere appreciation goes to all of them for being part of this journey.

First and foremost, I would like to express my deepest gratitude to my supervisor, Professor Arne Nysveen, for his guidance, support and tolerance throughout the PhD project. His encouragement on the experiment has consolidated the essence of the research, and beyond, made me comprehend the conscience of a scientific work. I consider myself very fortunate to have such an insightful and supportive supervisor as my mentor. Thank you, Arne!

I would also like to thank my co-supervisor and spiritual mentor, Professor Robert Nilssen. His crucial comments and advice in the early stage of the PhD project, led me to my research with aesthetic interest: – "Cutting coefficients is always a pleasure!"

A special thanks to my co-supervisor, Dr. Niklas Magnusson. He has been incredibly generous with his time, patience and advice. His guidance on scientific writing and publication will be a lifelong benefit to me. I could not have asked for a more helpful and knowledgeable supervisor. My gratitude also goes to Dr. Atle Pedersen and all the TEMpT members at SINTEF Energy for giving me the opportunity and freedom to carry out my PhD study in a multidisciplinary field.

I'd like to further extend my sincere gratitude to Anders Gytri, Bodil Wold and all the technical staff at the Department of Electric Power Engineering at NTNU who have been of great support.

I am forever indebted to my parents for their unconditional love, trust and constant support of my pursuits. They selflessly encourage me to explore new directions in life and seek my own destiny. Finally, I want to thank the love of my life, Haiyan, and my sons, Luming and Liam, who endured this journey with me, always offering support and love. I dedicate this milestone to all of them.

Trondheim, November 2022

Wei Wang

Abstract

The PhD research work presented in this thesis deals with electromagnetic field calculation and loss evaluation in power transformers under special operation conditions. The special loading conditions under investigation include over-excitation, heavy loading, inductive loading and dc-bias introduced either by geomagnetically induced current (GIC) or by power converter operations.

In a power transformer, the leakage flux enters the steel laminations of the iron core in different directions. The leakage flux can, depending on the orientation, add eddy current or hysteresis losses to the loss caused by the main flux. To study the principles of the influence of the leakage flux on the losses in transformer cores, an instrument that enables a loss measurement under the main flux superimposed with the transverse flux or normal flux was developed. The system was modelled using finite elements to interpret the physical phenomena. The results revealed that the loading conditions (heavy loading or inductive loading) have a significant impact on the local eddy current loss and on the overall hysteresis loss in the core. The identified additional losses indicate that under inductive loading, conventional no-load tests can underestimate the core losses considerably.

Dc magnetisation due to GIC or HVDC converter operation may cause core saturation and result in a serious decline in the transformer performance as well as the power system stability. To distinguish dc-bias caused by GIC and converters, the concept of common mode and differential mode was introduced. An experimental investigation was conducted on a three-phase three-limb transformer to study the power loss and reactive power consumption. The test revealed a significant difference in stray loss and winding loss between the two modes in three-phase transformers. Finally, a solution to mitigate the undesired effects associated with dc-bias of differential mode was discussed.

Computation of iron losses in transformers requires significant numerical efforts, particularly under magnetic saturation when the magnetic nonlinearity needs to be considered. In this PhD work, a Fourier-based effective permeability is proposed to calculate the magnetic flux density for the core loss in transformers under saturation. This includes pre-processing of the nonlinear material. A permeability frequency spectrum is obtained from Fourier analysis, where the fundamental part is used as the magnetisation definition and the harmonic components are used for loss calculation. The proposed Fourier permeability is more efficient than the time-domain

method and yields significantly higher accuracy in stray loss calculation under heavy saturation than energy-based permeability.

Contents

Preface	i
Acknowledgements	iii
Abstract	v
Contents	vii
List of Figures	xi
List of Tables	xvi
List of Abbreviations (or Symbols)	xvii
1 Introduction	1
1.1 Objectives and scope of the work	2
1.2 Background	3
1.3 Outline of the thesis.....	4
1.4 Scientific contributions	5
2 Transformer operation	11
2.1 Transformer loading.....	11
2.1.1 Loading conditions.....	11
2.1.2 Influence of loading on magnetic field distribution	13
2.2 DC bias in power transformers.....	17
2.2.1 DC bias due to GICs.....	17
2.2.2 DC bias due to HVDC electrode operations	18
2.2.3 DC bias due to converter modulation.....	19
2.2.4 Modes of dc bias	21
3 Power losses in transformers	25
3.1 Core losses.....	25
3.1.1 Core loss constitution.....	25
3.1.2 Core loss calculation	26
3.2 Stray losses.....	28

3.2.1	Stray loss distribution in power transformers	28
3.2.2	Stray loss calculation.....	30
3.3	Problem of excessive losses in power transformers.....	32
3.4	Research questions	34
4	Experimental systems and numerical models	37
4.1	Effective permeability for loss evaluation	38
4.2	Experimental work	41
4.2.1	Material characterisation.....	41
4.2.2	Power losses measurement with multidirectional flux.....	46
4.2.3	Measurement of three-phase transformer under dc-bias	49
4.3	Electromagnetic simulations	51
4.3.1	Models of multidirectional flux in lamination	52
4.3.2	Models of dc-bias in three-phase transformer.....	53
5	Results.....	57
5.1	Power losses due to multi-directional flux in laminated steels [Paper III, IV,V]	57
5.2	Common mode and differential mode of dc-bias [Paper VI, VII]	61
6	Discussions.....	65
6.1	Finite element loss calculation using effective permeability — in answer to research question 1	65
6.2	Effect of leakage flux on core losses in power transformer — in answer to research question 2.....	66
6.3	Influence of dc-bias on power transformer — in answer to research question 3.....	67
6.4	Limitations and source of the errors.....	68
7	Conclusions.....	75
7.1	Concluding remarks	75
7.2	Recommendations for Future Work.....	76
	Bibliography	79

Publications.....	85
Paper I.....	85
Paper II.....	93
Paper III.....	99
Paper IV.....	111
Paper V.....	121
Paper VI.....	127
Paper VII.....	141

List of Figures

Figure 1.1 Power transformer used for HVDC transmission link [2]. 1

Figure 1.2 The iron parts in a power transformer (the iron tank and cover are not shown). 2

Figure 2.1 The equivalent circuit diagram of the transformer on load condition. (from paper IV) 12

Figure 2.2 An example of a phasor diagram representing a transformer in loading operation. Left: resistive loading; Right: inductive loading. (from paper IV) 12

Figure 2.3 Leakage flux orientations at the top of the winding of a single-phase transformer. Left: TD; Right: ND. (from paper IV)..... 13

Figure 2.4 Definition of the flux directions in the grain-oriented steel laminations. RD: rolling direction; ND: normal direction; TD: transverse direction. (from paper IV) 14

Figure 2.5 Illustration of the local zone (a) and the global zone (b) of the leakage flux distribution in the core of a single-phase power transformer. (a) Leakage flux density component in x-axis and flux lines (perpendicular to the limb). (b) Penetrated flux along the edge of the core window. (from paper IV) 14

Figure 2.6 Flux line distribution inside the magnetic core of a single-phase power transformer at the time when the leakage flux is maximum. Three representative points for flux density calculation: A, the centre of the Core; B, the middle point between the Windings; C, the edge of the Yoke. 15

Figure 2.7 Flux density variations over a period under the resistive loading (left) and the inductive loading (right) at three locations. The two upper figures are with low leakage flux density $B_{leak}=0.31$ and the two lower figures is with high leakage flux density $B_{leak}=0.62$ 16

Figure 2.8 Geomagnetically induced current distribution in three-phase power system and power transformers. (from paper VI) 17

Figure 2.9	Measured GIC profile at neutral of a generator step-up transformer [13].	18
Figure 2.10	Fundamental frequency voltage and current on the dc side of the VSC-HVDC converter transfer to the ac side and appear as dc current circulating in the windings of the power transformer. (from paper VI).....	19
Figure 2.11	The phase currents (IA, IB and IC) and their dc components (IA_dc, IB_dc and IC_dc) on the converter ac bus due to harmonic transfer from the dc side. (from paper VI)	20
Figure 2.12	A phasor representation of the dc component in each phase of the transformer winding due to the modulation effect.	23
Figure 3.1	Alternating magnetisation (1D magnetisation) and rotating magnetisation (2D magnetisation). Alternating magnetisation has variable magnitude and single direction; rotating magnetisation can have variable magnitude and direction.	28
Figure 3.2	Penetration of field and induced current inside a conductor. (from paper V).....	31
Figure 4.1	Flux density distribution in the transformer core (a quarter model) from a time-domain simulation. (a) Isotropic magnetic core. (b) Anisotropic (grain-oriented) magnetic core. (from paper I)	39
Figure 4.2	Average flux density spectra calculated for the magnetic core with different materials. (a) Isotropic (NGO) magnetic core. (b) Anisotropic (GO) magnetic core. (from paper I)	40
Figure 4.3	Stray loss on the transformer tank wall calculated by various effective permeability methods under different saturation levels. (from paper II)	41
Figure 4.4	Standardised magnetic property measurement devices for electric steels (Brockhaus). Left: Epstein frame tester (according to IEC 60404-2); Right: Single sheet tester (SST, according to IEC 60404-3).....	42
Figure 4.5	Standardised magnetic property measurement for a ring core according to IEC 60404-6.	43

Figure 4.6	Schematic diagram of the loss measurement system under dc-bias. (a) The excitation voltage applied on the primary coil has a small dc-bias. (b) The dc-bias is introduced by a separate coil (on the right) connected to a dc power supply and an inductor for current smoothing. (from paper III).....	44
Figure 4.7	Schematic diagram for material magnetisation characterisation using a three-phase three-limb transformer. The red arrow represents the flux path. (from paper VII)	45
Figure 4.8	The examples of material characterisation (a) The measured power losses in the GO electrical steel versus flux density. (b) The components of the permeability tensor versus flux density measured using the single sheet tester (SST). (μ_x : rolling direction, RD; μ_y : transverse direction, TD). (c) Measured magnetisation characteristic for the transformer core. (d) B-H curve under ac nominal MMF superimposed with multiple dc-bias levels. (from paper III).....	46
Figure 4.9	Schematic diagram of the loss measurement system with artificial leakage flux superimposed with the main flux. The AC power supply 1 is connected to two coils wound around the square frame and the coil current generates the main flux in the frame. The AC power supply 2 is connected to a coil wound around the C-shaped core and the coil current generates the leakage flux to the lamination. The C-shaped core is mounted either on the side of the lamination (a) for TD flux or on the top of the lamination (b) for ND flux. (from paper III).....	48
Figure 4.10	A 2.5 kVA three-phase three-limb transformer for dc-bias test and the EGSTON grid emulator (controllable three-phase voltage source) in the National Smart Grid Laboratory (NSGL), Norway. (from paper VII).....	49
Figure 4.11	Transformer winding connection and dc-bias implementation. (from paper VI)	50
Figure 4.12	A phasor representation of dc current distribution in each phase of scenario 0° , 60° , 90° , 150° . $\theta_0 - \theta_1$ determines the magnitudes of dc current in each phase. (from paper VI)	51

Figure 4.13	The geometry view of the 2D and 3D model. Left: 2D model to study the TD flux and flux superimposition (with RD flux). Right: 3D model to study ND flux and flux superimposition (with RD flux). (from paper IV)	52
Figure 4.14	View of the geometry model in FE modelling. Upper: 2D FE (half) model for core loss calculation. Lower: 3D FE (quarter) model for stray loss calculation. (from paper VII)	53
Figure 5.1	Incremental power loss versus phase angle with the main flux superimposed with the transverse flux. The main flux densities are 1.6 T and 1.8 T; the transverse flux density varies from 0.2 T to 0.6 T. (from paper IV)	58
Figure 5.2	Incremental power loss versus phase angle with the main flux superimposed with the normal flux. RD flux density BRD=1.6 T; ND flux density and TD flux density are BND= 0.2 or 0.4 T. (from paper IV)	58
Figure 5.3	Flux distribution in the steel lamination with incident TD alone (Left: BTD=0.2 T; BRD=0 T), RD alone (Middle: BTD=0 T; BRD=1.6 T) and with incident TD flux superimposed with RD flux (Right: BTD=0.2 T; BRD=1.6 T). (from paper IV)	59
Figure 5.4	The eddy current distribution in the lamination under the ND flux (0.2 T) superimposed with the RD flux (1.6 T) at phase angles of 90° and 0°. (from paper V)	60
Figure 5.5	Power Losses versus dc-bias of CM. (from paper VI)	61
Figure 5.6	Stray loss and winding loss (with both tank and clamping structure) due to DM dc current of four different configurations. (from paper VII)	62
Figure 5.7	The maximum flux density in the magnetic core under 1.6 A DM dc current of four different configurations and 1.6 A CM dc current. (from paper VII)	63
Figure 5.8	The maximum volumetric stray loss density in the tank under 1.2 A DM dc current of four different configurations. (from paper VII)	63

Figure 5.9	The calculated instantaneous stray loss over one period in the tank under 1.2 A DM dc current at the configuration of 0° . (from paper VII)	64
Figure 6.1	The cross-section (observed by Scan Electronic Microscope) of the electric steel used in the square frame. The thickness of the sheet can vary almost by 10% in one single batch.....	69
Figure 6.2	The C-shaped core and the excitation system. (a) The C-shaped core (CSC) was made by a half ring unit. (b) The excitation and voltage pickup coils were wound around the CSC. Plastic spacers were used to create air gaps. (from paper III)	70
Figure 6.3	The transverse flux distribution (flux density in the horizontal direction, B_x) in the lamination. The end (inhomogeneity) effect is cancelled out by subtracting the measurement of the three-unit core from the measurement of the five-unit core (from paper III).	71
Figure 6.4	Comparison of the measured and calculated primary phase currents over one period at 1.6 A dc current for the four different DM cases and for the CM case. (from paper VII).....	74

List of Tables

Table 2.1	Peak values of flux density in the yoke.....	16
Table 4.1	Error comparison for different core materials. (from paper I)	40
Table 4.2	Flux density, voltage and excitation current ranges on the main and the C-shaped core excitation systems. (from paper III)	48
Table 4.3	DC current ratio defined in each phase for loss measurement. (from paper VI)	51
Table 5.1	Winding losses and core losses due to DC bias of DM. (from paper VI).....	61

List of Abbreviations (or Symbols)

NTNU	The Norwegian University of Science and Technology
2D	Two-dimensional
3D	Three-dimensional
AC	Alternating current
B	Flux density
B_m	Maximum flux density
B_{peak}	Peak flux density
DC	Direct current
E	Electric field intensity
FEA	Finite element analysis
FEM	Finite element method
GIC	Geo-magnetically induced current
GMD	Geomagnetic disturbances
CM	Common mode
DM	Differential mode
HVDC	High Voltage Direct Current
ND	Normal direction
TD	Transverse direction
PD	Parallel direction
RD	Rolling direction
SST	Single sheet tester
TPFEM	Time periodic finite element method
HBFEM	Harmonic balance finite element method
CFD	Computational fluid dynamics
GO	Grain oriented
NGO	Non-grain oriented
NVE	The Norwegian Water Resources and Energy Directorate
MMF	Magnetomotive force
MMC	Modular multilevel converter
VSC	Voltage source converter
CME	Coronal mass ejections
CSC	C-shaped core

NRC	Notched ring core
P_h	Hysteresis loss
P_e	Eddy current loss
f	Frequency of the magnetisation
t	Thickness of individual sheets of lamination
RMS	Root Mean Square
u_p	Positive pole voltage of voltage source converter
u_n	Negative pole voltage of voltage source converter
V_m	Voltage magnitude of voltage source converter
u_{ac}	AC bus voltage of voltage source converter
S_p	Switching function of positive pole of voltage source converter
S_n	Switching function of negative pole of voltage source converter
m	Modulation index
θ_l	Phase angle of the switching function
P_a	Power loss per unit mass for an alternating magnetisation
P_r	Power loss per unit mass for rotational magnetisation
ρ	Mass density of the material
$B_{x(y)}$	Flux density in the x(y) direction
$H_{x(y)}$	Magnetic field strength in the x(y) direction
H_m	Amplitude e of the time-harmonic magnetic field
T	Period of the oscillation
σ	Electrical conductivity
N_1	Number of turns of the primary winding of transformer
N_2	Number of turns of the secondary winding of transformer
A	Cross-sectional area of magnetic core
P_s	Specific power loss in electric steel
P_m	Power loss reading from wattmeter
P_{incr}	Incremental power loss
P_{net}	Net power loss (excluding measurement instrument loss)
P_{am}	Power loss in the auxiliary excitation system
μ	Magnetic (relative) permeability
J_e	Current density
Φ	Electric scalar potential
A_i	Vector magnetic potential at time step i

$J_{e,i}$	Excitation current at time step i
I_m	Amplitude of the input current
DoN	Degree of nonlinearity of the function $B(I)$
H_{max}	Maximum magnetic field
I_{max}	Maximum input current
I_0	Primary no-load current
Φ_m	Main flux in the transformer core
I_2	Secondary current of transformer
I_1	Total primary current of transformer
I'_1	Primary load current of transformer
B_{yoke}	Flux density in the specified point in the yoke
B_{leak}	Flux density in the specified point at the leakage channel
B_{core}	Flux density the specified point in the core
ω	Angular frequency
ω_0	Fundamental angular frequency
$\mu_{AE,eff}$	Effective Magnetic (relative) permeability based on average energy
$\mu_{SE,eff}$	Effective Magnetic (relative) permeability based on simple energy
$\mu_{RMS,eff}$	Effective Magnetic (relative) permeability based on RMS method
$\mu_{eff,k}$	Effective Magnetic (relative) permeability based on Fourier method
$\mu_{mf-eff,k}$	Modified Effective (relative) permeability based on Fourier method
$\mu_{gf-eff,k}$	Generalised Effective (relative) permeability based on Fourier method
Z_i	Intrinsic surface impedance
ϵ_B	Spectrum based error
$B_{FD,i}$	The average flux density at the harmonic order i , in frequency domain
$B_{TD,i}$	The average flux density at the harmonic order i , in time domain

1 Introduction

Temperature is the driving force for the aging of the insulation system in transformers, particularly in large power transformers (Figure 1.1). Accurate lifetime predictions for transformers rely on knowledge of their internal temperatures. High internal temperatures in a transformer may have immediate, disastrous effects on a transformer in addition to the longer-term aging effects referred to above [1]. Generally, transformers are designed for higher loads than what are required to deliver on average. Traditionally, the margins used in the design of older units were typically larger than those used today due to design calculations being less accurate in the past. Consequently, if the power losses and temperature distribution can be calculated satisfactorily, reinvestment may be delayed for transformers with a favourable history.



Figure 1.1 Power transformer used for HVDC transmission link [2].

Temperature is a function of load, transformer design and ambient conditions. Precisely calculating the temperature distribution has always been a challenging task. Electromagnetic models and thermal models are particularly needed to estimate temperature and predict lifetime to reach Norwegian and European goals of efficient and reliable grid operation and monitoring. Under normal operation, a well-designed transformer is considered to have good thermal

management, which means the overall temperature rise fulfils the standardised specification and the local hot-spot hazards are largely minimised [3]. Today, variable power production and load, due to e.g. wind and solar energy and charging of electrical vehicles, lead to new load patterns for power equipment. Under these special loading conditions, both the overall power loss enhancement and the local heat hazard should be re-evaluated. The special conditions to be investigated in this research project include over-excitation, heavy loading and/or inductive loading and dc magnetisation. Unlike various transient events that directly threaten the insulation of transformers, the abovementioned phenomena persist for a longer time (longer than the thermal time constants) or even constantly; therefore, this creates an enhanced temperature profile globally or locally in a power transformer.

1.1 Objectives and scope of the work

This PhD research work is a part of the project ‘Thermal modelling of transformers’ funded by the Research Council of Norway, Statnett, Hafslund and Lyse Nett. The main project is to develop thermal models that can be adapted to existing transformers to support reinvestment and maintenance decisions and allow safe upgrading and emergency overloading. The objective of this PhD project is to investigate magnetic leakage fields and the resulting power losses in power transformers under special operation conditions. The work mainly focuses on the iron parts (i.e. the magnetic core and iron structure, see Figure 1.2) of power transformers, in which the anisotropy and the nonlinearity of ferromagnetic materials add complexity to the phenomena under investigation.

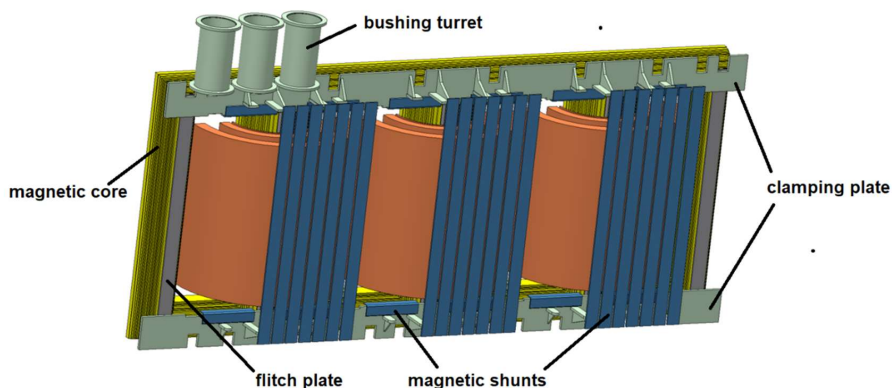


Figure 1.2 The iron parts in a power transformer (the iron tank and cover are not shown).

This research work covers several special operation conditions, including over-excitation, heavy and inductive loading and dc magnetisation. Under these circumstances, the overall power losses may rise in the magnetic core, reducing the lifetime of the transformer. More importantly, some operations may introduce local hot spots in the iron parts and deteriorate adjacent insulation in a short time. As such, this research work aims to investigate how different factors affect power losses locally and globally and to evaluate the risks of overheating. Thermal modelling of transformers, i.e. the temperature calculation is beyond the scope of the research in this PhD project. Dedicated CFD modelling of the thermal-hydraulic system is handled by another work package in the main project.

In the experimental investigations, the material characterisation was performed on the grain-oriented (GO) electrical steels. The developed instrument in this research project enables loss measurement under multi-directional flux as well as under dc-bias. Deriving specific power loss is beyond the scope of the work. The dc-bias tests were carried out in a three-phase three-limb transformer. Although the methodology and the numerical method developed can apply to different types of transformers, investigation of transformers other than the three-phase three-limb transformer is beyond the scope of this work.

The finite element method (FEM) is used to determine the magnetic field and the iron losses in power transformers. Nonlinear and anisotropic effect of the ferromagnetic materials are considered in FE simulation. Development of hysteresis models for calculating core loss is beyond the scope of this research. Calculation of stray loss in windings or bushing mounting plates are beyond the scope of the research project, as the analytical methods have been well-established.

1.2 Background

Temperature rise caused by power losses is the main driver for transformer aging, and in some extreme case, an immediate deterioration [1]. Today, engineers face challenges in transformer design requirements such as high loss capitalisation and optimum performance. Additionally, there could be constraints on the weight, dimensions and clearance of the transformer. A well-designed transformer under normal condition maintains good thermal control, which enables a lifetime over 40 years [4]. Reduced lifetime is often linked to the degeneration of the insulation

system, for instance, caused by excessive power losses under occasional unconventional operation conditions [3].

- **Over-excitation**

When a transformer is subjected to an over-excitation voltage, the magnetising current increases dramatically and raises the winding loss. More importantly, the flux spills out of the core into the neighbouring structural parts and enhances the stray losses.

- **Inductive-loading**

Transformers sometimes operates in a loading condition other than resistive loading. In such cases, the phase angle between the core main flux (generated by the excitation voltage) and the leakage flux (related to load current) varies. As a result, the superimposed flux density and the associated power loss become phase dependent. Therefore, the conclusion that core loss is load independent shall be re-evaluated if the abovementioned effect is significant.

- **DC-bias**

Geomagnetically induced currents (GICs) [5] [6] [7] and HVDC system operations [8] [9] [10] [11] [12] are two main causes of dc magnetisation in gird transformers. Depending on the level of the dc excitation, the loss feature can deviate significantly from ac symmetric excitation; hence, the core loss depends on both applied ac and dc flux.

More importantly, dc magnetisation leads to half-cycle saturation of the transformer core [13]. Similar to the phenomenon of ac voltage over-excitation, the excessive magnetisation current due to (half-cycle) saturation can result in hot spots in the windings and structural parts [14]. The current harmonic increases reactive power absorption and causes voltage instability [15]. In the worst scenario, grid transformers are destroyed [10] and system blackouts [16] may occur.

1.3 Outline of the thesis

This PhD thesis is organised in three parts.

The first part (Chapter 1, 2, 3) gives an introduction of the project background, literature review of the research frontier and then derives the research questions.

- *Chapter 1* presents an introduction to the project background, motivation and the outline of the thesis.

- *Chapter 2* gives an introduction to power transformer operation. The thermal issue in a power transformer under special operation conditions is highlighted in this chapter.
- *Chapter 3* describes the classification and constitution of power losses inside a power transformer. Classic numerical approaches to calculate electromagnetic field and power losses are reviewed. The research questions are derived in this chapter.

The second part (Chapter 4, 5, 6, 7) presents the development of numerical models, simulations and experiments. Finally, it summarises the research findings and answers the research questions.

- *Chapter 4* describes the methodology of the experimental work and the numerical simulations developed in this research work.
- *Chapter 5* summarises the study results and research findings.
- *Chapter 6* presents discussion of the results and the limitation, source of error in the research work.
- *Chapter 7* includes the conclusions and the suggestions for future works.

The third part (Reference and appendix) presents the reference and the paper collections.

- The experimental results, numerical analysis and the discussions are presented as a paper collection in the appendix. Seven papers are presented, two published in *IET Transactions on Electrical Power Applications*; one published in *IEEE Transactions on Magnetics*; one published in *Review of Scientific Instrument*; one published in *Journal of Magnetism and Magnetic Materials*; one published in *Proceeding of the Conference on the Computation of Electromagnetic Fields (COMPUMAG)*; and one published in *Journal of Electrical Engineering*.

1.4 Scientific contributions

The main contributions of the publications in this thesis are listed as follows. The general research question was proposed by my supervisors. I conducted the literature search and formulated the concrete research question, fitting in the current scientific literature. I designed the studies, performed the simulations, carried out the experiments, conducted the data analysis, wrote the draft of the manuscript and implemented the contribution of the co-authors.

[Paper I]: Wei Wang, Arne Nysveen, Niklas Magnusson, Robert Nilssen, “Fourier-based effective permeability for transformer iron losses computation under saturation,” IET Transaction on Electrical Power Applications, December 2020, Volume 14, Issue 13, p. 2609–2615, <https://doi.org/10.1049/iet-epa.2020.0315>.

This paper proposes a Fourier method to calculate the magnetic flux density used for the iron loss evaluation in transformers under saturation. It includes pre-processing of the nonlinear material. A permeability frequency spectrum is obtained from Fourier analysis, where the fundamental part is used as magnetization definition and the harmonic components are used for core loss calculation. Several Fourier-based formulations of permeability have been proposed to deal with a magnetic core under saturation. It is found out that in a magnetic core with homogenous distributed flux such as one made of GO steel, the original formulation (without domain decomposition) gives sufficiently accurate result. In case of inhomogeneous distributed flux under heavy saturation, the modified formulation with domain decomposition significantly improves the accuracy. Degree of nonlinearity (DoN) is introduced to assist domain decomposition. Under a moderate saturation, a single domain decomposition seems sufficient, whereas under heavy saturation (highly nonlinear), two and more domain divisions is needed. The proposed methods offers a time efficient tool to calculate core loss under various saturation levels and nonsinusoidal excitation currents.

[Paper II]: W. Wang, A. Nysveen, N. Magnusson and R. Nilssen, "Computation of transformer iron losses under saturation using the Fourier method Part 2: Stray loss," *22nd International Conference on the Computation of Electromagnetic Fields (COMPUMAG)*, Paris, France, 2019, pp. 1-4, doi:10.1109/COMPUMAG45669.2019.9032726.

In this paper, the influence of the permeability definition (proposed in paper I) of the core material on leakage field and the associated stray loss calculation is studied. It is found out that the accuracy of calculated stray loss under heavy saturation is largely influenced by the chosen definition of the effective permeability of the magnetic core and the described Fourier method yields significantly higher accuracy than energy based methods. In order to evaluate the stray losses due to nonsinusoidal excitation, a waveform correction factor is proposed based on the relationship between magnetic field and input current. The results obtained by this method are compared to those given by a time domain calculation to evaluate the accuracy of the method. The proposed waveform correction factor in combination with the conventional surface impedance method enables time efficient evaluation of the stray loss for nonsinusoidal current excitation under saturation.

[Paper III]: W. Wang, A. Nysveen and N. Magnusson, “Apparatus for loss measurements under multidirectional and dc-bias flux in electrical steel laminations,” *Rev. Sci. Instrument.* Vol.91, Issue 8, 2020, DOI: 10.1063/5.0011076.

This article describes the design and construction of an apparatus for loss measurements under two scenarios. 1) The main flux in the rolling direction is superimposed with flux in either the transverse or normal direction, while varying magnitude and phase angle between two fluxes. 2) The main flux having a dc-bias. The main flux in the rolling direction is generated in a square lamination frame by the current in excitation coils. The transverse and normal direction fluxes are generated by the current in auxiliary excitation coils wound around powder cores. The dc-bias flux is created either by an ac current with a small dc offset in the excitation coils or by a separate coil excited by dc current. We implement and compare the two dc-bias methods and discuss the commons and differences. Experimental measurements demonstrate the apparatus' ability to provide loss measurements in a large range of flux densities and orientations important for studying iron core losses in e.g. transformers under saturation.

[Paper IV]: W. Wang, A. Nysveen and N. Magnusson, "The influence of multidirectional leakage flux on transformer core losses," *Journal of Magnetism and Magnetic Materials*, 2021. <https://doi.org/10.1016/j.jmmm.2021.168370>.

In this article, an experimental investigation has been performed to characterize the power loss feature in the core lamination due to leakage fluxes. To study the principles of the influence of the leakage flux on the losses in transformer cores, the problem was isolated to an experiment on a stack of laminations in an Epstein-like frame. The frame carried the main flux, while additional flux entered the laminations in the two directions perpendicular to the main flux. Additionally, the system was modelled using finite elements to interpret the physical phenomena. The measurement result reveals that the loading angle has a significant impact on the eddy current loss in the local zone as well as the overall hysteresis loss in the global zone. Therefore, the conventional no-load test may underestimate core loss considerably under inductive loading. In contrast, the rotational power loss that appears locally has a negligible contribution, regardless of the phase and the magnitude of the superimposed leakage flux density.

[Paper V]: W. Wang, A. Nysveen and N. Magnusson, "Eddy Current Loss in Grain-Oriented Steel Laminations due to Normal Leakage Flux," *IEEE Transactions on Magnetics*, vol. 57, no. 6, pp. 1-4, June 2021, no. 6301604, doi: 10.1109/TMAG.2021.3069727.

In this article, the loss influence on the steel lamination by the normal flux is investigated experimentally and numerically. Due to the strong magnetic anisotropy of the lamination structure, the penetrating flux tends to saturate the lamination in its plane, even when the incident stray flux density is low. Therefore, the nonlinearity of the lamination has a considerable impact on the eddy currents and the associated power losses. A homogenization approach for modelling grain-oriented steel lamination based on the finite element method is implemented for computing eddy current loss, taking both magnetic anisotropy and the saturation effect into account. The results show that eddy current loss dominates when the lamination is exposed to normal flux and the loss increases rather rapidly with increasing normal flux density due to the nonlinear effect. When the normal flux is superimposed with the main flux, the power loss can dramatically increase at a low phase angle. Moreover, it is found out that both the

normal flux density and the main flux density play important role in the loss enhancement, at a decreased loading angle, attention must be paid on the local heat enhancement in the core lamination exposed to the normal leakage flux.

[Paper VI]: W. Wang, A. Nysveen and N. Magnusson, “Common and differential mode of dc-bias in three-phase power transformer,” *Journal of Electrical Engineering*, 2022. <https://doi.org/10.1007/s00202-022-01592-7>

In this article, we introduce the concept of common mode and differential mode to distinguish dc-bias caused by GIC and converters. Experimental investigations were made on a three-phase three-limb transformer, where the loss impact as well as reactive power consumption are studied. The test shows a significant difference in stray loss between the two modes in three-phase power transformers: The power losses in the three-phase three-limb transformer are susceptible to DM dc current, but not sensitive to CM dc currents. The magnetizing currents of DM are significantly larger than CM, resulting in higher stray losses as well as winding loss. On the other hand, the influence on the core loss is insignificant. The DM dc currents enhances the reactive power consumption and introduces an unbalanced voltage distribution in three phases. Last, the test shows that the delta winding can significantly reduce the stray loss caused by the DM dc currents. This implies that a delta winding can be a mitigation measure to reduce excessive loss (as well as noise) induced by the DM dc current, as long as the care is taken of the rating of the delta winding.

[Paper VII]: W. Wang, A. Nysveen and N. Magnusson, “Power losses in three-phase three-limb transformer due to common and differential mode of dc-bias,” *IET Transaction on Electrical Power Applications*, 2021. [//doi.org/10.1049/elp2.12113](https://doi.org/10.1049/elp2.12113)

In this article, the power loss feature of common mode (CM) and differential mode (DM) of dc-bias in a three-phase three-limb transformer are investigated experimentally and numerically. Time periodic FEM is adopted to calculate core loss and magnetization current. 3D transient FE simulation is performed to calculate stray losses. The results revealed that the performance of power losses are significantly influenced by dc current directions, arrangement of the structural parts and the method of winding connection. It is found out that:

- The flux density offset (thereby the maximum flux density) due to the DM dc-bias is significantly larger than that of CM, due to the low reluctance path of the DM.
- The core loss is not sensitive to dc-bias, regardless of the magnitudes and modes of the applied dc currents.
- The winding losses due to DM dc-bias are significantly larger than that of CM, due to high magnitudes of the magnetizing currents as well as their high frequency harmonic contents.
- The excessive stray loss caused by the DM dc currents can be reduced significantly by introducing a delta winding.

The results above shows that a three-phase three-limb transformer, which is vulnerable to CM dc currents, is susceptible to DM dc current. The DM dc-bias poses risk of a local overheating hazard in the tank and the clamping plates in a power converter connected transformer, particularly if a delta winding is not used. With proposed FEA, the loss density distribution can be identified and mitigation measure such as delta winding, dimension optimization and magnetic shunt placement can be employed based on the numerical calculation.

2 Transformer operation

A transformer experiences power losses during its operation. Energy dissipation occurs in a magnetic core due to alternating magnetisation at system frequency, which is known as the core loss or iron loss. It has been estimated that the iron losses constitute around 5% of all electricity [4]; therefore, the financial costs are vast. On the other hand, the flow of a current in conductors in a transformer generates ohm loss, determined by the magnitude of the current and the resistance of the system. These ohm losses are known as the load loss or copper loss of the transformer. Typically, the load loss can be categorised into three groups: 1. ohmic resistive loss in the winding; 2. eddy current loss in the winding; and 3. eddy current loss in the tanks and structural parts.

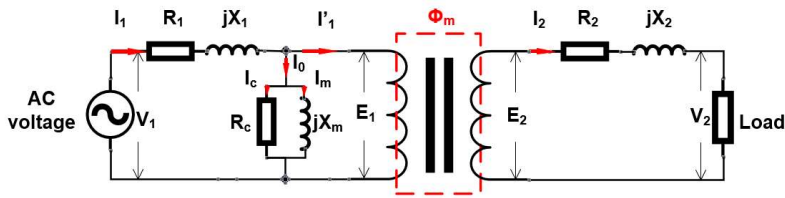
In the normal no-load operation, i.e. at the rated flux density, the magnetising current is so small that the ohm loss in the primary winding is negligible. Meanwhile, the stray losses in the tank and structural parts are insignificant as most of the flux is confined in the magnetic core. In the load operation, the load loss is present in the winding, tanks and structural metalwork. At nominal loading, the stray losses constitute only a small proportion of the total load losses. The load current in the secondary of the transformer and its MMF is balanced by an equivalent primary current and its MMF, which implies that, ideally, the iron loss is independent of the load.

The abovementioned common understanding are conclusions drawn from normal operation of a transformer. However, when a transformer is operated under occasional special conditions, these conclusions must be carefully re-visited.

2.1 Transformer loading

2.1.1 Loading conditions

A transformer can operate under various loaded conditions. The magnitude of the secondary current I_2 depends on the secondary terminal voltage V_2 and the load impedance. The phase angle between I_2 and V_2 depends on the nature of the load, which can be resistive, inductive or capacitive. The well-known equivalent circuit diagram of a transformer is shown in Figure 2.1.



- | | |
|---|--------------------------------------|
| V_1 : Primary terminal voltage | V_2 : Secondary terminal voltage |
| E_1 : Primary induced EMF | E_2 : Secondary induced EMF |
| I_1 : Primary current | I_2 : Secondary load current |
| I'_1 : Load component of I_1 | R_2 : Secondary winding resistance |
| I_0 : Primary no-load current | jX_2 : Secondary leakage reactance |
| I_m : Primary magnetising current | Φ_m : Peak magnetic flux |
| I_c : Primary core loss current | |
| R_1 : Primary winding resistance | |
| R_c : Resistance representing core loss | |
| jX_1 : Primary leakage reactance | |
| jX_m : Primary magnetising reactance | |

Figure 2.1 The equivalent circuit diagram of a transformer on load condition. (from paper IV)

The primary no-load current I_0 induces the magnetomotive force (MMF), which set up the main flux Φ_m in the transformer core. Likewise, the secondary current I_2 induces the demagnetising MMF on the secondary winding of the transformer. An equilibrium is established when the primary current creates ampere-turns balance with the secondary. The total current in the primary circuit I_1 is the phasor sum of the primary load current I'_1 and the no-load current I_0 . The resistance and leakage reactance drops are allocated to their respective windings. The phasor diagrams of the actual transformer under resistive loading and inductive loading conditions are shown in Figure 2.2:

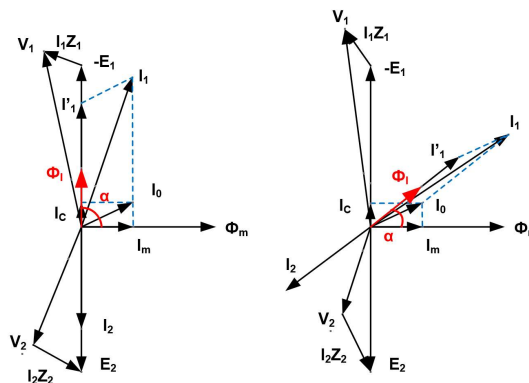


Figure 2.2 An example of a phasor diagram representing a transformer in loading operation. Left: resistive loading; Right: inductive loading. (from paper IV)

In reality, not all of the flux produced by the primary winding links to the secondary, so the transformer is said to possess leakage fields. The leakage flux is represented as Φ_l , which is in phase opposing the load current. As shown in Figure 2.2, under resistive loading, the phase difference between the core flux and the leakage flux α is 90° , whereas under inductive load, α can decrease significantly depending on the phase of the load current.

2.1.2 Influence of loading on magnetic field distribution

The orientation of the leakage flux inside a single-phase transformer is schematically demonstrated in Figure 2.3. The directions where the leakage flux enters the laminated core lead to the following definitions (see Figure 2.4):

- **Transverse direction (TD):** Around the core window, the flux enters the core in parallel with the plane of the lamination and perpendicular to the rolling direction.
- **Normal direction (ND):** On the surface of the yoke and the limb, the flux enters the core perpendicular to both the plane of the lamination and the rolling direction.

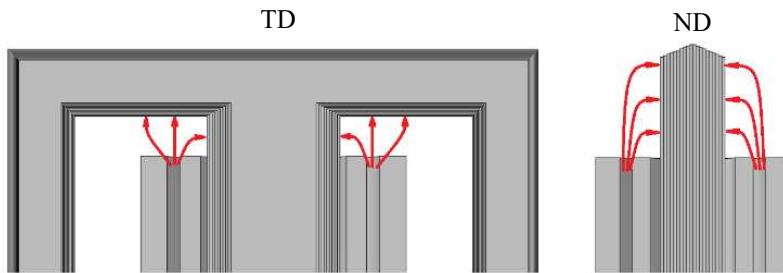


Figure 2.3 Leakage flux orientations at the top of the winding of a single-phase transformer. Left: TD; Right: ND. (from paper IV)

The definition of the flux direction relative to the rolling direction in a grain-oriented (GO) lamination block is further illustrated in Figure 2.4.

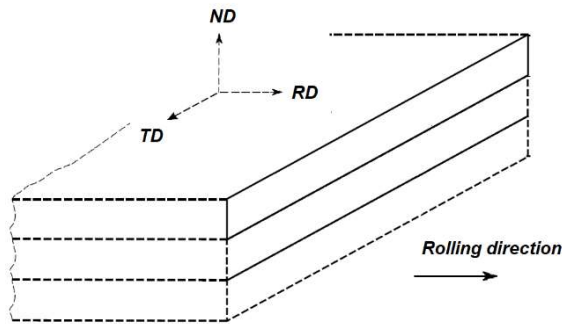


Figure 2.4 Definition of the flux directions in the grain-oriented steel laminations. RD: rolling direction; ND: normal direction; TD: transverse direction. (from paper IV)

The flux entering the core (in either TD or ND) at the top of the transformer eventually turns and becomes parallel to the rolling direction before it again leaves the core at the bottom of the transformer; see Figure 2.5. This flux path inside the core suggests two zones with different loss characteristics:

- **Local zone:** Where the flux enters the core in either ND or TD, the flux is constrained within a small depth in the core. The induced loss is dominated by either eddy current loss (due to ND flux) or rotational power loss (at TD flux) [17] [18].
- **Global zone:** As the entering flux changes direction and becomes parallel to the main flux (in RD), it follows the edge of the core window.

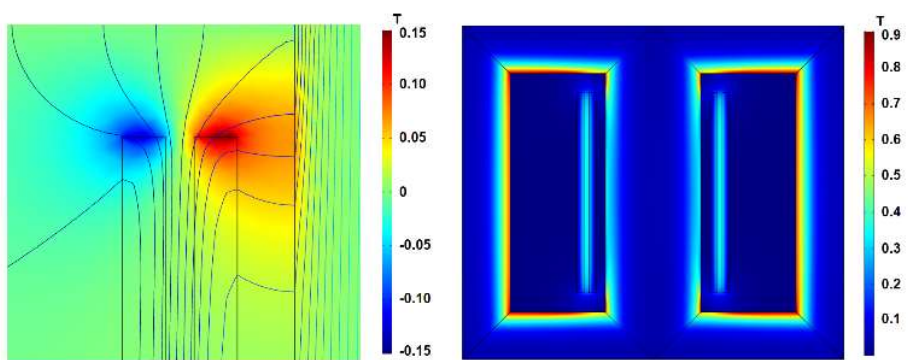


Figure 2.5 Illustration of the local zone (a) and the global zone (b) of the leakage flux distribution in the core of a single-phase power transformer. (a) Leakage flux density component in x-axis and flux lines (perpendicular to the limb). (b) Penetrated flux along the edge of the core window. (from paper IV)

To demonstrate the flux variation in space and time due to the phase angle, the flux density in the yoke B_{yoke} (point C marked in Figure 2.6) under resistive loading and inductive loading was calculated. The flux density at point B is defined as the leakage flux density (B_{leak}), which is set to 0.31 T and 0.62 T. The flux density in the core B_{core} (at point A) is maintained at 1.4 T. The flux variation over a period at the three points is described in Figure 2.7. The peak value of B_{yoke} under different scenarios is listed in Table 2.1.

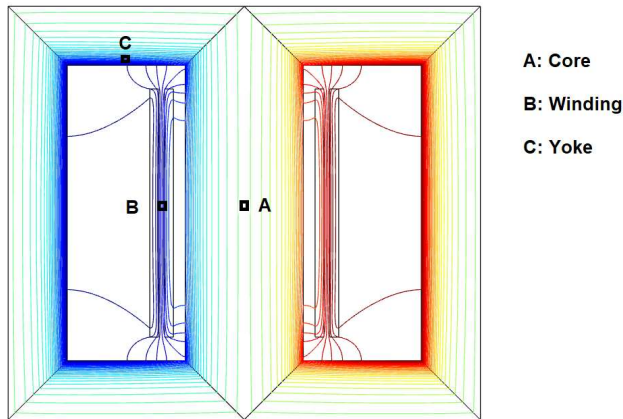


Figure 2.6 Flux line distribution inside the magnetic core of a single-phase power transformer at the time when the leakage flux is maximum. Three representative points for flux density calculation: A, the centre of the Core; B, the middle point between the Windings; C, the edge of the Yoke.

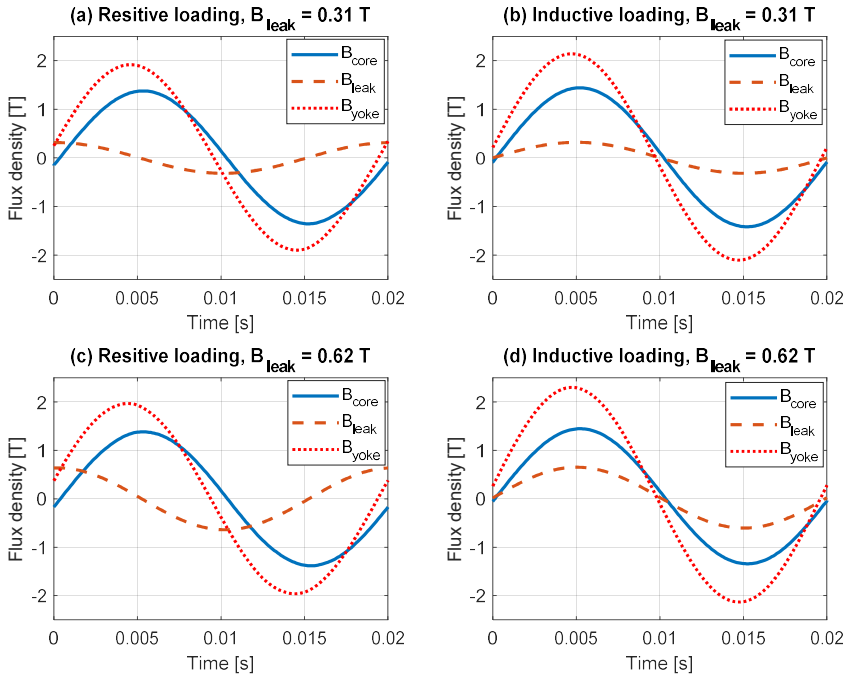


Figure 2.7 Flux density variations over a period under the resistive loading (left) and the inductive loading (right) at three locations. The two upper figures are with low leakage flux density $B_{leak}=0.31$ and the two lower figures is with high leakage flux density $B_{leak}=0.62$.

Loading condition	Resistive loading		Inductive loading	
	a	b	c	d
B_{leak} [T]	0.31	0.62	0.31	0.62
B_{yoke} [T]	1.94	1.98	2.14	2.31

Table 2.1 Peak values of flux density in the yoke.

As shown in Figure 2.7, due to the superimposed leakage flux, B_{yoke} is significantly larger than B_{core} and there is a phase difference between B_{core} and B_{yoke} . B_{yoke} increases with an increasing B_{leak} and a decreasing phase angle. The increment of B_{yoke} under inductive loading is larger than

that under resistive loading (e.g. B_{yoke} increases by 0.17 T from (b) to (d) and increases by only 0.04 T from (a) to (c)).

In summary, the flux density in the global zone (represented by B_{yoke}) depends on the loading condition and the magnitude of the leakage flux density. The overall power loss is expected to increase with lower phase angle and higher leakage flux density.

2.2 DC bias in power transformers

2.2.1 DC bias due to GICs

Coronal mass ejections (CME) originated from the sun interact with the magnetosphere of the earth and induce a longitudinal quasi-dc potential on the transmission lines, which drives the flow of the induced current (GIC) [13]. The scenario of GIC generation in the network is depicted in Figure 2.8, which has also been extensively illustrated in the literature [13] [5] [6]. As shown, the GIC is a quasi-dc current (low frequency, typically 0.01 Hz to 0.5 Hz) [4] that flows in the power system, which closes its path through transmission lines, windings and neutral points of grid transformers and ground. Factors that influence the level of GIC include geomagnetic latitude, ground resistivity, network topology and the design of the power transformer.

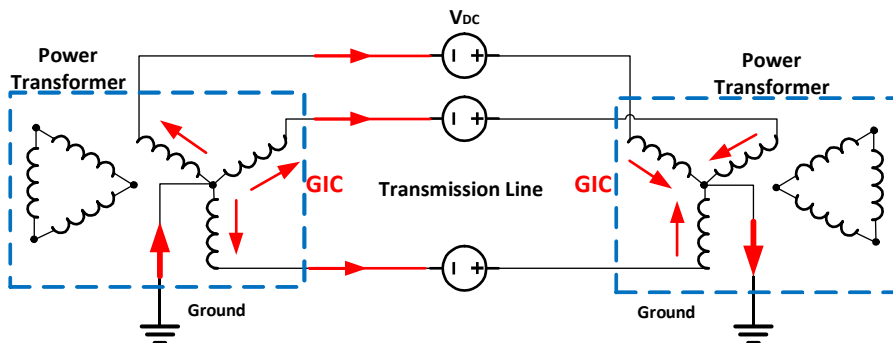


Figure 2.8 Geomagnetically induced current distribution in three-phase power system and power transformers. (from paper VI)

Apparently, the GICs in all three phases go in the same direction. At very low frequency, the high-voltage network is essentially resistive. Considering the symmetric resistance in the three phases, the magnitudes of GICs are considered to be identical in the three phases. Based on these factors, the GICs are often referred to as zero sequence. Because of its origin from solar

activity, GICs are characterized by a large number of narrow consecutive pulses over a period of hours separated by a few high peak pulses of less than a few minutes duration (Figure 2.9 [13]).

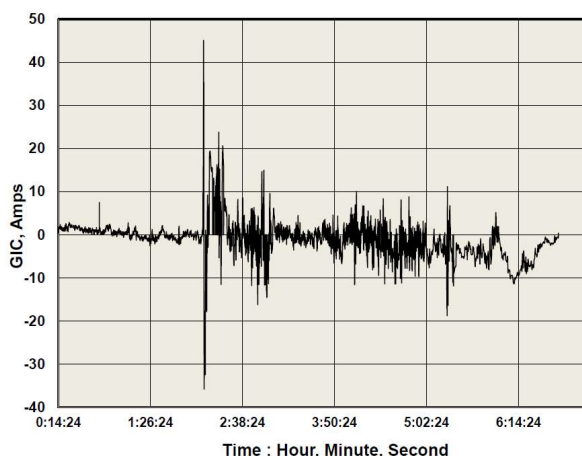


Figure 2.9 Measured GIC profile at neutral of a generator step-up transformer [13].

Factors that determine the susceptibility to GICs of the power transformer include core topology, winding configuration and the design of structural parts [13]. Among them, the core topology has a major impact on the classification. Single-phase and five-leg core transformers with low reluctance to the dc flux are susceptible to GICs. For a three-phase three-limb transformer, the flux of zero sequence has to pass from the top yoke to the tank top, through the tank walls, and return to the bottom yoke from the tank bottom. Therefore, a three-phase three-limb transformer is less susceptible due to the higher reluctance path of the dc flux.

2.2.2 DC bias due to HVDC electrode operations

The stray dc current due to HVDC electrode operations (monopolar or bipolar operation) can flow into solidly earthed transformers between two substations. The phenomenon is considered to be similar to GICs as the stray current flowing in the neutral is of zero sequence. However, different from GICs, the stray currents are driven by the potential difference between substations due to HVDC electrode operation (not from transmission lines). That is, the current emanating from the anode partly enters the earth of one substation and flows into the grounded

neutrals of the transformer towards the other substation (and the cathode) [11]. This dc current can have two major consequences: saturation of the grounded transformers and corrosion of the ground grid of the station nearest the cathode.

Apart from the difference in origination and consequences, the stray currents feature a stationary dc current, whereas GICs are characterized by consecutive pulses over different period of time scale as mentioned in 2.2.1.

2.2.3 DC bias due to converter modulation

A rapid increase of the HVDC transmission line creates a situation where ac and dc lines may share the same corridor or even on the same towers [8] [9]. A dc line in parallel with an ac line is exposed to a fundamental frequency inductive coupling, where a longitudinal voltage potential of fundamental frequency will generate on the dc line. As depicted in Figure 2.10, the inductive coupling part is represented as two longitudinal voltage sources in this model. The fundamental frequency voltage and current on the dc side of the converter transfer to the ac side and appear as dc current (and 2nd order harmonic) circulating in the windings of the power transformer.

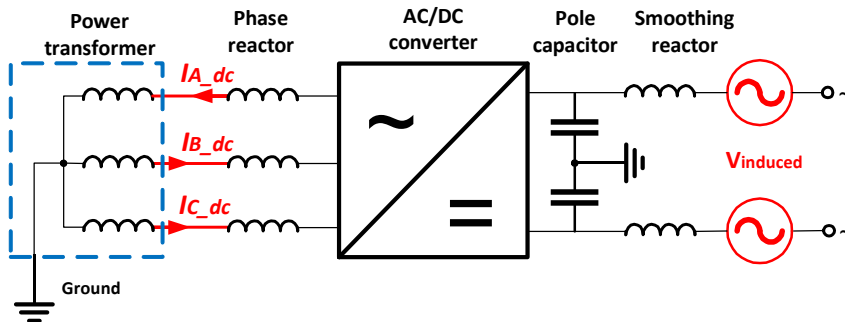


Figure 2.10 Fundamental frequency voltage and current on the dc side of the VSC-HVDC converter transfer to the ac side and appear as dc current circulating in the windings of the power transformer. (from paper VI)

The difference between two induced voltage sources and the impedance seen from the dc side determines the dc current level on the ac bus. Different from previous two dc currents, the sum of the dc currents that appeared on the ac bus is zero. As the dc currents are not identical in three phases, this results in asymmetrical magnetisation of transformer core. The saturation

caused by dc current can result in excessive heating and an increased noise level in the transformer.

Many factors affect the resultant dc current level in transformers. An investigation of the coupling effect has been reported in [9], where the parallel length, separation distance between ac/dc lines, line transposition and ground resistivity are discussed. Prior research focuses on the VSC-HVDC transmission system, such as [19], where the frequency domain model is derived for a parameter sensitivity study. With impedance representation of the network, the factors such as dc capacitors and modulation index are studied analytically.

As an example, the simulations with the model were conducted as described in Figure 2.10. The classic three-level converter and the modular multilevel converter (MMC) [20] with full control function were implemented. The phase currents on the converter bus as well as their dc components (three-level and MMC) obtained from the simulation are demonstrated in Figure 2.11.

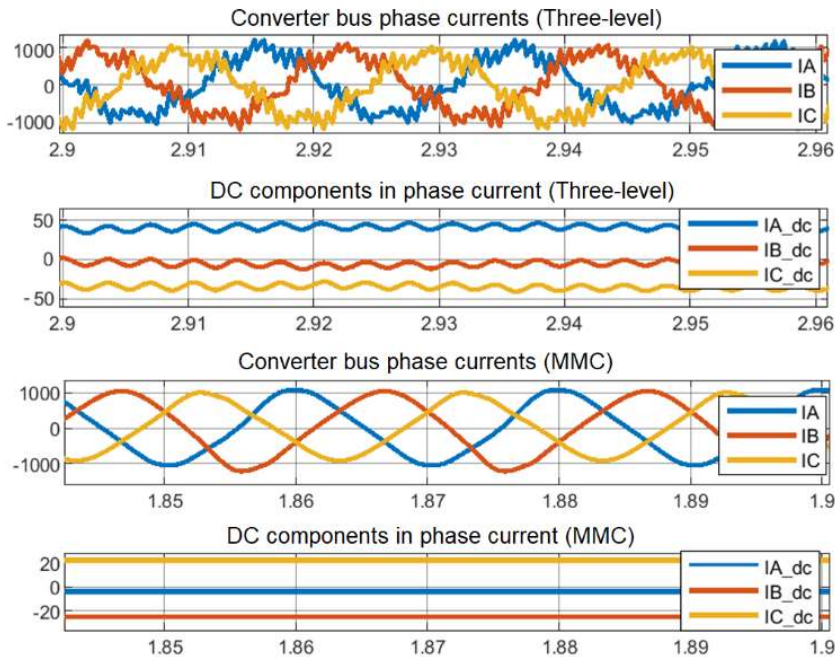


Figure 2.11 The phase currents (IA, IB and IC) and their dc components (IA_dc, IB_dc and IC_dc) on the converter ac bus due to harmonic transfer from the dc side. (from paper VI)

As shown in Figure 2.11, due to the induced fundamental frequency voltage on the dc side, unbalanced phase currents appear on the converter ac bus, which has a dc bias in each phase. The dc (component) current circulates in three phases and the sum of them is zero. This modulation effect occurs in both the three-level converter and MMC, where the dc currents generated in MMC has less ripple than the three-level converter.

2.2.4 Modes of dc bias

The GICs and the stray dc current introduced by HVDC systems are known to be of zero sequence: the dc currents are in the same direction in all three phases. The standard [13] on GICs has classified power transformers into four groups based on their susceptibility to GIC, which is widely used as a guideline to select or design power transformers subject to dc current. However, the features of the dc current generated by converter modulation are considerably different. The sum of the dc currents generated by the converter in three phases is zero. To distinguish the two phenomena, the terminology of common mode (CM) and differential mode (DM) is introduced on the basis of current directions, whereas the term ‘sequence’ is not used to define dc current, since there is no ‘phase’ meaning for a dc signal. In this terminology, the common mode is the same as ‘zero sequence’. Therefore, the GICs and the stray currents are classified as CM. The differential mode in telecommunication often refers to signals that flow in opposite directions in a pair of lines. Here, we extend the DM definition to represent the dc currents of different directions in three phases, where the sum of DM currents is zero. The dc currents introduced by converter modulation is classified as DM.

The distribution of the dc currents within the three phases relies on the phase difference between the induced voltage sources and the switching operation. As the induced voltage and the converter belong to two separated systems, this phase difference is unpredictable in practice. Assume that two fundamental frequency voltage sources u_p and u_n have the same magnitude V_m but out of phase:

$$\begin{cases} u_p = V_m \cos(\omega_0 t + \theta_0) \\ u_n = -V_m \cos(\omega_0 t + \theta_0) \end{cases} \quad (1)$$

where ω_0 is the fundamental frequency and θ_0 is the phase of the voltage source.

The voltage on the ac bus of the converter can be expressed in terms of switching functions [10]:

$$u_{ac} = S_p \times u_p + S_n \times u_n \quad (2)$$

where the switching functions S_p and S_n of the converter are defined as:

$$S_p = \frac{1}{2} \begin{bmatrix} 1 + m \cos(\omega_0 t + \theta_1) \\ 1 + m \cos(\omega_0 t + \theta_1 - \frac{2}{3}\pi) \\ 1 + m \cos(\omega_0 t + \theta_1 + \frac{2}{3}\pi) \end{bmatrix}$$

$$S_n = \frac{1}{2} \begin{bmatrix} 1 - m \cos(\omega_0 t + \theta_1) \\ 1 - m \cos(\omega_0 t + \theta_1 - \frac{2}{3}\pi) \\ 1 - m \cos(\omega_0 t + \theta_1 + \frac{2}{3}\pi) \end{bmatrix} \quad (3)$$

where m is the modulation index and θ_l is the phase of the switching functions.

If we put (1) and (3) into (2), take only the dc component of (2) u_{dc} and simplify, we obtain:

$$u_{dc} = \frac{mV_m}{2} \begin{bmatrix} \cos(\theta_1 - \theta_0) \\ \cos(\theta_1 - \theta_0 - \frac{2}{3}\pi) \\ \cos(\theta_1 - \theta_0 + \frac{2}{3}\pi) \end{bmatrix} \quad (4)$$

Equation (4) indicates that the relative phase difference between the induced voltage and the switching functions of the converter $\theta_0 - \theta_l$ determines the magnitudes of dc components in each phase. A phasor interpretation of (4) is described in Figure 2.12.

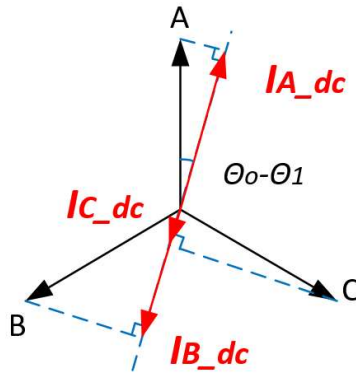


Figure 2.12 A phasor representation of the dc component in each phase of the transformer winding due to the modulation effect.

3 Power losses in transformers

3.1 Core losses

3.1.1 Core loss constitution

Hysteresis and eddy current losses together constitute the core loss. Hysteresis loss (P_h) is caused by the irreversible domain wall movement and magnetisation rotation within the domains in the magnetic material in response to a variable magnetic flux. Hysteresis loss is proportional to the enclosed area of the B - H curve (the hysteresis loop) under quasi-static alternating magnetisation and frequency [21]

$$P_h = k_h f B_{peak}^n \quad (5)$$

where k_h is a material dependent constant, f is the frequency of the magnetisation, B_{peak} is the flux density, and n is the Steinmetz constant having a value between 1.6 and 2.0 for hot rolled laminations and a value of more than 2.0 for cold rolled laminations [21].

There is a complex relationship between the magnetisation, magnetic polarisation, flux density and the applied magnetic field for ferromagnetic materials. The status of the flux density and the magnetic field can be traversed in a trajectory that is related to the past history of the material, which is known as hysteresis. Hysteresis modelling is essentially the determination of the constitutive law, e.g. $B(H)$. Over the years, many hysteresis models have been proposed [22] [23] [24] [25]. These models are based on the physical interpretation of the phenomena or mathematical curve fitting on experimental data.

The Jiles-Atherton model was introduced in [22] to describe scalar hysteresis and it has a modified version [26]. Due to their differential formality, they are relatively easier to implement in FEM tools [27] and circuit simulation software such as EMTP [28]. The Preisach model [23], has been widely used for modelling static scalar hysteresis, especially for prediction of minor loops [25]. The model has also been extended to vector hysteresis modelling [24]. However, practical implementation in FE simulation requires a large amount of experimental data.

Eddy current loss (P_e), which has its origin in induced voltages in the laminations in response to a sinusoidal magnetic flux in the lamination plane, is proportional to the square of the

thickness of the laminations, the square of the frequency and the square of the effective (r.m.s.) value of flux density. Since the thickness of the sheet is much smaller than the skin depth power frequencies, the eddy current loss can be expressed as [21]:

$$P_e = k_e f^2 \delta^2 B_{peak}^2 \quad (6)$$

where k_e is a material dependent constant, δ is the thickness of individual sheets. In practice, the definition of eddy current is complex, and some research [21] classifies (6) as the classical eddy current loss (in accordance with classical electromagnetic theory).

The other type of eddy current loss is known as anomalous loss or excess loss. Anomalous eddy current loss can account for around half of the total iron loss [21] in grain-oriented steels. Anomalous eddy current loss attributes to many causes, such as the displacement, nucleation and annihilation of domain walls, interaction between grains, applied mechanical stress and non-sinusoidal, localised variation of the flux density during the magnetising cycle [29].

Reducing the magnetic domain width is an effective way to minimise anomalous eddy current loss. This has been achieved by modern domain refinement technology and increasing the tensile stress from insulation film. The magnetic domain refinement can be realized by introducing local strain (non-heat resistant domain refinement) or forming grooves (heat resistant domain refinement) in the steel sheet [30].

3.1.2 Core loss calculation

The finite element method (FEM) is widely adopted to determine the magnetic field used to calculate the core losses in power transformers. In the linear region of ferro-magnetic materials, the time-harmonic (frequency domain) approach has proved to be both efficient and accurate in calculating flux density. However, in case of ferromagnetic resonance and GICs when the transformer core enters its nonlinear region, time-consuming time domain simulations are often employed.

For system analysis, optimisation and the inverse problem where the computation effort is demanding, the frequency domain method is desirable. Therefore, effective permeabilities of various types [31] [32] [33] have been proposed to handle the nonlinearity of the ferromagnetic cores. Energy-based methods [31] [32] are derived from the conservation of the exchange of

the magnetic energy (or co-energy). In the average energy method [32], the effective permeability is defined as:

$$\mu_{eff,AE} = \frac{16}{TH_m^2} \int_0^{T/4} \left[\int_{H(0)}^{H(t)} B(H)dH \right] dt \quad (7)$$

where $B(H)$ is the nonlinear magnetisation virgin curve of the material, H_m is the amplitude of the time-harmonic magnetic field and T is the period of the oscillation.

In the simple energy method [31], the effective permeability is defined by means of the magnetic coenergy:

$$\mu_{eff,SE} = \frac{2}{H_m^2} \int_0^{H_m} B(H)dH \quad (8)$$

In the Root Mean Square (RMS) method [34], the effective permeability is defined as:

$$\mu_{eff,RMS} = \frac{\sqrt{2}}{H_m} \sqrt{\frac{1}{T} \int_0^T B^2(t)dt} \quad (9)$$

where $B(t)$ is obtained from the magnetisation curve.

The choice of which existing definition of effective permeability should be used is based on the applications [35]. In addition to the effective permeability approach, a harmonic balance method [36] has been proposed, yielding a moderate calculation effort, but involving a sophisticated reformulation of the finite element equations in the harmonic frequency domain.

When the magnetic field distribution is obtained from the FEA, the core loss can be calculated by the post-processing method, which is based on either loss separation (into hysteresis loss, classical eddy current loss and excessive loss) [37] or curve fitting using the Steinmetz equation. For the latter, several modified types [38] [39], of the Steinmetz equation have been proposed to handle nonsinusoidal excitation. The macroscopic methods [38] [39] enable an efficient post-processing approach to evaluate core loss, based on the waveform of the magnetic flux density. However, since the existing effective magnetic permeability definitions [31] [32] [33] do not reproduce the flux density waveform, they cannot always provide the core loss estimation accurately. Therefore, the conventional definitions of the effective permeability have a restricted applicability for loss evaluation, i.e. the magnetic core should be linear or slightly nonlinear and the excitation should be sinusoidal.

In the magnetic cores of the rotating machine (back of teeth in the stator [40]) and transformers (T-joint of three-limb transformer [41]), the steels can be subjected to a magnetic flux with its

direction rotating (2D excitation). Under 2D magnetisation, the flux density vector rotates in the plane of lamination. The magnitude of the vector can be constant (i.e. isotropic material) or varying (i.e. anisotropy material). The latter has an elliptical loci of B vector (Figure 3.1). The rotational losses can contribute up to 50% of the total magnetic loss in the machines [42].

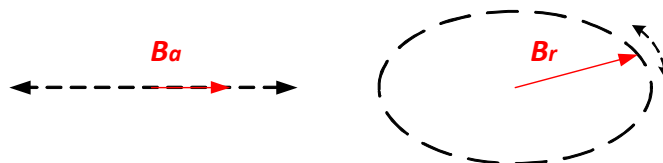


Figure 3.1 Alternating magnetisation (1D magnetisation) and rotating magnetisation (2D magnetisation). Alternating magnetisation has variable magnitude and single direction; rotating magnetisation can have variable magnitude and direction.

As a comparison, the average power loss per unit mass for an alternating magnetization [43], P_a , and for rotational magnetisation [44], P_r , are given by:

$$P_a = \frac{1}{\rho T} \int_0^T \left(\frac{dB_x}{dt} \cdot H_x \right) dt \quad (10)$$

$$P_r = \frac{1}{\rho T} \int_0^T \left(\frac{dB_x}{dt} \cdot H_x + \frac{dB_y}{dt} \cdot H_y \right) dt \quad (11)$$

where ρ is the mass density of the material, T is the period of magnetisation, and $B_{x(y)}$ and $H_{x(y)}$ are the flux density and magnetic field strength in the x(y) direction, respectively.

3.2 Stray losses

3.2.1 Stray loss distribution in power transformers

Control of power loss in a large unit transformer becomes increasingly important to reduce its overall size and minimize the material cost. For designers, strict requirements on guaranteed losses (capitalised by each kW) have been imposed in each component of power systems.

- **Tank**

The stray flux imposing on windings and structural parts gives rise to eddy currents. The major contribution to the stray losses is the structural parts with large exposure areas such as the tank, though the loss density may be low. Hotspots seldom develop in the tank as it is cooled by oil circulating. Additionally, in a large power transformer, magnetic shields are widely used to control the stray loss.

- **Clamping structure**

The clamping structure consists of structural parts like yoke beams and flitch plates. The stray losses in the clamping structure involves relatively smaller area, but the loss density can be high, and result in local hot spot.

The clamping parts are made of mild steel, aluminum or non-magnetic steel, in which the magnetic field and the stray loss distribute differently. The stray flux density in flitch plates is higher than that in the tank. Therefore, the risk of hotspots and local temperature rise is greater though the overall loss in the flitch plates is moderate. Dedicated geometry design (e.g. slots) and proper material selection (e.g. non-magnetic steel) are common practiced to mitigate the excessive stray losses in flitch plates. Non-magnetic material (stainless steel) is sometimes used in the flitch plate to reduce the eddy current loss. However, this material is not recommended for yoke beams since the reduction of stray loss is only possible when the thickness of the structure is sufficiently small.

- **Core edge**

As illustrated in 2.1.2, the loading condition of the transformer has a significant influence on the path of the leakage field. The incident flux on the core surface is considerable due to the closeness of the winding to the core surface. Hotspots may develop if the incident leakage flux density is appreciable. The normal flux (flux impinging normal to the lamination plane) induces eddy current loss on the edge of the core lamination.

- **Windings**

The eddy current loss in the windings is sometimes counted in the stray losses as well. The winding stray losses can be substantially high if the conductor dimensions and transposition methods are not chosen properly [21]. The loss density is higher at the top and bottom ends of the windings due to radial flux [14]. The unbalanced ampere turns of the windings gives rise to the stray loss. For instance, substantial magnetising current, due to either over-excitation or dc-bias, may lead to a local overheat hazard at winding terminals. Therefore, voltage profile and winding connection are important factors for winding stray losses.

The winding stray losses are also influenced by tank and magnetic shunt since they affect the leakage flux path. The winding stray losses might increase when a tank is equipped with magnetic shields shunts. The yoke beams function as magnetic shunts, providing a low reluctance flux path to the leakage flux. The leakage flux penetrated in the yoke beams induces stray loss. However, as the radial leakage flux is minimised, both tank stray loss and the winding stray loss are reduced.

- **Bushing mounting plates**

In furnace transformers and large generator transformers of a large rating where the current in the low voltage side is high, the stray losses in the vicinity of high current conductors can be substantial [21]. For example, if shielding is not sufficient or the magnetic clearance is inadequate, hotspots may develop in the bushing mounting plates. As a mitigation measure, the plates made of mild steel are sometimes replaced with stainless steel to reduce the stray loss.

3.2.2 Stray loss calculation

To estimate and control the stray losses in windings and structural parts in power transformers, an in-depth understanding of the fundamentals of eddy currents is desirable. A lot of work has been done to evaluate stray losses in power transformers. Winding stray loss has been extensively researched and well-documented in many studies. Today, numerical tools (FEM-based) can handle such calculations very accurately and efficiently as the winding material (copper) is linear and its geometry is regular. Likewise, the geometry of bushing mounting plates is symmetric and flux configuration is regular, an analytical approach [45] can be used to determine the magnetic field distribution and its eddy loss.

In the 1980s and 90s, due to the limitations of hardware and computation methods, two-dimensional FE formulations (Cartesian and axisymmetric) [21] were largely used to calculate tank stray losses, and to evaluate the effectiveness of magnetic shielding and shunt and thereby optimise their dimensions. The Reluctance Network Method [46] can also provide fast estimation of tank stray loss and it allows a 3D reluctance modelling taking nonlinearity. Today, the fast development of computers in speed and memory enables 3D FE analysis of eddy current problems in complex structural parts and the accuracy is significantly improved compared to 2D simulations.

Time-harmonic formulation enables an efficient and accurate evaluation of the magnetic field and eddy current loss on the iron surfaces. With a 3D FEM formulation with features of anisotropic modelling, the evaluation of exact stray loss in the core is now also less complicated. Furthermore, the multi-physics function is available in many commercial software packages, with which, EM-Thermal coupled problems can be handled more easily and the temperature rise can be found directly. In the classic time harmonic formulation, the complex diffusion equation is expressed by magnetic vector potential A ,

$$\nabla^2 A = -\mu(\sigma \nabla V + j\omega \sigma A) \quad (12)$$

The terms $\sigma \nabla V$ and $j\omega \sigma A$ represent the source current density vector and the induced current density, respectively. The time-harmonic formulation is computationally efficient, and the required memory is only twice that of the static formulation.

In the one dimensional condition, a conductor surface is represented by $z=0$. Let $z>0$ and $z<0$ represent the regions corresponding to the conductor and perfect loss-free dielectric medium (Figure 3.2). Assume that the vector field H has a component only along the y axis and that H_y is a function of z only.

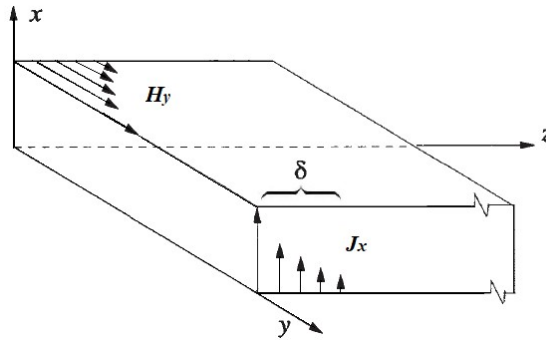


Figure 3.2 Penetration of field and induced current inside a conductor. (from paper V)

According to classic wave propagation theory and Poynting's theorem, the eddy loss in the conductor is expressed as

$$P = \iint_s \mathcal{R}\{Z_i\} \frac{H_m^2}{2} ds \quad (13)$$

where H_m is the amplitude of the surface tangential magnetic field, and the intrinsic impedance is defined as:

$$Z_i = \sqrt{\frac{\omega\mu}{2\sigma}}(1 + j) \quad (14)$$

Despite rapid development of numerical methods and computer hardware, eddy current analysis is still a challenge when the problem is complicated by nonlinearity at magnetic saturation, due to e.g. ferromagnetic resonance and GICs. A transient simulation is still the most reliable and accurate method for non-linear materials. For a transient analysis of eddy current problem involving non-linear material or non-sinusoidal excitations, the problem needs to be solved at each time step, and therefore demands considerable computation efforts. Moreover, calculation of eddy loss in the tank involves a large area (in meters) and a small skin depth (in millimeters), and such computation is memory bounded. Therefore, a fast frequency-domain analysis is still preferred as long as it gives sufficiently accurate estimation. As mentioned, various effective permeability definitions have been proposed [31] [32] [33], which maintain the time-harmonic feature and gives an estimation with sufficient accuracy. Those methods could provide good estimations on the overall equivalent field and the associated power loss in the core itself. However, no research has been conducted into the influence of those definitions on the stray field and associated power losses.

3.3 Problem of excessive losses in power transformers

The lifetime of a transformer is mainly determined by the degradation of insulation inside it. The Montsinger formula has been used to estimate the lifetime, where temperature is considered to be a single factor that affects the aging process

$$t = Ke^{-pT} \quad (15)$$

where K and p are constant, and T is temperature in °C. It is recommended [1] that the rate of aging doubles for each 6°C temperature rise for present day insulation materials. In other words, the lifetime halves with temperature increasing 6°C. The normal operation temperature (average hotspot temperature) at which the insulation of a transformer degrades at the normal rate (allow the transformer service for 30 years) is suggested to be 98°C.

Apart from long-term aging effect, short-time over-loading poses immediate thermal problem if hotspots develop. The permissible overloading period differs for different rating levels of the transformer. For example, 140°C (flash point of oil) is allowed for hot spot temperature in metallic parts in distribution and medium power transformers under normal loading and 120°C for large power transformers [1]. When the transformer core gets saturated (over-excitation), the magnetising current and the level of stray flux increases dramatically. The magnetisation with high frequency harmonic content produces excessive eddy losses in windings and structural parts.

The sources of power losses are mostly the metallic parts in a transformer such as the winding conductor, core steels or structural metalwork. However, the temperature is unlikely to reach a level that damages those metal parts. Instead, it is the adjacent insulation parts such as paper, pressboard and oil that are vulnerable to the temperature rise.

▪ Windings

Resistive loss and eddy loss generates heat in transformer windings. If the heat cannot dissipate timely due to e.g. poor oil circulating, then hotspots may develop in the windings. The winding conductor (copper) can withstand a substantial temperature (a few hundred degree). It is the insulation in the vicinity of the hotspot that deteriorates with increasing temperature. Among the insulation materials, paper is more susceptible to high temperature than transformer oil. The aging speed accelerates significantly for paper above 90°C, whereas oil has a flash point around 140°C [21].

Hotspot temperature, which determines the lifetime of a transformer, is difficult to measure. In reality, the temperature varies depending on oil circulation. One example is that the temperature dependent viscosity becomes poor during the ‘cold start’ (low temperature) and the oil duct may not be able to dissipate the heat generated by the windings in a timely way; consequently, the reduced cooling efficiency means the local temperature rises rapidly.

▪ Core

The core is one of the most significant contributors to the overall power losses in a transformer. When a transformer is subjected to an over-excitation, its magnetic core becomes saturated. There are two major thermal issues related to core saturation. First, the increased flux density produces higher hysteresis loss. However, the overall core loss under dc-bias is considered to be moderate and less severe than ac over-excitation (bidirectional saturation). Moreover, the thermal time constant of the core is typically much longer (above 30 min) than the duration of

the peak GIC, which makes temperature rise insignificant in practice. Another consequence is the leakage flux due to saturation, which can induce excessive stray losses in the tank, windings and structural parts and result in local hotspots. This is considered to be more problematic than the overall core loss.

There is no specific limit in any standards for the temperature rise of transformer cores. The steel of a lamination can withstand a substantially high temperature (a few hundred degree), but the insulation in the vicinity may be affected. For example, the temperature limit for the pressboard is 105°C (which is also the top oil temperature limit under normal cyclic loading conditions) [21].

▪ Structural parts

The leakage flux impinging on the metallic structural parts induces eddy current loss in them. The stray loss in the structural parts is significant for high-rating transformers such as generator transformers, furnace transformers and large autotransformers. The majority of the stray losses take place in the tank. However, the hotspots often develop in the parts with a smaller area such as flitch plates and clamping structures. As mentioned, the high temperature will barely damage the metals; instead, it may seriously deteriorate insulation in the vicinity, thereby affecting the lifetime of the transformer.

Apart from the excitation (voltage) and loading (current) condition of a transformer, the severity of stray losses also depends on the topology of the core and the winding connection. The standard [13] has classified power transformers into four groups based on their susceptibility to the effects of GIC, and it has been widely used as a guideline to select or design power transformers subject to dc current. However, this classification is only valid for GIC with common mode dc currents. Therefore, the consequence of differential mode dc current on stray losses in structural parts must be carefully re-visited.

3.4 Research questions

Power losses are the main drive for the degeneration of insulation system in transformers. In particular, the excessive power losses due to occasional unconventional operation conditions can result in reduced lifetime or even immediate deterioration of the transformer. The three phenomena under investigation as described in Chapters 1 and 2 are highlighted as below.

▪ Over-excitation

Over-excitation voltage, as long as its magnitude is not extremely high (above a certain insulation protection level), seldom leads to a direct insulation breakdown. However, it can introduce a substantial magnetising current, an order of magnitude larger than in normal conditions, which is essentially a thermal issue [47]. Testing transformers at such a high level of voltage/current is risky for the product, instead, numerical simulations are employed to model and identify the risk under different extreme operation conditions [48]. However, studying saturation often involves nonlinear FE analysis with time-domain simulation, which is a well-known numerical challenge. To resolve such problems, frequency-domain methods with effective permeabilities of various types [31] [32] [35] have been introduced. By far, these definitions have a restricted application in the loss evaluation, i.e. the magnetic core should be linear or slightly nonlinear and the excitation should be sinusoidal. It lacks an efficient approach to evaluate the saturation phenomenon in a wider range.

▪ Heavy loading and inductive loading

In power transformers, the laminated iron cores are, in addition to the main flux following the direction of the core, exposed to magnetic leakage flux, which can be significant under high loading. The leakage flux enters the laminated core from different directions, leading to additional power loss in the laminations close to the windings. Depending on the orientation of the leakage flux relative the lamination, different types of losses develop. The leakage flux normal to the plane of the lamination induces eddy currents and thereby generates eddy current loss [49]. The leakage flux perpendicular to the rolling direction (transverse flux) in the plane of the lamination induces additional hysteresis loss. If the transverse flux and the main flux are not in phase, the magnetic field then becomes rotating and generates rotational power loss [17]. Traditionally, loading condition is not considered in core loss assessment, and core loss is considered to be solely determined by the main flux (i.e. flux in the rolling direction). The majority of the previous research focuses on the material characterisation under unidirectional homogenous flux. An assessment of how multidirectional leakage flux influences power losses inside a transformer core is lacking in the literature.

▪ DC magnetisation

The effect of GICs has been a concern for network owners in high latitude countries. Nordic countries are among the countries at higher risk of GIC, with the largest GIC over a few hundred amperes [50]. The Norwegian Water Resources and Energy Directorate (NVE) has therefore

requested that risk analyses be performed by grid operators. GIC may saturate the magnetic core, hence assessing the risk of damage for transformers requires extensive calculations of magnetic fields and the associated stray losses. Thereafter the entire temperature distribution must be evaluated, as the hottest spot in the transformer during a GIC event in general does not coincide with the hottest spot during regular operation.

A direct current in transformers can also be introduced by HVDC systems. Stray currents due to HVDC electrode operations is generated in the neutral grounded transformers, similar to GICs. AC/DC line interaction and HVDC modulation effect create dc current of differential mode.

Since 1989 when a blackout occurred in Canada due to GIC [11], this phenomenon has drawn significant attention. The standard [13] has classified power transformers into four groups based on their susceptibility to effects of GIC, and it has been widely used as a guideline to select or design power transformers subject to dc current. However, the different features (from GIC) of the dc current generated by converter modulation are not addressed in the literature, particularly in a three-phase three-limb transformer where asymmetric dc bias appears in three phases. No experimental investigation on the comparison between the two phenomena has been reported.

Following this literature review of the state-of-the-art and the operation principles of power transformers in various special operation conditions, three research questions arise, summarised as follows:

1) *How can core losses and stray losses under saturation be computed in a more efficient way? Is it possible to avoid time consuming time-domain finite element analysis for nonlinear analyses while maintaining acceptable computation accuracy?*

(Research question 1)

2) *What is the consequence of grid transformers operating under heavy inductive loading considering variation of the leakage flux? Is the core loss really load independent?*

(Research question 2)

3) *What is the consequence of three-phase transformers operating with dc bias induced by different mechanisms? Is the dc bias introduced by converter modulation similar to GICs?*

(Research question 3)

4 Experimental systems and numerical models

This chapter presents a summary of the simulations and lab tests. Details on modelling, analysis and conclusions are elaborated in the appended papers. Two major experimental works are discussed in this chapter.

In electromagnetic calculation, new formulation of effective permeability is proposed to deal with loss evaluation under saturation (nonlinear problem). This part of work answers the research question 1, and the results are summarized in section 4.1.

The first work investigates loss measurement on steel lamination subjected to multidirectional flux. This experimental work is developed to address research question 2, i.e. the influence of leakage flux on core loss. A loss measurement instrument is developed, which enables material characterisation under transverse and normal direction flux. The instrument also allows a replica of actual leakage flux configuration of transformers. Based on this measurement system, the power loss of a laminated core imposed with multidirectional leakage flux under different loading conditions is studied.

The second experimental work examines the power loss under different modes of dc-bias. This experimental work is developed to deal with research question 3, i.e. the influence of dc-bias on power losses. The investigation is based on a three-phase three-limb transformer, where the core loss, winding loss and stray loss are measured. The tests also cover measurement of reactive power and the magnetizing currents. The study reveals an important difference in behavior between common mode and differential mode dc currents in a three-phase transformer. The different configurations of the differential mode are compared extensively, and the worst scenario is then identified.

To gain a physical understanding of the experiment, all the experimental setups (multidirectional flux and dc-bias tests) are modelled by FEM. From the simulation, the spatial distribution and time variation of the eddy current are visualised. Both 2D and 3D models are used in the simulation work. Nonlinear and anisotropic material properties are considered in the implementation of the numerical models. The majority of the simulation is in time domain so as to consider the nonlinear effect. For the simulation involving dc magnetisation, time domain simulation demands significant computation effort due to the long time required to

reach a steady state. To save computation time, the time periodic method is implemented. The simulation results have been compared to the measurement extensively, to validate the numerical models.

4.1 Effective permeability for loss evaluation

Three formulations of effective permeability are proposed for loss evaluation under heavy saturation. The original formulation is defined as

$$\mu_{eff,k} = \frac{\mathcal{F}_k \{B(H_m \sin(\omega t))\}}{H_m} \quad (16)$$

where the $B(H)$ function is the virgin nonlinear magnetisation curve of the material and F_k is the Fourier operator giving the k th Fourier series coefficient. The accuracy of the flux density spectrum calculation can be improved by the introduction of domain decomposition, and modified formulation of effective permeability:

$$\mu_{mf-eff,k} = \frac{\mathcal{F}_k \{B(H(I_m \sin(\omega t)))\}}{\mathcal{F}_1 \{H(I_m \sin(\omega t))\}} \quad (17)$$

where I_m is the amplitude of the input current.

To assist in the division into domains, a dimensionless quantity characterising the degree of nonlinearity (DoN) of the function $B(I)$ is introduced:

$$DoN = \frac{\int_0^{I_{max}} \left| B(H(I)) - B\left(\frac{H_{max}}{I_{max}} I\right) \right| dI}{\int_0^{I_{max}} B\left(\frac{H_{max}}{I_{max}} I\right) dI} \quad (18)$$

where H_{max} and I_{max} are the maximum magnetic field and the maximum input current considered, respectively. To quantify and compare the accuracy of the average flux density calculation using different methods, a spectrum-based error estimation (19) is introduced to characterise the difference relative to the time-domain result:

$$\varepsilon_B = \frac{\sqrt{\sum_{i=1}^n (B_{TD,i} - B_{FD,i})^2}}{B_{TD,1}} \quad (19)$$

where $B_{FD,i}$ is the calculated amplitude of the average flux density at the harmonic order i and $B_{TD,i}$ is the amplitude of the average flux density at the harmonic order i , calculated from a time-domain simulation.

The Fourier method and the domain decomposition approach are validated in 3-dimensional (3D) models, with isotropic (non-grain-oriented, NGO) and anisotropic (grain-oriented, GO) material.

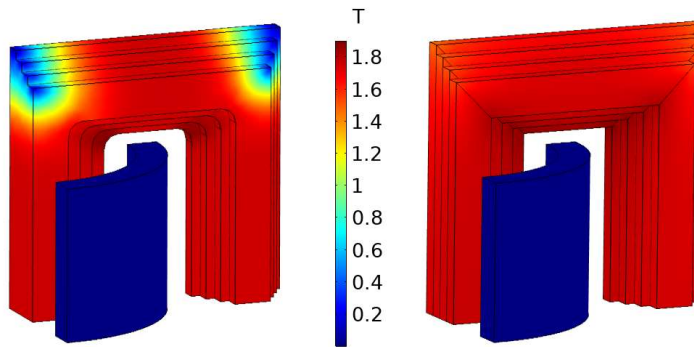


Figure 4.1 Flux density distribution in the transformer core (a quarter model) from a time-domain simulation. (a) Isotropic magnetic core. (b) Anisotropic (grain-oriented) magnetic core. (from paper I)

As shown in Figure 4.1, the flux density distribution is nearly homogenous in the GO core, whereas it is less homogenous in the isotropic core. The Fourier methods (16)(17) are compared to the corresponding time-domain simulation result (Figure 4.2) and the errors are presented in Table 4.1. Due to the homogeneity of the flux distribution in the anisotropic core, the Fourier method (16) gives a sufficiently accurate estimation (Figure 4.2b, $\epsilon_B=0.40\%$) on flux density spectrum without domain decomposition. For the isotropic core, the Fourier method (17) gives a moderately accurate result (Figure 4.2a, $\epsilon_B=3.29\%$). With a single domain decomposition, the accuracy is improved (Figure 4.2b, $\epsilon_B=1.61\%$).

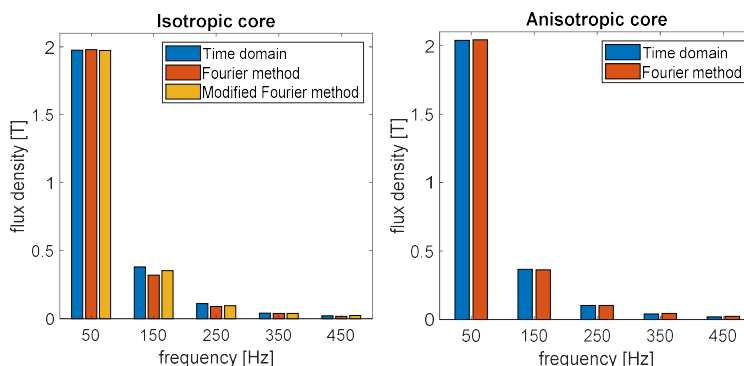


Figure 4.2 Average flux density spectra calculated for the magnetic core with different materials. (a) Isotropic (NGO) magnetic core. (b) Anisotropic (GO) magnetic core. (from paper I)

Excitation current [A]	FM NGO steel	Modified-FM NGO steel	FM GO steel
100	3.29%	1.61%	0.40%

Table 4.1 Error comparison for different core materials. (from paper I)

The definition (17) can be further generalised to nonsinusoidal excitation currents, occurring e.g. at voltage over-excitation. The current in (17) is then defined as a general function $I(t)$. The fundamental component of the resultant magnetic field is used as the denominator in the permeability definition. Hence, the generalised effective permeability becomes:

$$\mu_{gf-eff,k} = \frac{\mathcal{F}_k \{B(H(I(t)))\}}{\mathcal{F}_1 \{H(I(t))\}} \quad (20)$$

Different permeability definitions applied on the core have a significant impact on stray loss calculation. Tank eddy loss as calculated by the Fourier method is compared to other existing methods (7)-(9) as well as the reference time-domain method. As shown in Figure 4.3, when the magnetic core is in the linear or slightly nonlinear region, the different definitions of the effective permeability yield results practically equal to those calculated with the time domain method (maximum deviation <6%). However, when the core is in the heavy saturated region,

the conventional methods largely overestimate the losses. In contrast, the Fourier method (16) gives a good estimation of the stray loss over the whole range.

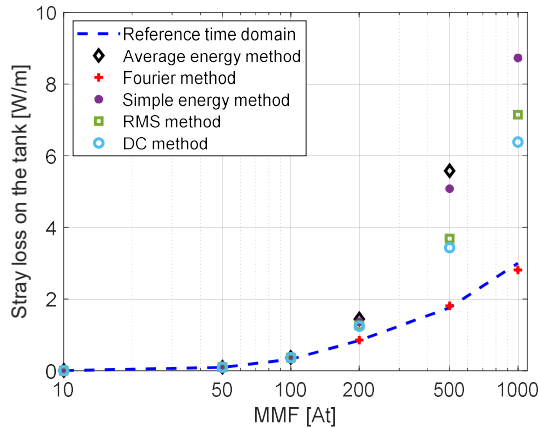


Figure 4.3 Stray loss on the transformer tank wall calculated by various effective permeability methods under different saturation levels. (from paper II)

4.2 Experimental work

4.2.1 Material characterisation

Characterisation of soft magnetic materials is a measurement procedure in which the specimens are subjected to a range of polarisation levels at specified frequencies. The specific losses and relative permeability obtained from the measurement are of great interest for the design and analysis of electric apparatus. In the experiment work, the material characterisation serves as a reference used for finite element analysis, where the specific loss and the relative permeability are the input parameters for material definition. In characterisation of the electrical steels under ac excitation, the standardised methods are used. In characterisation of the electrical steels under ac excitation with dc bias, a new test setup is designed. In addition to the sample measurement, the characterisation can be carried out in a transformer directly if the specimen or the test instrument is not available.

a) Standardised measurements

The Epstein Frame [51] and the Single Sheet Tester (SST) methods [52] are the two standardised methods for measurements of the magnetic properties of electrical steel sheets.

The Epstein Frame consists of four coils into which strips to be tested are inserted and assembled in a square (Figure 4.4). The losses are calculated from the current of the primary winding and the voltage of the secondary winding. In the single sheet tester, the sheet specimen is placed inside two windings (also here the primary winding yields the current and the secondary winding the voltage for the loss calculation) between a double-C laminated yoke (Figure 4.4). In this project, the magnetic property of electric sheet is measured by SST due to availability of the instrument (Brockhaus MPG 100) in the lab. The strips (cold rolled grain oriented electric steel, Grade 30P120, Standard33 JIS 2553, Japan) were cut along the rolling direction (with angle tolerance of 1°), where the edge of the sheet defined the reference direction.

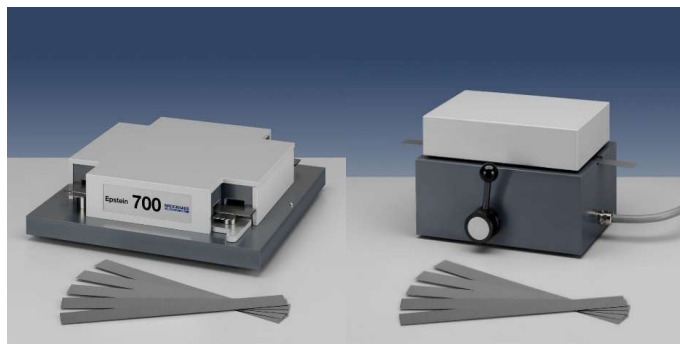


Figure 4.4 Standardised magnetic property measurement devices for electric steels (Brockhaus). Left: Epstein frame tester (according to IEC 60404-2); Right: Single sheet tester (SST, according to IEC 60404-3).

In a wattmeter-based measurement, the secondary voltage $V_{2,rms}$ is calculated from the desired value of magnetic polarisation by:

$$V_{2,rms} = \sqrt{2\pi f N_2 A B_{peak}} \quad (21)$$

where N_2 is the total number of turns of the secondary winding and A is the cross-sectional area of the magnetic core. Since the internal impedance of the voltage measurement is high, the voltage measurement is practically equal to the induced voltage and the power consumed by the instruments in the secondary circuit is negligible. In a measurement, the power supply is tuned until the secondary voltage of the laminated frame reaches the values calculated from the designated flux densities. Then the power losses from the power analyser are recorded. The specific loss P_s is calculated by:

$$P_s = \frac{N_1}{N_2} \frac{P_m}{m} \quad (22)$$

where P_m is the reading from the wattmeter and m is the mass of the sample.

Apart from electric steels, the experimental work also includes a ring shape powder core (Figure 4.5). The magnetic property i.e. the specific loss of the ring core is measured according to [53]. Similar to EPF and SST, the measurement is also a wattmeter-based method. The specific losses are calculated from the current of the primary winding and the voltage of the secondary winding.

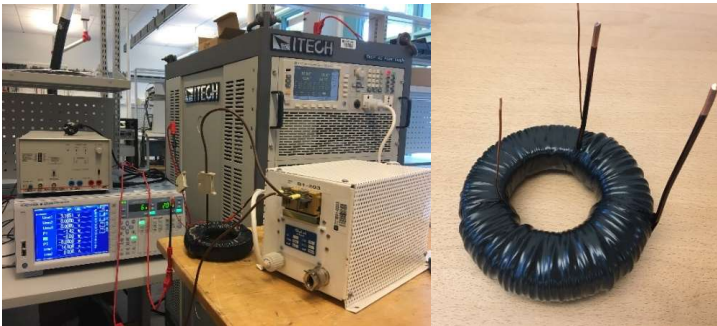


Figure 4.5 Standardised magnetic property measurement for a ring core according to IEC 60404-6.

b) Material characterisation involving dc magnetisation

In both standardised methods (Epstein Frame and SST), the power loss is determined for flux densities with ac symmetric excitation. To fulfil the increasing importance of studying the loss in electrical sheets dc-bias flux, a measurement system based on the wattmeter method and the basic Epstein Frame geometry was developed. The schematic diagram of the loss measurement system under dc-bias is given in Figure 4.6a. Two methods of introducing dc-bias in the flux can be implemented.

In the first method, the voltage offset is added directly from the power supply (Figure 4.6a). In a measurement, the ac voltage source is tuned until the induced secondary voltage of the lamination frame reaches the value calculated from the designated flux density, and the dc voltage offset is tuned until the dc component of the primary current reaches the designated value. Then the power losses from the power analyser are recorded. The advantages of this approach are its simplicity and that it is similar to the real GIC scenario. The disadvantage is

the need for delicate tuning of the dc voltage offset (dc-bias is an order of magnitude smaller than the ac signal due to the low resistance and the high number of turns of the primary winding).

In the second method, a dc flux using a separate excitation coil (Figure 4.6b) is introduced, which enables easy tuning since the dc flux is excited separately. The ac voltage source is tuned in the same way as in method 1, whereas the dc current (corresponding to dc MMF) is directly tuned to the designated value. A large inductance is required to smooth the current induced by the coupling system.

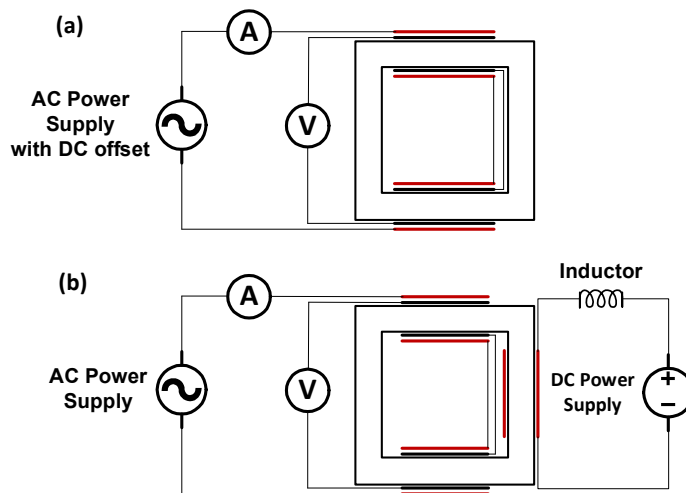


Figure 4.6 Schematic diagram of the loss measurement system under dc-bias. (a) The excitation voltage applied on the primary coil has a small dc-bias. (b) The dc-bias is introduced by a separate coil (on the right) connected to a dc power supply and an inductor for current smoothing. (from paper III)

c) Material characterisation in transformers

The sample of electric steel and its parameters are not always available for transformer users, particularly when it involves a non-standardised test such as dc magnetisation. In a single-phase transformer, this is less problematic since the transformer resembles an Epstein frame measurement system and the magnetic property can be characterised directly on the transformer. However, for three-phase transformers, the standardised test is not applicable as the flux density is not uniform in the core, particularly when dc-bias is involved.

To deal with this situation, a simple method is proposed, which allows uniform flux distribution in the three-phase transformer, and thereby enables a dc-bias test. The winding connection is represented in the schematic diagram in Figure 4.7. The primary windings of the phase A and C (two side-limbs) of the transformer are connected in series and excited by a single-phase voltage source. The secondary windings of the phase A and C are also connected in series as well, used as a voltage measurement winding. In this way, a uniform flux is circulated in the side limbs and yokes (the cross-section areas of yoke and limb shall be identical). In principle, there is no flux flowing in the middle limb. To verify this, the induced voltage in the middle winding is closely monitored.

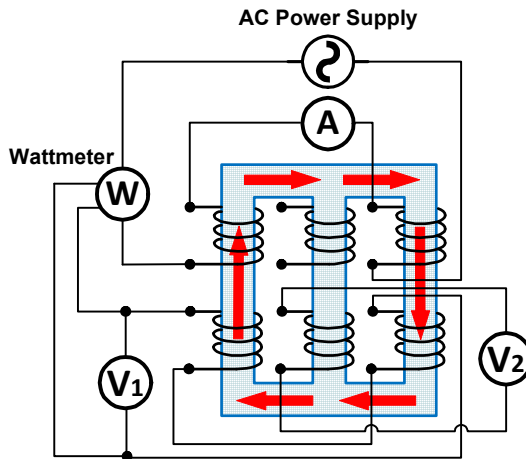


Figure 4.7 Schematic diagram for material magnetisation characterisation using a three-phase three-limb transformer. The red arrow represents the flux path. (from paper VII)

The examples of the material characterisation measurement are presented in Figure 4.8. The specific power losses in an electric steel at rolling direction and orthogonal to rolling direction are measured by standardised SST (Figure 4.8a); relative permeabilities in the two directions (Figure 4.8b) can be obtained by the same instrument (SST). The measured ac magnetisation of the transformer core is presented in Figure 4.8c. The B-H characteristics of the electrical steel in the three-phase transformer under different dc-bias levels is demonstrated in Figure 4.8d. It is evident that the dc flux adds to the amplitude of the ac flux in one half-cycle and subtracts in the other half-cycle, resulting in half-cycle saturation.

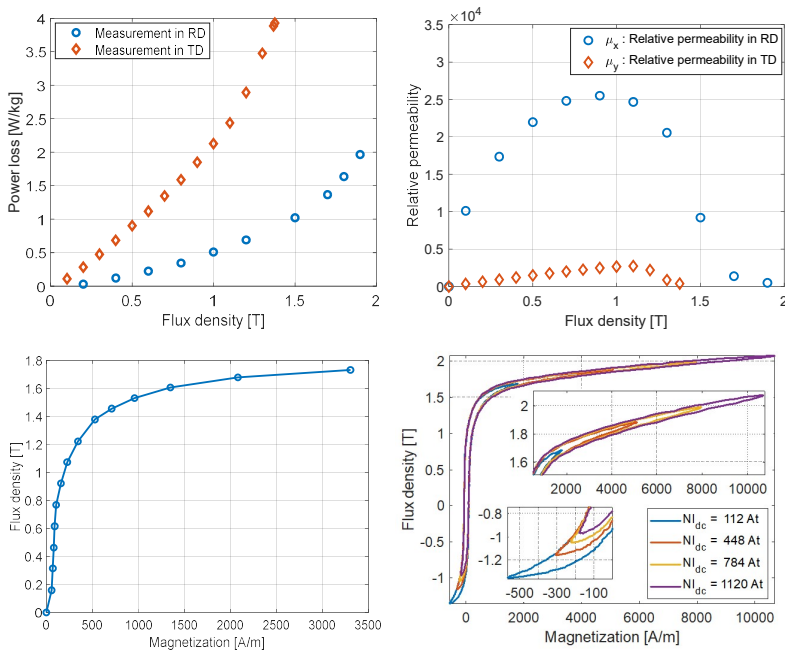


Figure 4.8 The examples of material characterisation (a) The measured power losses in the GO electrical steel versus flux density. (b) The components of the permeability tensor versus flux density measured using the single sheet tester (SST). (μ_x : rolling direction, RD; μ_y : transverse direction, TD). (c) Measured magnetisation characteristic for the transformer core. (d) B-H curve under ac nominal MMF superimposed with multiple dc-bias levels. (from paper III).

4.2.2 Power losses measurement with multidirectional flux

As described in Section 2.1.2, the leakage flux can either be normal or transverse to the core lamination. The leakage flux will add on the main flux and the generated power losses are determined by the superimposed flux. However, the measurement method in 4.1.1, is incapable to cope with multidirectional flux superimposition. To reflect the actual flux configurations, a C-shaped core is introduced to produce an ‘artificial leakage flux’. As shown in the schematic diagram in Figure 4.9, the main flux is generated in an Epstein-like frame with excitation coils and voltage pick-up coils, which is the same as in an Epstein frame. The C-shaped core can be positioned such that it imposes the artificial leakage flux either in TD or ND. Compared to the leakage flux generated by transformer windings, the artificial leakage flux has well defined incident areas, positions and directions, fully controllable magnitudes and phases of the flux densities. The C-shaped core also has primary and secondary windings. The primary windings

of the C-shaped core and the main frame are excited by independent voltage supplies such that their phase angle can be adjusted flexibly. The phase difference is varied from 0° to 90° , corresponding to the operation of inductive and resistive loading of transformers.

In configuration Figure 4.9a, the C-shaped core is mounted on the side of the lamination where the incident flux is in the TD, whereas in configuration Figure 4.9b the C-shaped core is mounted on top of the lamination where the incident flux is in the ND. In a measurement, two power supplies are tuned until the induced secondary voltages of the lamination frame and the C-shaped core reach the values calculated from the designated flux densities. Then the power losses from the power analyser are recorded.

To evaluate the variation in loss due to an added flux, the concept of incremental loss, P_{incr} , is introduced, which is the difference between P_{net} (under superimposed flux) and the arithmetic sum of the loss measured with the individual excitation systems alone (under unidirectional flux).

$$\begin{aligned}
 P_{incr} &= P_{net} - \left(\frac{N_1}{N_2} P_m + \frac{N_1^a}{N_2^a} P_m^a - P_{pow} \right) \\
 &= \frac{N_1}{N_2} (\tilde{P}_m - P_m) + \frac{N_1^a}{N_2^a} (\tilde{P}_m^a - P_m^a)
 \end{aligned} \tag{23}$$

where P_m and P_m^a are the losses of the main excitation system and the auxiliary excitation system measured individually. Note that \tilde{P}_m is different from P_m since it changes with the applied flux.

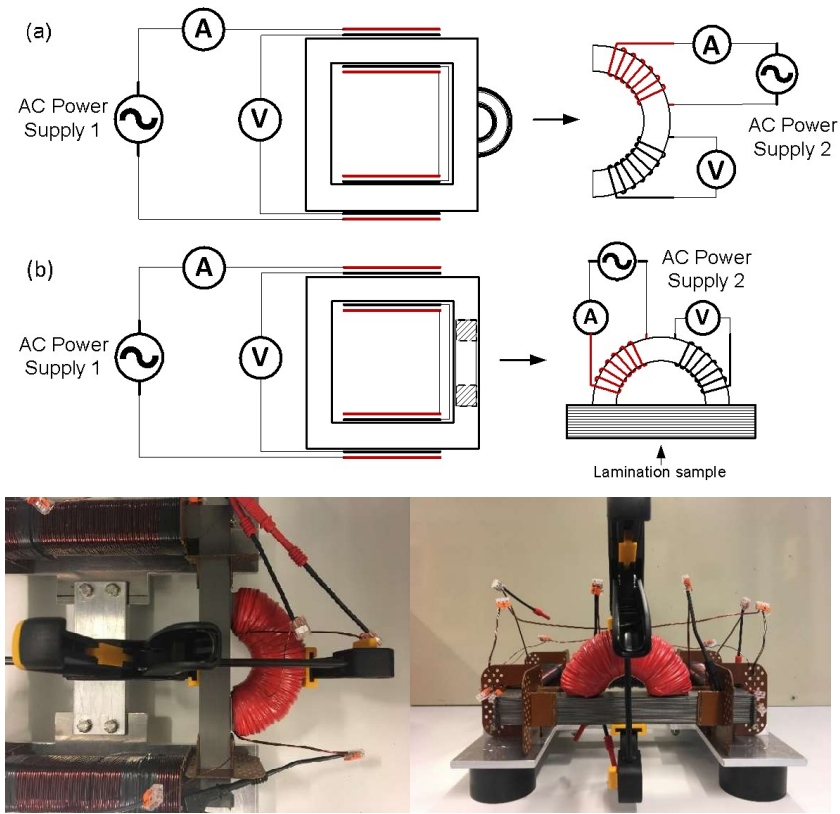


Figure 4.9 Schematic diagram of the loss measurement system with artificial leakage flux superimposed with the main flux. The AC power supply 1 is connected to two coils wound around the square frame and the coil current generates the main flux in the frame. The AC power supply 2 is connected to a coil wound around the C-shaped core and the coil current generates the leakage flux to the lamination. The C-shaped core is mounted either on the side of the lamination (a) for TD flux or on the top of the lamination (b) for ND flux. (from paper III)

Excitation coil	Flux density [T]	RMS voltage range [V]	Excitation current [A]
Laminated frame	0 - 1.6	0 - 62	0 - 0.72
C-shaped core	0 - 0.8	0 - 24	0 - 6.1

Table 4.2 Flux density, voltage and excitation current ranges on the main and the C-shaped core excitation systems. (from paper III)

4.2.3 Measurement of three-phase transformer under dc-bias

A 2.5 kVA three-phase three-limb transformer is used as the test object (Figure 4.10) for dc-bias investigation. The iron tank and the clamping steel can be disassembled so that the core loss and the stray losses (in the tank and the clamping steels) can be separated. Moreover, the tank is specially designed such that the height (i.e. the distance between the magnetic core and the cover/bottom) is adjustable.

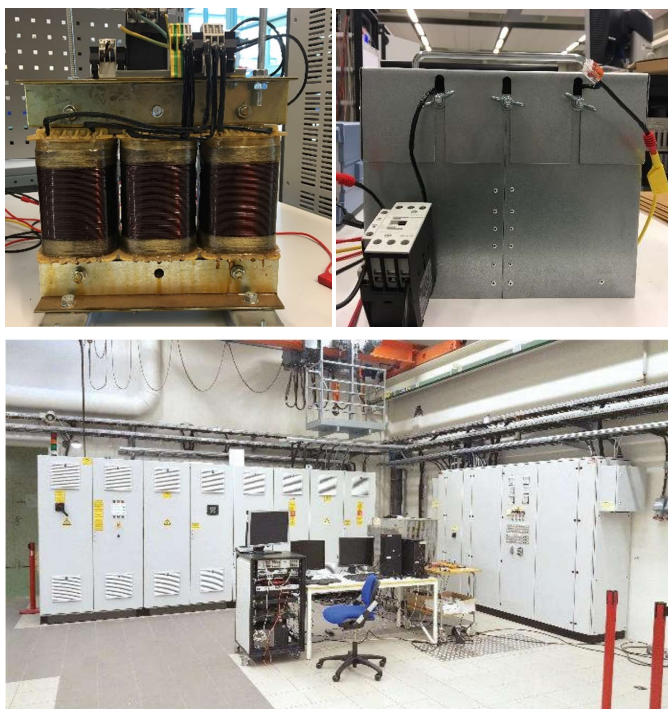


Figure 4.10 A 2.5 kVA three-phase three-limb transformer for dc-bias test and the EGSTON grid emulator (controllable three-phase voltage source) in the National Smart Grid Laboratory (NSGL), Norway. (from paper VII)

The number of turns is 280 for both the primary winding and the secondary winding. The primary windings of the transformer are connected (in star) to a three-phase power supply (the FPGA-based grid emulator, EGSTON®), with independently controllable phases (Figure 4.11). The grid emulator is a reconfigurable switching converter that is able to emulate a power system as ac/dc sources (100 kVA, 400 V_{ac}/800 V_{dc}). The system offers a symmetric ac source with independent, controllable dc voltages. During the test, the dc currents can be tuned precisely to predesignated values, while the nominal ac voltage is maintained. The secondary windings are

connected in delta. A switch is used (Figure 4.11) so that the effect of open circuit and delta connection can be investigated. The current and the voltage in each phase are measured and incorporated into high precision power analyser (YOKOGAWA WT3000) to obtain the power losses.

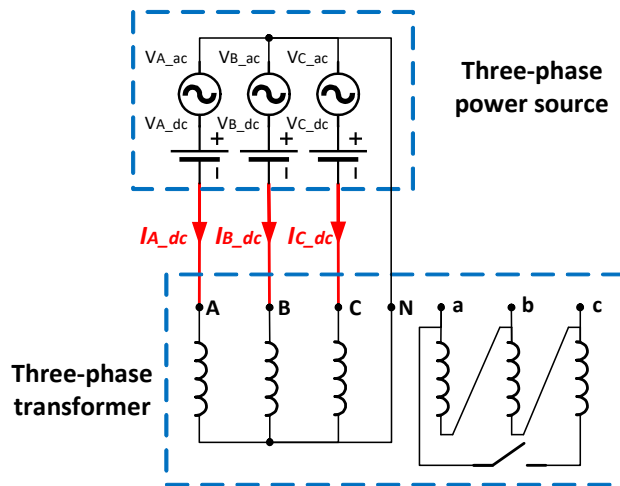


Figure 4.11 Transformer winding connection and dc-bias implementation. (from paper VI)

In common mode test, the dc voltage offsets in all three phases are tuned to be identical and in the same direction. The ac nominal voltage (230 V) is applied on the primary winding and the dc current increases from 0.4 A up to 4 A (Table 4.3). As depicted in Equation (4) and Figure 2.12, the current distribution (of differential mode) in three phases depends on the phase difference between the induced voltage and the switching function of the converter, which can vary even if the magnitude of the induced voltage source is fixed. To identify the worst case in terms of power losses, four scenarios with phase differences varying from 0° to 150° (Figure 4.12) are defined. The ratio and the range of the current applied is listed in Table 4.3. (The applied current in each phase is the multiplication of the current ratio and the current range.)

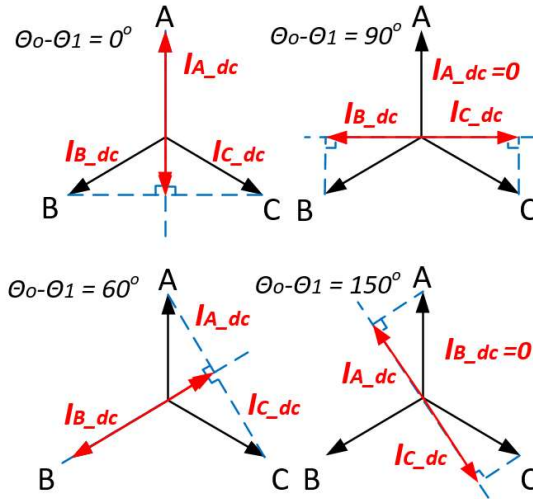


Figure 4.12 A phasor representation of dc current distribution in each phase of scenario 0° , 60° , 90° , 150° . $\theta_0 - \theta_1$ determines the magnitudes of dc current in each phase. (from paper VI)

$\theta_0 - \theta_1$	I_{A_dc}	I_{B_dc}	I_{C_dc}	I_0
DM	1	-0.5	-0.5	0
	0.5	-1	0.5	
	0	$\sqrt{3}/2$	$-\sqrt{3}/2$	
	$\sqrt{3}/2$	0	$-\sqrt{3}/2$	
CM	1	1	1	3

Table 4.3 DC current ratio defined in each phase for loss measurement. (from paper VI)

4.3 Electromagnetic simulations

The measured power losses consist of the loss of different types such as eddy loss and hysteresis loss, which cannot be separated by means of measurement itself. Moreover, the spatial distribution of the power cannot be identified solely by the wattmeter test. To gain a physical insight into the loss distribution associated with different flux configurations (i.e. to visualise the power loss variation in time and space), finite element (FE) models were developed.

4.3.1 Models of multidirectional flux in lamination

The geometry view of the 2D and 3D model of the measurement instrument (4.1.2) is illustrated in Figure 4.13. A 2D FE model (Figure 4.13a) is developed to investigate the TD flux. For eddy current, as the eddy current spacious distribution is three-dimensional, a 3D FE model (Figure 4.13b) is developed to investigate the ND flux.

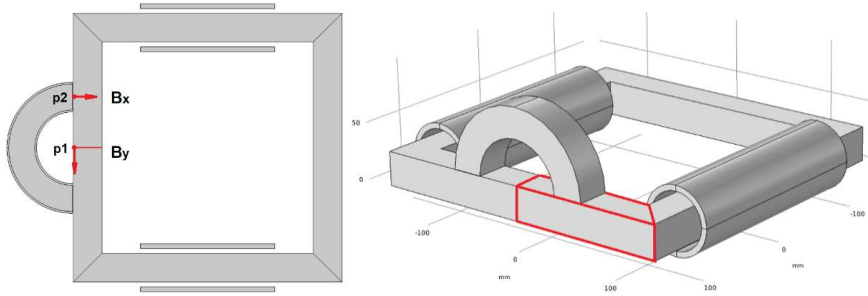


Figure 4.13 The geometry view of the 2D and 3D model. Left: 2D model to study the TD flux and flux superimposition (with RD flux). Right: 3D model to study ND flux and flux superimposition (with RD flux). (from paper IV)

The governing equations for the 3D eddy current field in the steel lamination are expressed in terms of a magnetic vector potential and an electric scalar potential (A, φ - A formulation).

$$\nabla \times \left([\mu]^{-1} \nabla \times A \right) + [\sigma] \left(\frac{\partial A}{\partial t} + \nabla \varphi \right) = 0 \quad (24)$$

$$\nabla \cdot \left\{ -[\sigma] \left(\frac{\partial A}{\partial t} + \nabla \varphi \right) \right\} = 0 \quad (25)$$

where $[\mu]$ and $[\sigma]$ are the tensor of the magnetic (relative) permeability and the conductivity.

$$\mu = \begin{bmatrix} \mu_x(B_x) & 0 & 0 \\ 0 & \mu_y(B_y) & 0 \\ 0 & 0 & \mu_z \end{bmatrix} \quad \sigma = \begin{bmatrix} \sigma_x & 0 & 0 \\ 0 & \sigma_y & 0 \\ 0 & 0 & \sigma_z \end{bmatrix} \quad (26)$$

The homogenisation scheme is implemented in the material definition in 3D finite element models, where the equivalent relative permeability in the ND $\mu_z = 30$ is determined by the stacking factor of the lamination; the equivalent relative permeability in the rolling direction μ_x and orthogonal to rolling direction μ_y is measured by SST (Figure 4.8b); and the equivalent

conductivity in the ND $\sigma_z=2.08 \times 10^2$ S/m is calculated based on the intrinsic conductivity of the electrical steel and the lamination geometry [18].

4.3.2 Models of dc-bias in three-phase transformer

The measured power losses comprise core loss, winding loss and stray loss, which cannot be separated by means of the measurement itself. To gain an insight into the constitution and the spatial distribution of the power losses, finite element (FE) models were developed. Considering the geometry of the transformer, a two-dimensional (2D) FE model is developed to investigate the core loss and a three-dimensional (3D) FE model is used to calculate the stray loss (eddy current loss). The geometry view of the 2D and 3D model is illustrated in Figure 4.14.

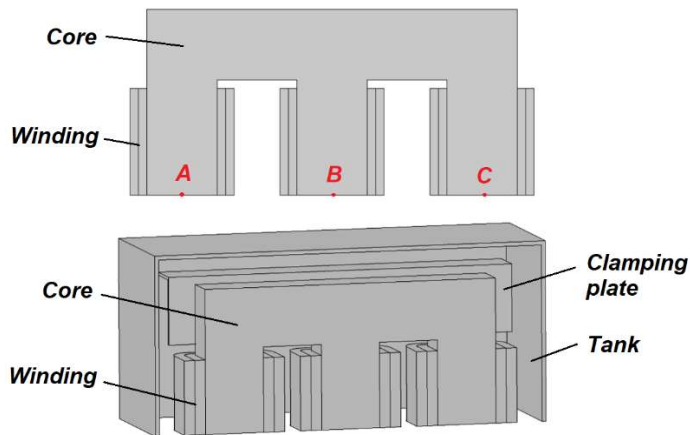


Figure 4.14 View of the geometry model in FE modelling. Upper: 2D FE (half) model for core loss calculation. Lower: 3D FE (quarter) model for stray loss calculation. (from paper VII)

The magnetisation characteristic (Figure 4.8) of the magnetic core used in the FE model is obtained by the approach described in 3.1.1. In normal operation, the leakage flux density is too weak to saturate the tank and the clamping plate; therefore, the constant relative permeability (100) is used for the iron tank and the clamping plate (mild steel), and the conductivity is 6.99 MS/m.

Transient analyses taking into account nonlinear magnetic properties often require significant computation effort to obtain steady state solutions. When the problem involves the dc signal,

the time for reaching the steady state that is determined by the ratio between the inductance and dc resistance and the winding, becomes extremely long. To avoid simulating multiple periods, the 2D time periodic finite element method (TPFEM) is used to calculate magnetising currents and core loss.

The governing equations in terms of a magnetic vector potential A is expressed as:

$$\nabla \times H + \sigma \frac{\partial A}{\partial t} = J_e \quad (27)$$

where J_e is a periodic excitation current (density). When the voltage sources are involved (e.g. 2D FE models), the current density satisfies:

$$J_e = -\sigma \left(\frac{\partial A}{\partial t} + \nabla \phi \right) \quad (28)$$

where ϕ is the electric scalar potential related to the applied voltage sources.

Since we are dealing with a saturation problem, the magnetic field strength H is a nonlinear function of the flux density B .

$$H = H(B) = H(\nabla \times A) \quad (29)$$

To implement TPFEM with commercial simulation codes (COMSOL Multiphysics®), the time domain equation (28) is discretised as multiple coupled stationary simulations:

$$\nabla \times H(\nabla \times A_i) + \sigma \frac{(A_i - A_{i-1})}{2 \frac{T}{N}} = J_{e,i} \Big|_{t=\frac{i}{N}T} \quad (30)$$

where T is the period of the excitation and N is the number of the time steps. A_i and $J_{e,i}$ are the vector potential and excitation current at time step i . Equation (30) represents i discrete equations at specified time instants. In the study, 40 points was used in one period.

For the boundary conditions, the symmetric plane (the bottom plane in Figure 4.14) of the model is defined as a perfect magnetic conductor (i.e. no tangential magnetic field).

$$n \times \vec{H} = 0 \quad (31)$$

Magnetic insulation is defined for the vertical symmetric plane in the 3D model, as well as for the outer boundary of the whole study region.

$$n \times \vec{A} = 0 \quad (32)$$

By integration of (30) over the whole coil cross-section and by expressing the electric scalar potential explicitly by means of applied voltage, a set of ordinary differential equations are obtained (following a similar discretisation approach to (30)).

$$N_t \cdot \vec{J}_{e,i} - \left[V_{dc} + V_m \cdot \sin\left(2\pi \frac{i-1}{N}\right) \right] \cdot \frac{\sigma}{2l} + N_t \cdot \frac{\sigma}{2} \frac{\int (\overline{A}_i - \overline{A}_{i-1}) ds}{2 \frac{T}{N}} = 0 \quad (33)$$

where N_t is the number of the turns, l is the out-of-plane depth, and V_{dc} and V_m are the dc voltage offset and the ac voltage amplitude applied, respectively.

With such implementation, the computation time is greatly reduced. When flux density distribution is obtained, the post-processing approach (lookup table) is adopted to calculate power loss.

For stray loss analyses that involve asymmetric or irregular geometry such as tank and clamping plate, 3D modelling must be conducted. In the 3D FE transient simulations, the obtained magnetising currents from 2D TPFEM are defined as the current excitations [54]. Compared with voltage source implementation, it requires significantly less memory and saves computation time.

5 Results

This section presents a summary of major experimental results. Detailed research analysis and results are further presented in the appended papers.

The experimental work includes power loss measurement and analyses in different tested objects (steel lamination and transformer unit). For the steel lamination, a loss measurement system was developed to investigate the effect of multidirectional flux on power losses. This part of the work answers research question 2, and the results are summarised in section 5.1. In testing the transformer unit, common mode and differential mode dc-bias were introduced and the loss feature under dc-bias of the two modes was studied. This part of work answers research question 3, and the results are summarised in section 5.2.

5.1 Power losses due to multi-directional flux in laminated steels [Paper III, IV,V]

Loss measurements of the electrical steel were performed with the instrument described in 4.2.2, under the combined action of RD main flux and TD leakage flux. The incremental loss is given as a function of phase angle in Figure 5.1. As shown, the incremental loss increases with the magnitudes of the TD flux density as well as the RD flux density. The highest incremental loss occurs when the two fluxes are in phase, whereas the field components act practically independently of each other when the RD and TD fluxes are 90 degrees out of phase. This increment is predominated by the effect of the flux superimposition; namely, a smaller phase difference results in a higher flux density and thereby higher power loss.

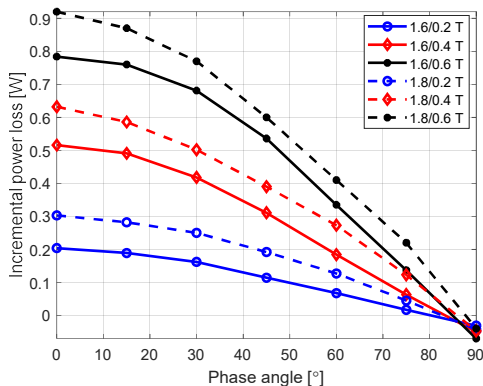


Figure 5.1 Incremental power loss versus phase angle with the main flux superimposed with the transverse flux. The main flux densities are 1.6 T and 1.8 T; the transverse flux density varies from 0.2 T to 0.6 T. (from paper IV)

The measurement is further performed under the combined action of RD main flux and ND flux of varying phase angles. An example of the results is shown in Figure 5.2, where the RD flux density (peak value) was set to 1.6 T and the TD flux was either 0.2 or 0.4 T. Similar to the case of TD flux, the incremental loss induced by the ND flux increases as the phase difference between the two fluxes decreases and there was almost no difference in power when the phase angle is 90 degrees. However, compared to the TD flux density of the same level, the ND flux induces much greater incremental loss at a small phase angle. Moreover, the incremental loss increases disproportionately to the magnitude of the ND flux density.

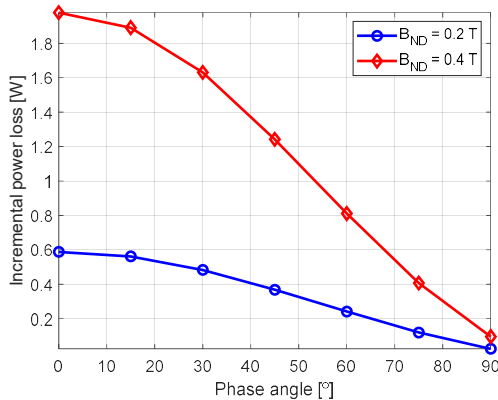


Figure 5.2 Incremental power loss versus phase angle with the main flux superimposed with the normal flux. RD flux density $B_{RD}=1.6$ T; ND flux density and TD flux density are $B_{ND}= 0.2$ or 0.4 T. (from paper IV)

The flux density distribution in the lamination was examined using FE simulations. The simulations were conducted under unidirectional flux (without RD flux in the lamination frame) as well as under flux superimposition of varying phase angles. Figure 5.3 demonstrates the comparison of the flux distribution in the lamination with and without flux superimposition. As such:

- With TD flux alone, the flux turns to parallel to RD along the edge. Due to material anisotropy, the flux concentrates in a narrow flux channel and the magnitude of the RD flux density is significantly larger than the incident ND flux density.
- With RD flux alone, the flux distributes homogeneously in the lamination frame with practically no flux flowing in the C-shape core.
- With superimposing (in phase) with the RD flux, the flux density increases. The resultant flux density under flux superimposition is not the arithmetic sum of two fluxes. Instead, the saturation effect significantly extends the TD flux influence area (global zone). The combined effect of the increased magnitude of the RD flux density as well as the extended area contributes to the loss increment.

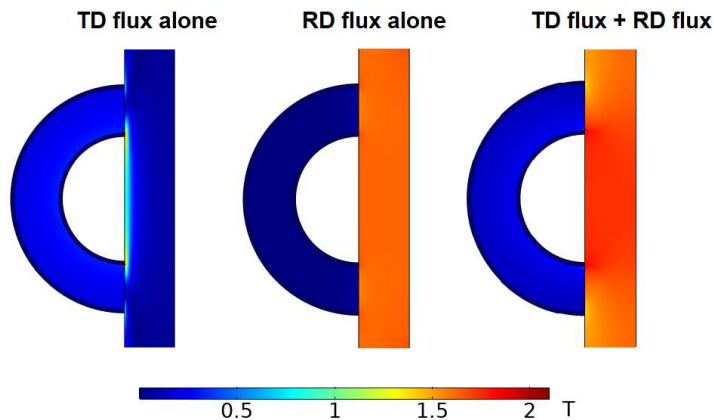


Figure 5.3 Flux distribution in the steel lamination with incident TD alone (Left: $B_{TD}=0.2$ T; $B_{RD}=0$ T), RD alone (Middle: $B_{TD}=0$ T; $B_{RD}=1.6$ T) and with incident TD flux superimposed with RD flux (Right: $B_{TD}=0.2$ T; $B_{RD}=1.6$ T). (from paper IV)

With ND flux superimposed with RD flux, the distribution of the eddy current significantly changes and the phase difference between two fluxes plays an important role in power loss enhancement. Figure 5.4 shows the eddy current distribution under the flux superimposition

between RD flux (1.6 T) and ND flux (0.2 T) at 90° and 0° , respectively. The eddy current is concentrated close to the surface at 90° phase angle. In contrast, at 0° phase angle, the eddy current region is largely extended due to the saturation effect. The extended eddy current volume leads to a significant loss increment.

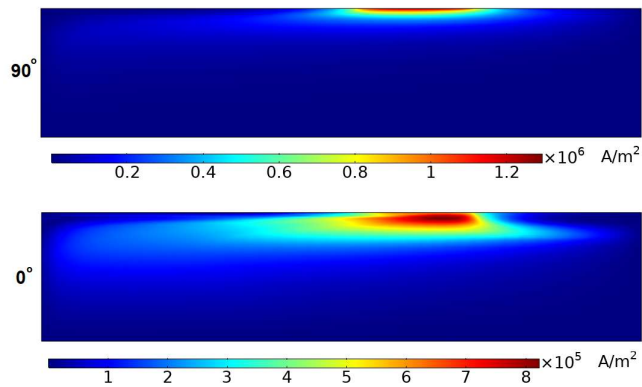


Figure 5.4 The eddy current distribution in the lamination under the ND flux (0.2 T) superimposed with the RD flux (1.6 T) at phase angles of 90° and 0° . (from paper V)

5.2 Common mode and differential mode of dc-bias [Paper VI, VII]

The measurement results of core losses and winding losses are presented in Figure 5.5 and Table 5.1.

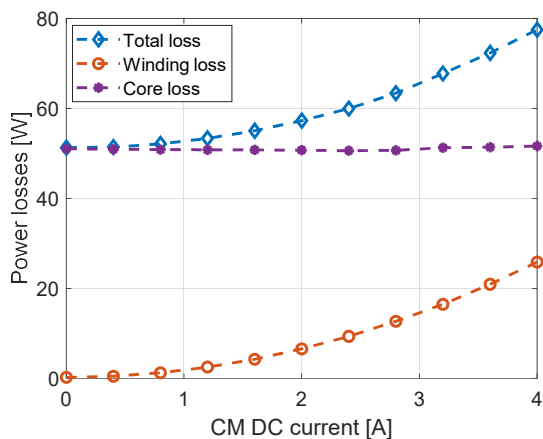


Figure 5.5 Power Losses versus dc-bias of CM. (from paper VI)

As shown in Figure 5.5, the total power loss due to CM currents increases considerably with dc current. The winding loss dominates the loss increment, whereas the core loss remains mostly constant (maximum 2.5% difference among all cases) as dc current increases. Among four different scenarios in CM, the 0° case gives the highest winding loss, although the difference is not significant.

DC current [A]	Losses [W]	0°	60°	90°	150°
0.4	Winding loss	0.79	0.79	0.79	0.74
0.8		2.30	2.16	2.18	2.16
1.2		4.62	4.28	4.39	4.32
1.6		7.70	7.13	7.35	7.29
0.4	Core loss	50.03	49.51	49.66	49.75
0.8		49.81	49.56	49.49	49.47
1.2		49.52	49.58	49.42	49.14
1.6		49.26	49.65	49.40	48.81

Table 5.1 Winding losses and core losses due to DC bias of DM. (from paper VI)

In the next stages of the test, the complete transformer unit is measured (i.e. both the iron tank and the clamping plates are included). The variation of the stray loss and the winding loss is presented in Figure 5.6. As shown, the stray loss increases dramatically with DM dc current, and it differs considerably among the four DM current configurations. In contrast, the winding loss of the four configurations is almost the same.

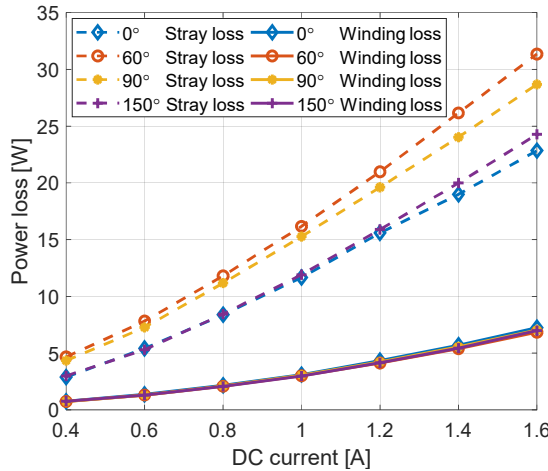


Figure 5.6 Stray loss and winding loss (with both tank and clamping structure) due to DM dc current of four different configurations. (from paper VII)

Figure 5.7 shows the calculated maximum flux density in the transformer core. As shown, the maximum flux densities distribute differently in three-limb transformer for the four DM configurations. The maximum flux densities of DM are significantly higher than that of CM. This is because the DM flux can close its path inside the core. Thereby, it has a low reluctance path for the dc flux of DM and higher flux density offset, whereas the CM flux must close the path outside the core, resulting in a much greater reluctance path and smaller flux density offset.

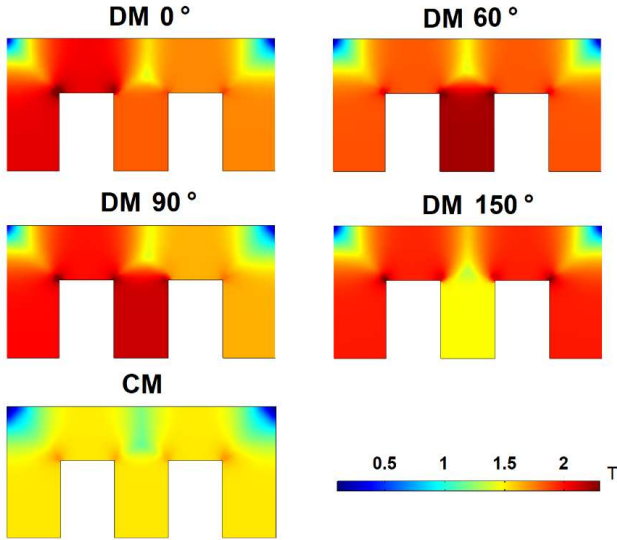


Figure 5.7 The maximum flux density in the magnetic core under 1.6 A DM dc current of four different configurations and 1.6 A CM dc current. (from paper VII)

Figure 5.8 shows the maximum stray loss density in the tank under four configurations. Due to the symmetry, the maximum loss density of 60° and 150° locates symmetrically in the tank. The maximum loss density locates at two sides of the tank for 60° and at the middle of the tank face for 150°. At 0°, the maximum loss density locates at the cover and one side of the tank. At 90°, the maximum loss density locates at one side of the tank. Among the four configurations, the case 60° has the highest loss density, and thereby generates the maximum stray loss.

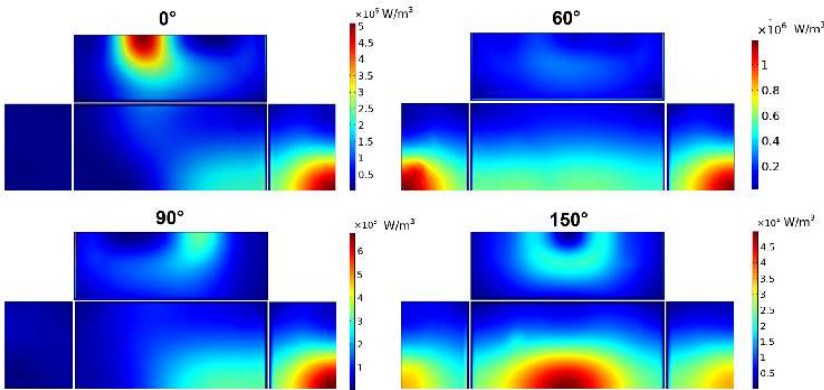


Figure 5.8 The maximum volumetric stray loss density in the tank under 1.2 A DM dc current of four different configurations. (from paper VII)

With delta winding, the stray loss dramatically reduces with little additional loss in the delta winding (Figure 5.9). This implies a delta winding could be a potential mitigation measure to control the extra loss induced by DM dc-bias.

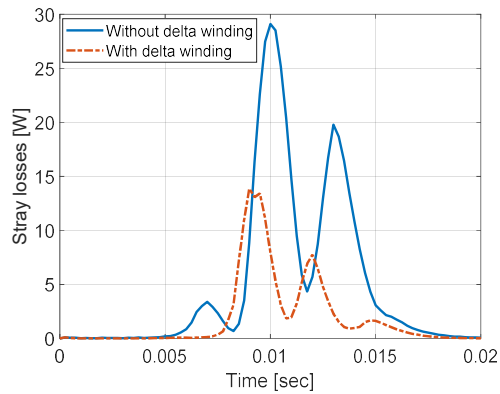


Figure 5.9 The calculated instantaneous stray loss over one period in the tank under 1.2 A DM dc current at the configuration of 0° . (from paper VII)

6 Discussions

6.1 Finite element loss calculation using effective permeability — in answer to research question 1

In the finite element calculation, new formulations of effective permeability are proposed to deal with loss evaluation under saturation. The approaches are based on the Fourier method and time-harmonic representation. Together with the macroscopic methods [38] [55] [56] [57] [39], it enables a more efficient post-processing approach for evaluating core loss under a large range of saturation conditions. Furthermore, the proposed method yields higher accuracy in calculating stray loss under heavy saturation.

The well-established macroscopic methods claim good accuracy in evaluating core loss. In particular, some modified types [38]- [39] are able to handle saturation conditions and nonsinusoidal excitation quite accurately. In the formulation of the modified Steimeltz equation [57] and the generalised Steimeltz equation [38], the flux density and its time-derivative are the only required inputs (other coefficients are obtained by material characterisation). Therefore, the remaining challenge is to obtain accurate flux density distribution under those conditions. The best candidate to resolve such a problem is the finite element method. For the sake of computation efficiency, the time-harmonic formulation with effective permeability is preferred. However, the existing effective permeability definitions [31] [32] [33] do not reproduce the flux density waveform accurately enough, due to their single equivalent approach. Therefore, the conventional definitions of the effective permeability have a restricted applicability for core loss evaluation, i.e. the magnetic core must be linear or slightly nonlinear. This also applies to stray losses evaluation as demonstrated in the study.

Unlike the conventional methods that only provide a single equivalent field, the proposed method preserves the full information of the magnetic field spectrum. In that way, it is possible to reduce the error of the flux density prediction considerably. Furthermore, since the time-harmonic feature is maintained, the system size (memory requirement) and the computation effort are significantly lower compared to the harmonic balance method and the time-periodic FEM. The only cost is the pre-processing of the magnetisation curve, which do not increase computation time since it is done off-line.

6.2 Effect of leakage flux on core losses in power transformer — in answer to research question 2

To investigate the influence of multidirectional leakage flux on the core loss, a loss measurement system is developed, and the actual leakage flux configurations are emulated experimentally and analysed numerically. The importance of the loading condition (i.e. phase angle) is highlighted. It is evident that the loading condition has a significant influence on local eddy current loss as well as the overall power losses in a magnetic core, due to penetrated leakage flux. This contradicts the statement of classic textbooks that the core loss is load independent, based on which the core loss is measured at no load test as the common practice. In this thesis, it is pointed out such a statement is valid when the loading angle is close to 90 degree.

The leakage flux influence area in the core lamination of a transformer has been categorised into local zone and global zone in 2.1.2. The associated loss characteristic was evaluated comprehensively.

▪ Local zone

Due to the high permeability of the ferromagnetic material, the leakage flux enters into the iron core perpendicularly, either normal to the lamination plane (ND) or in the lamination plane but transverse to the rolling direction (TD).

The induced loss associated with ND is eddy current loss and the induced loss associated with TD is the rotational power loss. Compared to the loss in the RD, the eddy current loss and the rotational loss produce much higher loss density (per volume); therefore, they potentially lead to local hotspot hazards. This has been confirmed experimentally and numerically. For instance, the eddy current loss increases rapidly with the magnitude of the ND flux density. More importantly, it has been determined that the phase angle between the RD flux (main flux) and the ND flux also plays a significant role in the eddy current loss.

The influence of the TD flux on power loss has been investigated. The existence of rotational power loss due to added flux in TD in the core has been demonstrated. This suggests that the TD flux induces significantly larger power loss density than RD flux of the same flux density level. However, the measurement as well as the finite element calculation shows that the contribution of rotational power loss to the total loss is negligible due to the small volume

involved. Although it has much higher power density than that generated by the flux in the rolling direction, the loss density is not high enough to develop a hot spot.

- **Global zone**

The penetrated flux inside the core lamination is largely dominated by the flux parallel to the main flux (in RD), which circulates along the edge of the core window. This flux path constitutes the global zone. Apparently, the area of the global zone is much larger than the local zone. Since the flux involved in the global zone is in RD, the eddy current is limited by the lamination structure. Thus, the hysteresis loss and anomalous losses dominate the power losses. Although these losses can hardly be attributed to any local hot spot, they may considerably contribute to the overall power losses at inductive loading, due to the increased magnitude of the resultant flux density and the larger volume it involves.

6.3 Influence of dc-bias on power transformer — in answer to research question 3

The concept of common mode (CM) and differential mode (DM) is introduced to distinguish dc-bias in a three-phase transformer caused by GIC and converter modulation. The tests on a three-phase transformer reveal that there is a significant difference between the common mode and differential mode dc-bias in terms of power losses and reactive power consumptions. Differential mode dc-bias induced significantly larger stray losses than that of common mode, regardless of the magnetic core topology. Four configurations of DM are defined according to dc current distribution in the three phases. The core loss, winding loss and the stray loss are compared.

- **Stray losses**

Unlike CM dc current, DM dc currents have low reluctance regardless of core topology, and therefore the flux density offset is more sensitive to DM dc current. As a result, the magnetising currents of DM are significantly larger than CM, leading to higher stray losses.

The stray losses induced by high-level DM dc currents differs with four configurations. As expected, the geometry of the tank and the clamping has a dramatic impact on the stray loss.

- **Core losses**

Unlike stray losses, the core loss is not sensitive to dc-bias, regardless of the magnitudes and modes of the applied dc currents.

▪ Winding losses

The winding losses due to DM dc-bias are significantly larger than that of CM, due to high magnitudes of the magnetising currents as well as their high frequency harmonic contents. Difference in winding losses among the four configurations have been noticed, but the difference is not significant.

Based on the above facts, it can be concluded that the power losses in the three-phase three-limb transformer are susceptible to DM dc current, but not sensitive to CM dc currents. In fact, any types of three-phase transformer (five-limb or four-limb) are susceptible to DM dc current since it always has a low reluctance path in the core.

Lastly, it has been found that the delta winding can significantly reduce the stray loss caused by the DM dc currents. This implies that a delta winding can be a practical mitigation measure to reduce excessive loss (as well as noise) induced by the DM dc current. A large transformer is often equipped with delta windings, either for stabilising or for auxiliary power supply. Therefore, the stray losses due to DM current have been minimised. In such cases, attention should be paid to the rating of the delta winding since the circulating current can be substantial if the dc unbalance is significant.

Apart from power losses, the DM dc currents also enhance the reactive power consumption and introduce an unbalanced voltage distribution in three phases, which could be an issue for voltage protection.

6.4 Limitations and source of the errors

In this PhD research project, the majority of the investigation on power losses were studied experimentally. Errors caused by instrumentation, sample preparation, environment, experiment design and procedure are inevitable. The significant contributors to these errors are as follows.

In the standardised tests (Epstein frame test and Single sheet test), errors introduced by instrumentation and measurement procedure were largely minimised as high precision devices (Brockhaus MPG 100 and YOKOGAWA WT3000) were used and the standardised procedures

[51] [52] [53] were followed. In the sample (electrical steel) preparation, the cross-sectional area determines the actual flux density as well as the specific loss. However, there was a large deviation (10%) of the individual sheet thickness from the nominal value (see Figure 6.1); therefore, neither the nominal value nor the single measured value are suitable for defining the cross-sectional area. Instead, a statistically reliable effective cross-sectional area, A , is used to minimise the error caused by this deviation.

$$A = \frac{m}{4l\rho} \quad (34)$$

where m is the total mass of the test specimen, l is the length of a test specimen strip and ρ is the mass density (7.65 kg/dm³ for 30P12033).

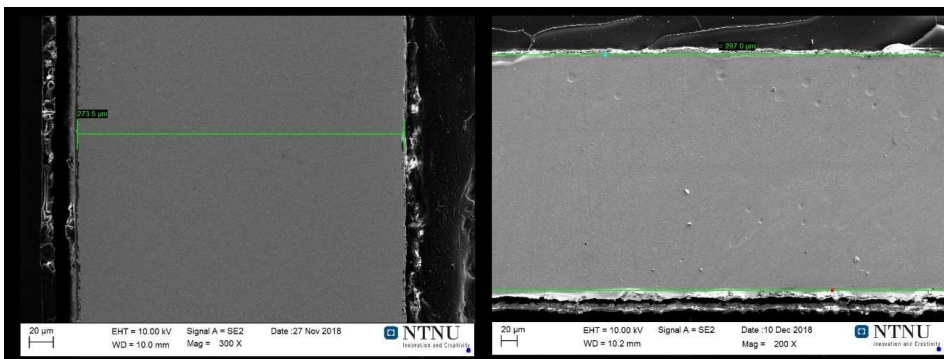


Figure 6.1 The cross-section (observed by Scan Electronic Microscope) of the electric steel used in the square frame. The thickness of the sheet can vary almost by 10% in one single batch.

In the multidirectional flux tests, a loss measurement instrument was developed with multi-purposes. It was mainly used for emulating leakage flux in a transformer but also allowed for the characterisation of ac flux with dc-bias.

In the former application, errors were mainly related to the power loss in the auxiliary ring core. According to (23), the accuracy of the incremental power loss relies on the perfect cancelling of the power loss in the auxiliary ring core. For instance, the variation of incremental loss in the lamination at 1.6/0.4 T is 0.5 W (Figure 5.1), which is at the same level as the loss in the C-core (0.47 W). This indicates the variation of the power loss in the C-core (e.g. 5%) can contribute to the error in the incremental loss (ca. 5%) considerably. To reduce errors from the auxiliary ring core, selecting low loss material is crucial for future improvement.

The permeability of the powder core ($\mu_r=125$) is much lower than that of GO steel ($\mu_r>12000$), therefore the impact of the main flux on the powder core is negligible ($<1\%$) when the GO steel works in its linear region. However, in the measurement where the flux superimposition takes place, the permeability of the GO steel reduces considerably. Consequently, the stray flux from the frame can enter the auxiliary core and influence the measured power loss. To minimise the measurement error introduced by the flux interaction, 1 mm thick plastic spacers (see Figure 6.2) were used to magnetically insulate the main frame flux from the saturated GO steels.

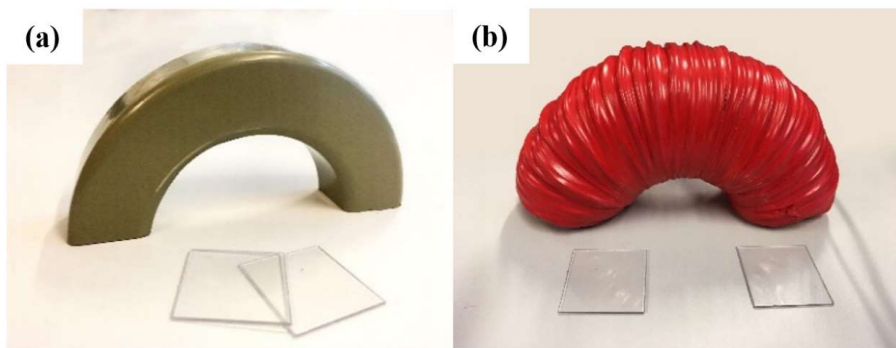


Figure 6.2 The C-shaped core and the excitation system. (a) The C-shaped core (CSC) was made by a half ring unit. (b) The excitation and voltage pickup coils were wound around the CSC. Plastic spacers were used to create air gaps. (from paper III)

Two notched ring cores (NRCs) have been used to characterise the rotational power loss associated with TD flux (Paper III). However, the transverse flux distribution is less homogeneous at the ends of the frame volume (measurement volume) covered by the NRC. To counteract the effect of the flux inhomogeneity, two NRCs have been assembled with different dimensions, one NRC comprising three units of the rings and the other five units (see Figure 6.3). The loss contributed by the inhomogeneity is then, minimised by subtracting the measurement using the three-unit NRC from the measurement using the five-unit NRC. The difference between the two measurements is, therefore, the contribution from the TD flux area of two units in the middle where the flux is practically homogeneous (effective volume). The described wattmeter-based approach still has its inherent limitation in the accuracy of the rotational power loss measurement. Instead, the field-based magnetisation method [17] focuses

on the local homogeneous magnetisation area and enables localised field measurement, which becomes a more favourable solution for 2D magnetisation measurement.

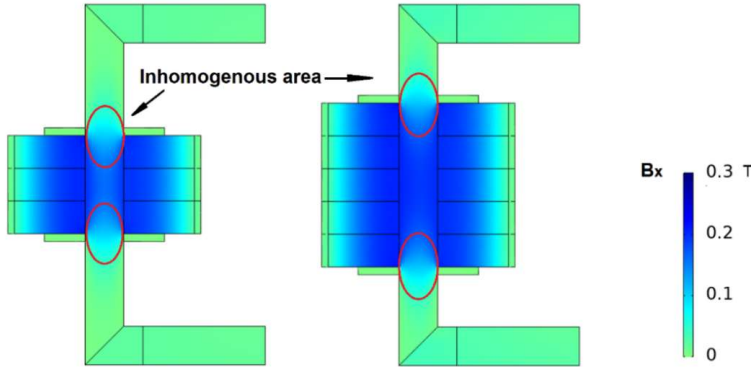


Figure 6.3 The transverse flux distribution (flux density in the horizontal direction, B_x) in the lamination. The end (inhomogeneity) effect is cancelled out by subtracting the measurement of the three-unit core from the measurement of the five-unit core (from paper III)

In the dc-bias tests on the transformer, the experiment was carried out on a down-scaled lab transformer, as it is impractical to perform such potentially destructive tests on a full-size grid transformer. In principle, the saturation phenomenon is characterised by the flux density in the magnetic core. According to Ampere’s law, the magnetomotive force (defined as NI in ampere-turns) is:

$$NI = Hl \tag{35}$$

where N is number of turns, I is current, H is magnetic field strength and l is mean length of the flux path. Then the flux density can be simply expressed by:

$$B = \mu H = \mu \frac{NI}{l} \tag{36}$$

where μ is magnetic permeability of the core.

To preserve the flux density feature, the scaled experiment maintains the same topology of the core and keeps N/l approximately at the same level as a full-scale transformer. Despite the similarity in flux density distribution between the lab transformer and full-scale transformer, it is imperative to highlight the important differences between them:

- Large (full-scale) transformers have sophisticated structural steels such as flitch plates close to the magnetic core which are susceptible to the leakage flux affected by saturation.
- The core material used in a grid (full-scale) transformer is often the grain-oriented steel, which has higher nominal flux density, lower specific loss and steeper magnetisation curve below the knee point, compared to the lab transformer which is made of non-grain-oriented steel.
- The rated current in a full-scale transformer is much larger than the lab transformer, so the winding loss generated under the same dc current in a full-scale transformer is not as problematic as the small one, since the percentage current increase (relative to nominal load current) in a full-scale transformer is much less significant.

The pros and cons have been discussed for the two methods (voltage source and current source) of introducing dc-bias. The errors of the two methods were related to the sensitiveness to the dc voltage tuning and the ripple of dc current (<5% in this experiment). Therefore, delicate control of dc voltage and larger inductance were required to increase accuracy for the two methods. Besides the limitation of the hardware, the way to derive dc flux density is indirect and may introduce some errors. In this approach, the ac over-excitation test result was used as a reference, i.e. a $B-I_{peak}$ characteristic curve. I_{peak} obtained from the dc-bias test was compared to the preserved $B-I_{peak}$ curve, where the maximum flux density B_{max} was identified. Since the peak-to-peak flux density was obtained by the ac voltage source, the dc-bias was calculated by:

$$\Delta B = B_{max} - B_{ac} \quad (37)$$

where B_{ac} corresponds to the applied ac voltage. This comparative method can be improved by incorporating more advanced pattern recognition methods or by a direct measurement method such as a Hall effect sensor.

Except from the errors in the experiment, errors can emerge in the numerical simulations due to parameter specification, geometry simplification, coarse mesh and time stepping, plus the various assumption made in the calculations. For example, in the calculation of the stray loss of the three-phase transformer, there was a relatively larger difference (max. 10%) between the calculated values and the measured values. This was because of the coarse model for the tank and clamping parts, for instance, the riveting, slotting, coating and holes (Figure 4.10) were ignored in the finite element model (Figure 4.14). In practice, these aspects have considerable impact on stray flux distribution in the tank and thereby the stray losses.

In the calculation of the rotational power loss by finite element analysis, the following approach is implemented as suggested by the literature [58]. The rotational power loss is calculated by the sum of the losses in two orthogonal directions:

$$P_{tot} = \int_V \left[P_x(\max_T(B_x)) + P_y(\max_T(B_y)) \right] dV \quad (38)$$

where $P_x(B)$ and $P_y(B)$ are the specific loss density with respect to the peak flux density in TD and RD, respectively. This approach is an approximation, disregarding the phase between the two fluxes, which may lead to errors. The remedy might be adoption of more sophisticated hysteresis models [17] or conducting massive 2D magnetisation measurements considering both magnitudes and phases simultaneously.

In the calculation of the magnetisation current of the three-phase transformer, the tank was ignored to save computation time. For DM mode dc current, this simplification has little influence on the accuracy. However, for CM mode dc current, there is a CM flux path from the core to the tank; therefore, ignoring the tank leads to some errors in the magnetisation current, which can be observed in Figure 6.4.

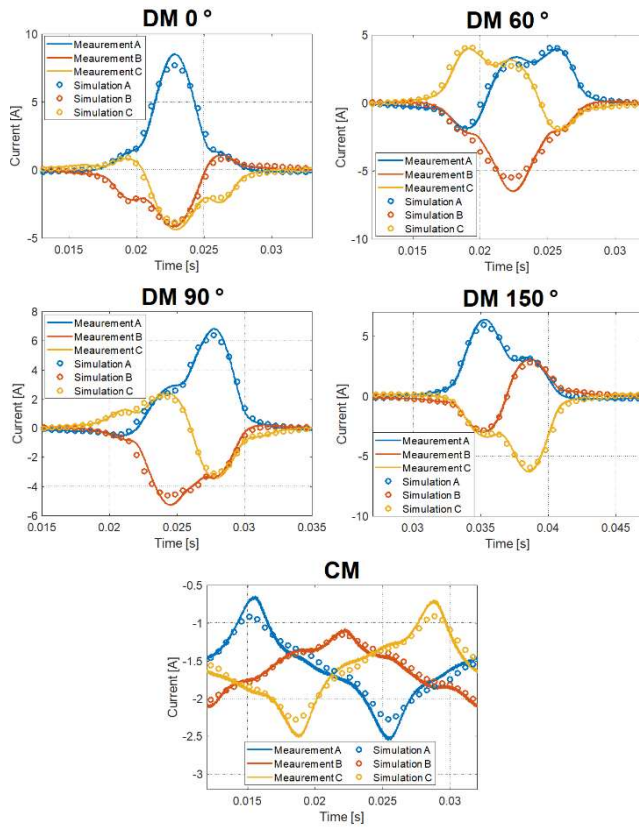


Figure 6.4 Comparison of the measured and calculated primary phase currents over one period at 1.6 A dc current for the four different DM cases and for the CM case. (from paper VII).

7 Conclusions

The research work is summarised in this chapter. Concluding remarks and suggestions for future work are presented.

7.1 Concluding remarks

In this PhD research work, power transformer under special operation conditions were studied with newly developed experiments, instruments and numerical methods.

New formulations of effective permeability were proposed for the calculation of flux density in a transformer core under various saturation levels, isotropic/anisotropic materials and sinusoidal/nonsinusoidal excitations. The proposed method is more efficient than the time-domain method and yields significantly higher accuracy in stray loss calculation under heavy saturation than energy-based methods.

The loss measurement under multidirectional stray flux has revealed that the loading conditions have a significant impact on both local eddy current loss and the overall power loss in the core. Under inductive loading, the core loss is actually load dependent and the conventional no-load tests can underestimate the core losses considerably. Furthermore, the eddy loss due to normal leakage flux can create hot spots under heavy, inductive loading. In contrast, the rotational power loss, as a result of added transverse flux, barely causes any hot spots because of its small volume and bounded loss density.

The dc-bias tests have identified a dramatic difference between the common mode and differential mode in terms of winding loss and stray loss. Differential mode dc-bias induced significantly larger stray loss and winding loss than that of common mode, regardless of the core topology. Moreover, DM dc current raised the reactive power consumption and introduced voltage unbalance in the three phases. Therefore, the risk of dc magnetisation due to the modulation effect of HVDC converters on both the equipment and the power system was highlighted.

7.2 Recommendations for Future Work

In this PhD research project, magnetic field distribution and associated power losses were studied. Thermal impact has been discussed but not investigated. Performing EM-Thermal coupled simulations to evaluate temperature rise in different components would be a beneficial next step. The viscosity of transformer oil is strongly temperature dependent and can vary significantly under some circumstances (e.g. cold energization). In that case, an EM-hydraulic coupling should be taken into account to obtain correct resultant temperature, which is essential for dynamic thermal modelling.

In the dc-bias investigation, the system-oriented simulation was performed. Although the mechanism of harmonic transfer is not within the scope of this study, the importance of control function in the resultant dc current should be addressed. Converter internal impedance seen from the dc side is strongly affected by converter control, particularly in voltage-source converter. For example, the circulating current control (or any low pass active filter) used in MMC behaves like a resistor seen from the induced voltage source and the resistance is determined by the gain of the controller. Therefore, the dc current derived by the analytical approach [19] without considering the control effect may not be valid in practice. This also implies that control functionality, instead of physical apparatus, can be a potential mitigation measure to minimise dc-bias on the transformer bus.

In the dc-bias study, the test object was a three-phase three-limb transformer. This type of core was chosen because of the distinction between CM and DM dc current in a three-limb transformer. There are many other three-phase core topologies such as five limb, in which the dc magnetisation phenomena might be more complex. Nevertheless, the methodology and numerical approach developed in this research project can easily apply to transformers of other types.

In FE simulation of transformers, the time periodic method is successfully implemented and provides efficient and accurate analysis of magnetising current and core loss in 2D. However, in dealing with 3D problems, significant memory and computation time is demanded (>200 GB, exceeding the limitation of server). To resolve this problem, the 2D-3D hybrid approach has been used. In a future work, it would be worthwhile to use the original formality (voltage source and TPFEM) and calculate with brutal computation force (cluster), and to make a rigorous comparison with the hybrid approach.

The well-established macroscopic methods claim good accuracy in calculation of core losses, as long as the flux density and its time-derivative are available. Therefore, in developing a numerical method for core loss calculation, the effort is spent on flux density calculation, particularly under the heavy saturation condition. This method has been extensively validated by comparison with the time-domain method. However, it is imperative to incorporate the method (Fourier-based effective permeability) with the modified Steimeltz equation [57] or the generalised Steimeltz equation [38] to validate the whole process with lab tests under various excitation conditions. Furthermore, various hysteresis models have been proposed in recent decades. It would be interesting to implement dedicate hysteresis models in the FE simulation to investigate the hysteresis effect, instead of using post-processing (the curve fitting approach), which is largely based on sample material characterisation.

Bibliography

- [1] "Power transformers - Part 7: Loading guide for mineral-oil-immersed power transformers," IEC 60076-7, 2018.
- [2] https://commons.wikimedia.org/wiki/File:Large_power_transformer.jpg.
- [3] "IEEE Guide for Loading Mineral-Oil-Immersed Transformers and Step-Voltage Regulators," IEEE Standard C57.91, New York, 2011.
- [4] M. J. Heathcote, J & P Transformer Book, Elsevier Science, 2011.
- [5] R. Girgis and C. D. Ko, "Calculation techniques and results of effects of GIC currents as applied to large power transformers," *IEEE Transactions on Power Delivery*, vol. 7, no. 2, pp. 699-705, 1992.
- [6] R. Pirjola, "Geomagnetically induced currents during magnetic storms," *IEEE Transactions on Plasma Science*, vol. 28, no. 6, pp. 1867-1873, 2000.
- [7] P. Price, "Geomagnetically induced current effects on transformers," *IEEE Transactions on Power Delivery*, vol. 17, no. 4, pp. 1002-1008, 2002.
- [8] J. Ulleryd, M. Ye and G. Moreau,, "Fundamental frequency coupling between HVAC and HVDC lines in the Quebec-New England multiterminal system-comparison between field measurements and EMTDC simulations," in *International Conference on Power System Technology (POWERCON)*, 1998.
- [9] E. V. Larsen, R. A. Walling and C. J. Bridenbaugh,, "Parallel AC/DC transmission lines steady-state induction issues," *IEEE Transactions on Power Delivery*, vol. 4, no. 1, pp. 667-673, 1989.

- [10] Y. Jiang and A. Ekström, "General analysis of harmonic transfer through converters," *IEEE Transaction on Power Electronics*, vol. 12, no. 2, pp. 287-293, 1997.
- [11] C. W. G. B4.61, "General Guidelines for HVDC Electrode Design," Jan. 2017.
- [12] B. B. a. M. S. J.C. Gleadow, "DC Ground Currents and Transformer Saturation on the New Zealand HVDC Link," in *CIGRÉ International Colloquium on High Voltage Direct Current and Flexible AC Power Transmission Systems*, Wellington, New Zealand, Sept. 1993.
- [13] "IEEE Guide for Establishing Power Transformer Capability while under Geomagnetic Disturbances," IEEE C57.163, 2015.
- [14] S. A. Mousavi, "Electromagnetic modelling of power transformers with DC magnetization," Ph.D. dissertation, Dept. Elect. Eng., KTH Royal Institute of Technology, Stockholm, 2012.
- [15] B. Bozoki and et al, "The Effects of GIC on Protective Relaying," *IEEE Transactions on Power Delivery*, vol. 11, no. 2, pp. 725-739, 1996.
- [16] "March 13, 1989 Geomagnetic Disturbance," North American Electric Reliability Council (NERC), 1989.
- [17] S. Zurek, *Characterisation of Soft Magnetic Materials Under Rotational Magnetisation*, London: CRC Press, 2018.
- [18] J. Wang, H. Lin, Y. Huang and X. Sun, "A New Formulation of Anisotropic Equivalent Conductivity in Laminations," *IEEE Transactions on Magnetics*, vol. 47, pp. 1378 -1381, 2011.
- [19] H. Ding and et al, "Analysis of Coupling Effects on Overhead VSC-HVDC Transmission Lines From AC Lines With Shared Right of Way," in *IEEE Power and Energy Society General Meeting*, MI, USA, 2011.

- [20] K. Sharifabadi, L. Harnefors, H. P. Nee, S. Norrga and R. Teodorescu, Design, Control, and Application of Modular Multilevel Converters for HVDC Transmission Systems, Wiley-IEEE Press,, 2016.
- [21] S. V. Kulkarni and S. A. Khaparde, Transformer Engineering: Design and Practice, New York,: Marcel Dekker, Inc.,, 2004.
- [22] D. C. Jiles and D. L. Atherton, "Theory of ferromagnetic hysteresis," *Journal of Applied Physics*, vol. 55, no. 6, pp. 2115- 2120, 1984.
- [23] F. Preisach, "Über die magnetische Nachwirkung," *Zeitschrift für Physik*, vol. 94, p. 277–302, 1935.
- [24] A. J. Bergqvist, "A simple vector generalization of the Jiles-Atherton model of hysteresis," *IEEE Transactions on Magnetics*, vol. 32, no. 5, pp. 4213-4215, 1996.
- [25] I. D. Mayergoyz, Mathematical Models of Hysteresis, New York: Academic Press, 1990.
- [26] N. Sadowski, N. Batistela, J. Bastos and M. L. Mazenc, "An inverse Jiles-Atherton model to take into account hysteresis in time-stepping finite-element calculations," *IEEE Transactions on Magnetics*, vol. 37, no. 2, pp. 797-800, 2002.
- [27] M. Mathekga, R. McMahon and A. Knight, "Application of the Fixed Point Method for Solution in Time Stepping Finite Element Analysis Using the Inverse Vector Jiles-Atherton Model," *IEEE Transaction on Magnetics*, vol. 47, no. 10, pp. 3048-3051, 2011.
- [28] S. Liu, S. Huang and H. Chen, "Using TACS Functions Within EMTP to Set Up Current-Transformer Model Based on the Jiles–Atherton Theory of Ferromagnetic Hysteresis," *IEEE Transactions on Power Delivery*, vol. 22, no. 4, pp. 2222-2227, 2007.
- [29] K. Overshott, "The use of domain observations in understanding and improving the magnetic properties of transformer steels," *IEEE Trans. Mag.*, pp. 840-845, 1976.
- [30] T. T. H. Suzuki, "Recent development of grain-oriented electrical steel in JFE Steel," JFE Technical Report, 2016.

Bibliography

- [31] H. Hedia, J. F. Remacle, P. Dular and et al, "A sinusoidal magnetic field computation in nonlinear materials," *IEEE Transaction on Magnetics*, vol. 31, no. 6, pp. 3527-3529, 1995.
- [32] D. Labridis and P. Dokopoulos, "Finite element computation of eddy current losses in nonlinear ferromagnetic sheaths of three-phase power cables," *IEEE Transaction on Power Delivery*, vol. 7, no. 3, pp. 1060-1067, 1992.
- [33] N. Demerdash and D. Gillott, "A new approach for determination of eddy current and flux penetration in nonlinear ferromagnetic materials," *IEEE Transaction on Magnetics*, vol. 10, no. 3, pp. 682-685, 1974.
- [34] Y. D. Terrail, J. Sabonnadiere, P. Masse and J. Coulomb, "Nonlinear complex finite elements analysis of electromagnetic field in steady-state AC devices," *IEEE Transaction on Magnetics*, vol. 20, no. 4, pp. 549-552, 1984.
- [35] G. Paoli, O. Biro and G. Buchgraber, "Complex representation in nonlinear time harmonic eddy current problems," *IEEE Transaction on Magnetics*, vol. 34, no. 5, pp. 2625-2628, 1998.
- [36] S. Yamada, and K. Bessho, "Harmonic field calculation by the combination of finite element analysis and harmonic balance method," *IEEE Transaction on Magnetics*, vol. 24, no. 6, pp. 2588-2590, 1988.
- [37] E. Barbisio, F. Fiorillo and C. Ragusa, "Predicting loss in magnetic steels under arbitrary induction waveform and with minor hysteresis loop," *IEEE Transaction on Magnetics*, vol. 40, no. 4, pp. 1810-1819, 2004.
- [38] L. Jieli, T. Abdallah, and C. R. Sullivan, "Improved Calculation of Core Loss With Nonsinusoidal Waveforms," in *IEEE Industry Applications Society Annual Meeting*, 2001.
- [39] S. Yue and et al, "Comparative analysis of core loss calculation methods for magnetic materials under nonsinusoidal excitations," *IEEE Transaction on Magnetics*, vol. 54, 2018.

- [40] C. A. Hernandez-Aramburo, T. C. Green and A. C. Smith, "Estimating rotational iron losses in an induction machine," *IEEE Transactions on Magnetics*, vol. 39, no. 6, pp. 3527-3533, 2003.
- [41] H. Pftzner, E. Mulasalihovic, H. Yamaguchi, D. Sabic, G. Shilyashki and F. Hofbauer, "Rotational Magnetization in Transformer Cores—A Review," *IEEE Transactions on Magnetics*, vol. 47, no. 11, pp. 4523-4533, 2011.
- [42] A. J. Moses , "Importance of rotational losses in rotating machines and transformers," *Journal of Materials Engineering and Performance volume*, vol. 1, p. 235–244, 1992.
- [43] H. Pftzner, "Rotational magnetization and rotational losses of grain oriented silicon steel sheets-fundamental aspects and theory," *IEEE Transactions on Magnetics*, vol. 30, no. 5, pp. 2802-2807, 1994.
- [44] N. Stranges and R. D. Findlay, "Measurement of rotational iron losses in electrical sheet," *IEEE Transactions on Magnetics*, vol. 36, no. 5, pp. 3457-3459, 2000.
- [45] J. Turowski and A. Pelikant, "Eddy current losses and hot-spot evaluation in cover plates of power transformers," *IEE Proceedings - Electric Power Applications*, vol. 144, no. 6, p. 435 – 440, 1997.
- [46] J. Turowski and M. Turowski, *Engineering Electrodynamics: Electric Machine, Transformer, and Power Equipment Design*, CRC Press, 2014.
- [47] J. A. Elbert, "Power transformer operation at over and under excitation benefits and consequences," *IEEE Trans. on Power Delivery*, vol. 15, no. 1, pp. 192-196, 2000.
- [48] G. B. G. L. a. K. P. O. Biro, "Prediction of Magnetizing Current Wave-Forms in a Three-Phase Power Transformer Under DC Bias," *IEEE Transactions on Magnetics*, vol. 44, no. 6, pp. 1554-1557, 2008.
- [49] I. Booth and H. Pftzner, "Characteristics of transformer core material for flux normal to the sheet plane," *Journal of Magnetism and Magnetic Material*, vol. 133, pp. 183-186, 1994.

Bibliography

- [50] "European Risk from Geomagnetically Induced Currents," <http://www.eurisgic.eu/>, 2014.
- [51] IEC 60404-2:1996 Magnetic materials - Part 2: Methods of measurement of the magnetic properties of electrical steel sheet and strip by means of an Epstein frame, 1996.
- [52] IEC 60404-3:1992 Magnetic materials - Part 3: Methods of measurement of the magnetic properties of magnetic sheet and strip by means of a single sheet tester, 1992.
- [53] IEC 60404-6:2018 Magnetic materials - Part 6: Methods of measurement of the magnetic properties of magnetically soft metallic and powder materials at frequencies in the range 20 Hz to 100 kHz by the use of ring specimens, 2018.
- [54] T. Ngnegueu and et al, "Behaviour of transformers under DC/GIC excitation: Phenomenon, Impact on design/design evaluation process and Modelling aspects in support of Design," in *CIGRE Session A2-303*, Paris, 2012.
- [55] N. Alatawneh and a. et, "Accuracy of time domain extension formulae of core losses in non-oriented electrical steel laminations under non-sinusoidal excitation," *IET Electric Power Applications* , vol. 11, no. 6, pp. 1131-1139, 2017.
- [56] E. Agheb and H. K. Hoidalén, "Modification of empirical core loss calculation methods including flux distribution," *IET Electric Power Applications*, vol. 7, pp. 381-390, 2013.
- [57] J. Reinert, A. Brockmeyer and R. W. Doncker, "Calculation of losses in ferro- and ferrimagnetic materials based on the modified Steinmetz equation," in *34th Annual Meeting of the IEEE Industry Applications Society*, 1999.
- [58] T. Kochmann, "Relationship between rotational and alternating losses in electrical steel sheets," *Journal of Magnetism and Magnetic Materials*, vol. 160, pp. 145-146, 1996.

Publications

Paper I

Wei Wang, Arne Nysveen, Niklas Magnusson, Robert Nilssen, “Fourier-based effective permeability for transformer iron losses computation under saturation,” IET Transaction on Electrical Power Applications, December 2020, Volume 14, Issue 13, p.2609–2615, <https://doi.org/10.1049/iet-epa.2020.0315>.

This paper is not included due to copyright restrictions.

Paper II

W. Wang, A. Nysveen, N. Magnusson and R. Nilssen, "Computation of transformer iron losses under saturation using the Fourier method Part 2: Stray loss," *22nd International Conference on the Computation of Electromagnetic Fields (COMPUMAG)*, Paris, France, 2019, pp. 1-4, doi:10.1109/COMPUMAG45669.2019.9032726.

Computation of transformer iron losses under saturation using the Fourier method Part 2: Stray loss

Wei Wang¹, Arne Nysveen¹, *Senior Member, IEEE*, Niklas Magnusson² and Robert Nilssen¹

¹Electric Power Department, Norwegian University of Science and Technology, Trondheim, NO-7491 Norway

²SINTEF Energy Research, NO-7465 Trondheim, Norway

Computation of iron losses is a heavy numerical task, and the problem is further complicated by magnetic nonlinearity when saturation is considered. In an accompanying paper, a Fourier method for calculation of the transformer core loss under saturation is presented. In this paper, the influence of the permeability definition of the core material on leakage field and the associated stray loss calculation is studied. Based on the relationship between magnetic field and input current, a waveform correction factor is introduced which enables stray loss estimation of nonsinusoidal excitations. The results obtained by this method are compared to those given by a time domain calculation to evaluate the accuracy of the method.

Index Terms— Finite element analysis, Fourier transforms, Magnetic losses, Power transformers, Saturation magnetization.

I. INTRODUCTION

IRON STRAY LOSS occurs in ferromagnetic structural parts of power transformers. In many cases, a time-harmonic method with surface impedance boundary conditions (SIBCs) is efficient and accurate enough to calculate the magnetic field and the associated loss. However, at magnetic saturation, due to e.g. ferromagnetic resonance and geomagnetically induced currents (GIC), the problem is complicated by magnetic nonlinearity.

Various effective permeability definitions have been proposed for time-harmonic problems involving ferromagnetic materials [1]-[3]. In the validation of those methods, focus has been on the overall equivalent field and the associated power loss of the core material itself. Little attention has been paid to the influence of those definitions on the stray field.

A definition of the effective magnetic permeability based on the Fourier series of the magnetization curve is presented in an accompanying paper [4]. The definition has been proved to be time efficient and sufficiently accurate for calculating transformer core loss under saturation. In the present paper we study how the definition influences the stray field and thereby the stray loss. We compare the stray loss calculated using the Fourier method with the stray loss calculated using definitions available in the literature, as well as with the loss determined more accurately by a (time-consuming) time domain calculation.

The surface impedance (SI) method and its various extended formulations [5]-[6] enable a straightforward analysis of electromagnetic fields and eddy loss on the iron surfaces with sinusoidal excitation under linear or saturated conditions. However, when the magnetic core (instead of the iron wall) is under saturation, the nonsinusoidal excitation problem cannot be simply treated by a linear superposition of the harmonics of the excitation (source), even though the iron wall is in a linear region. To deal with the such condition, we propose a waveform correction factor in combination with SI to calculate the stray losses.

II. EFFECTIVE PERMEABILITY AND WAVEFORM CORRECTION FACTOR

A. Effective Permeability

Several approaches exist to determine the effective permeability based on the magnetization curve of the ferromagnetic materials. In the average energy method [1], the effective permeability is defined as:

$$\mu_{\text{eff},AE} = \frac{16}{TH_m^2} \int_0^{T/4} \left[\int_{H(0)}^{H(t)} B(H) dH \right] dt \quad (1)$$

where $B(H)$ is the nonlinear magnetization virgin curve of the material, H_m is the amplitude of the time-harmonic magnetic field and T is the period of the oscillation.

In the simple energy method [2], the effective permeability is defined by means of the magnetic coenergy:

$$\mu_{\text{eff},SE} = \frac{2}{H_m^2} \int_0^{H_m} B(H) dH \quad (2)$$

In the Root Mean Square (RMS) method [3], the effective permeability is defined as:

$$\mu_{\text{eff},RMS} = \frac{\sqrt{2}}{H_m} \sqrt{\frac{1}{T} \int_0^T B^2(t) dt} \quad (3)$$

where $B(t)$ is obtained from the magnetization curve.

The Fourier method presented in the accompanying paper is based on the Fourier series of the magnetization curve [4]. The effective permeability is defined as:

$$\mu_{\text{eff},k} = \frac{\mathcal{F}_k \{ B(H_m \sin(\omega t)) \}}{H_m} \quad (4)$$

where \mathcal{F}_k is the Fourier operator giving the k th Fourier series coefficient. The fundamental component μ_1 is implemented as the magnetization definition in the finite element analysis.

With domain decomposition, a modified form, taking spatial variations in the magnetic field to current excitation relationship into account, has shown an improved accuracy in the core loss calculation [4].

$$\mu_{mf-eff,k} = \frac{\mathcal{F}_k \{B(H(I_m \sin(\omega t)))\}}{\mathcal{F}_k \{H(I_m \sin(\omega t))\}} \quad (5)$$

For nonsinusoidal excitation, the generalized form of the Fourier type effective permeability [4] can be used:

$$\mu_{gf-eff,k} = \frac{\mathcal{F}_k \{B(H(I(t)))\}}{\mathcal{F}_k \{H(I(t))\}} \quad (6)$$

Using a typical silicon steel material [4], different effective magnetization curves obtained by the abovementioned methods are illustrated in Fig. 1. In the linear region, the magnetization curves of the methods behave almost the same as the virgin curve. However, in the nonlinear region, the differences between various approaches become remarkable.

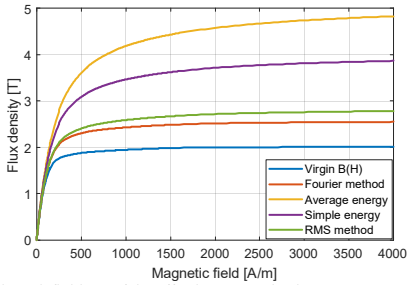


Fig. 1. Various definitions of the effective magnetization curves.

Although the effective permeability is mainly proposed for emulating the performance of the nonlinear material (the core) itself, we will demonstrate that an appropriate definition of the core is also critical for leakage field calculation and associated stray loss evaluation.

B. Waveform Correction Factor due to Nonsinusoidal Excitation Currents

The eddy loss in a steel plate subjected to a magnetic field can be calculated with the surface impedance method:

$$P = \iint_s \mathcal{R}\{Z_s\} \frac{H_m^2}{2} ds \quad (7)$$

where H_m is the amplitude of the surface tangential magnetic field and the surface impedance is expressed as:

$$Z_s = \sqrt{\frac{\omega\mu}{2\sigma}}(1 + j) \quad (8)$$

where μ is the permeability of the ferromagnetic material, σ is the electric conductivity and ω is the angular frequency.

A conductor surface is represented by $z=0$. Let $z>0$ and $z<0$ represent the regions corresponding to the conductor and perfect loss-free dielectric medium (Fig. 2). Assume that the vector field E has a component only along the x -axis and that E_x is a function of z only. In the frequency domain, E_x can be expressed in the complex exponential notation.

$$E_x(z) = E_{x0} e^{-\frac{z}{\delta}} \quad (9)$$

where E_{x0} is the electric field intensity at the surface and δ is the skin depth.

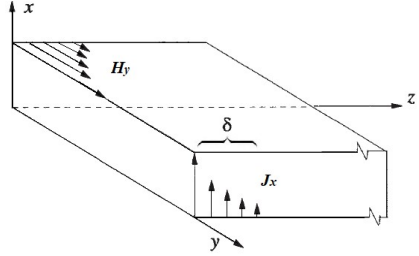


Fig.2. Penetration of field and induced current inside a conductor.

Faraday's law with E in the x -direction varying as a function of z only becomes:

$$\frac{\partial E_x}{\partial z} = -\frac{\partial B_y}{\partial t} \quad (10)$$

Substituting the value of E_x from (9) and rearranging (10) with time-harmonic representation, we obtain:

$$E_{x0} = \frac{j\omega}{\delta} B_{y0} \quad (11)$$

According to Ohm's law, the current density J within a conductor is proportional to the electrical field intensity, thus

$$J_x = \sigma E_{x0} e^{-\frac{z}{\delta}} = \frac{\sigma}{\delta} j\omega B_{y0} e^{-\frac{z}{\delta}} \quad (12)$$

Therefore, the current density is proportional to the product of the tangential flux density on the iron surface and the frequency. For nonsinusoidal waveform, our assumption is to extend this expression by replacing $j\omega B$ with the root mean square (RMS) average of the time derivative of B over a period, i.e.

$$j\omega B \rightarrow \sqrt{\int_0^T \left(\frac{\partial B}{\partial t}\right)^2 dt} \quad (13)$$

On basis of (13), a wave correction factor k_{curr} for the nonsinusoidal current density can be introduced

$$k_{curr} = \frac{J_{rms}}{J_1} = \frac{\sqrt{\int_0^T [\partial B(H(I(t)) / \partial t)]^2 dt}}{\sqrt{\int_0^T [\partial B(H(I_1 \sin(\omega t)) / \partial t)]^2 dt}} \quad (14)$$

The current $I(t)$ in the numerator is the nonsinusoidal current and the current in the denominator $I_1 \sin(\omega t)$ is the reference fundamental (sinusoidal) current. $B(H)$ is the magnetization function of the iron tank material. Thus, the equivalent current can be simply defined as

$$I_{eq} = k_{curr} I_1 \quad (15)$$

Furthermore, a wave correction factor k_e for the stray loss can be defined, which is the ratio between the power loss P_{ns} under nonsinusoidal excitation and the power loss P_1 under sinusoidal excitation.

$$P_{ns} = k_{loss} P_1 \quad (16)$$

P_1 is calculated by the conventional time-harmonic approach with the SIBC. In light of (7), k_{loss} can be expressed by

$$k_{loss} = \frac{P_{ns}}{P_1} = \left[\frac{H_m(I_{eq})}{H_m(I_1)} \right]^2 = \left[\frac{H_m(k_{curr} I_1)}{H_m(I_1)} \right]^2 \quad (17)$$

In the linear region of the transformer core, the incident magnetic field on the tank wall is proportional to the input

current. Therefore, k_{loss} reduces to k_{curr}^2 . In the nonlinear region, however, the incident field is no longer proportional to the input current due to core saturation. Thus, a more general dependency is used, where the magnetic field is assumed to be proportional to γ^{th} power of the current. Finally, k_{loss} is simplified to

$$k_{loss} = k_{curr}^{2\gamma} \quad (18)$$

where γ equals one in a linear region as mentioned. The $H(I)$ function used in (14) as well as the coefficient γ can be obtained by a frequency domain scan.

III. SIMULATIONS

A. Model Setup

To evaluate how the permeability definitions in section IIA for the core material influence stray loss calculation results, they were implemented in the frequency domain finite element model of the transformer described in [4]. The results are compared with the results obtained with an accurate (but largely time-consuming) time domain method.

The simulations were performed at 50 Hz on a single-phase transformer. The virgin magnetization data of the silicon steel of the transformer core and the corresponding B - H curve are illustrated in [4]. The magnetization data [7] of the carbon steel of the transformer tank and the corresponding B - H curve with cubic spline interpolation are shown in Fig. 3 (right).

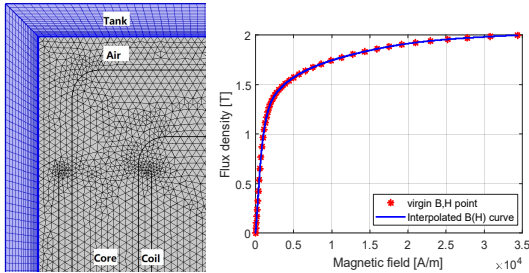


Fig. 3. The transformer quarter model (left) with fine mesh and the virgin magnetization curve of the carbon steel used for the transformer tank (right).

The surface boundary condition and the effective B - H curves were used for all the frequency domain simulations. In the time domain model, the virgin magnetization curves were used. The iron surface of the tank wall was meshed with a large number of elements to account for the thin skin depth.

B. Stray Loss under Sinusoidal Excitation

The definitions in section IIA were implemented with sinusoidal excitation currents varying from 10 A to 2000 A, going from the linear region to the heavy saturated region for the magnetic materials. The same setup was applied to the corresponding time domain model. The loss on the tank surface was calculated and compared with its counterparts calculated from the frequency domain simulations, see Fig. 4.

In the linear region (<10 A) and slightly nonlinear region (<100 A), where the excitation current is moderate, the different definitions of the effective permeability yield results practically equal to those calculated with the time domain method, and

hence, are good estimations of the stray loss. However, in the heavy saturated region (>100 A), the average energy (1) and simply energy (2) methods largely overestimate and the RMS method (3) slightly overestimates the stray loss. In contrast, the Fourier method gives a better estimation of the stray loss over the whole range. This is due to that the formulation of the Fourier method is the closest to the original flux density waveform in the least-square sense.

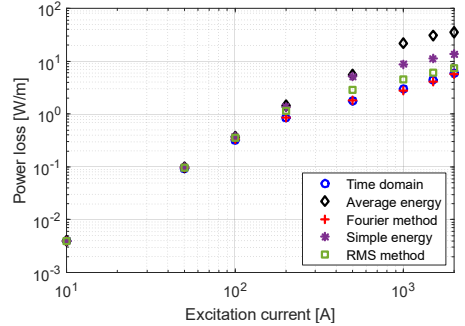


Fig. 4. Stray loss on the transformer tank wall calculated by various effective permeability methods under different saturation levels.

C. Stray Loss under Nonsinusoidal Excitation

To validate the waveform factor derived for stray loss calculation under nonsinusoidal excitation, three test cases under heavy saturation were set up. The sinusoidal excitation of power frequency (Case 1) is the reference case, whereas the two other cases have the same fundamental component, but the third harmonics of opposite phase angles are added.

- Case 1: $I_1 = 1\sin(100\pi t)$ [kA]
- Case 2: $I_2 = 1\sin(100\pi t) + 0.15\sin(300\pi t)$ [kA]
- Case 3: $I_3 = 1\sin(100\pi t) - 0.15\sin(300\pi t)$ [kA]

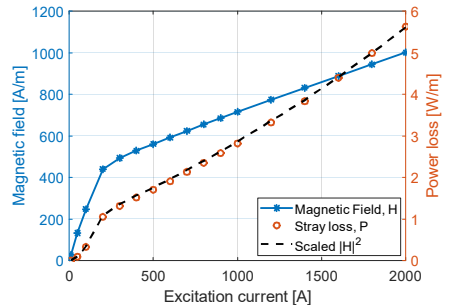


Fig. 5. Average tangential magnetic field (blue line) and the average power loss (dotted line: P , simulated value; dashed line: scaled $|H|^2$, derived from the blue line) on the tank wall as function of excitation current obtained from frequency domain scan.

A frequency domain field versus current scan was performed to specify $H(I)$. In Fig. 5, the stray loss P matches the scaled $|H|^2$ curve, which confirms the assumption (17). In the linear and slightly nonlinear region ($I_m < 0.1$ kA), the power loss is proportional to the square of the input current, i.e. $k_e = k_r^2$ (or $\gamma = 1$). For the heavy saturation test case ($I_m = 1$ kA), the stray loss

has an approximately linear dependency on the excitation current, which practically gives $k_e = k_i$ (or $\gamma=0.5$).

The results obtained by the time domain simulations are illustrated in Fig. 6. The induced current density waveform is more sinusoidal at the moderate saturation level (0.1 kA) than at the high saturation level (1 kA). Sharp spikes can be observed under heavy saturation (cases 1-3), especially in proximity to the iron surface. The peak value is also sensitive to the shape of the input current, i.e. given the same fundamental excitation current, the peak of the induced current density is strongly influenced by the phases of the harmonics.

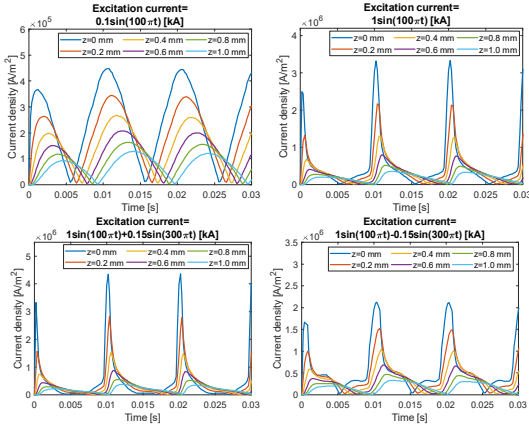


Fig. 6. Induced current density variation in time at different depth in the tank wall under different excitation currents. Upper left: excitation current=0.1 kA; Upper right: Case 1; Lower left: Case 2; Lower right: Case 3.

Those shape effects are related to the time derivative of the flux density and have been taken into account in the definition (14). Fig. 7 shows the average flux density $B(t)$ on the tank wall surface in a half period and its time derivative, directly derived from the obtained $H(I)$ function (Fig. 5) without involving a time domain simulation.

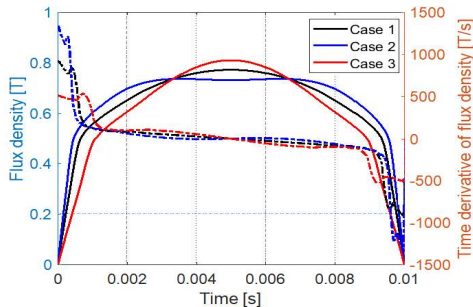


Fig. 7. Flux density on the tank wall (solid lines) and its time derivative (dashed lines) as function of time for the cases in Table I.

The stray loss of the sinusoidal case (Case 1 in Table I) is calculated using classical surface impedance method. The stray losses of the nonsinusoidal cases (Case 2 and 3) are calculated by the stray loss of the reference case (Case 1) multiplying with the correction factor k_{loss} . Apparently, the waveform of the

excitation current has a significant impact on the stray losses. The result from the frequency domain calculation with the proposed method shows a good agreement with the corresponding time domain simulation. The result also indicates that a conventional practice such as the total harmonic distortion (THD) approach, which is applicable in a linear region, could potentially lead to a large overestimation of the stray loss under saturation.

TABLE I
STRAY LOSS ON THE IRON SURFACE

Test case	Stray loss correction factor, k_{loss}		Stray loss density, P [W/m]	
	Time domain	Frequency domain	Time domain	Frequency domain
Case 1	1	1	3.00	2.81
Case 2	1.193	1.191	3.58	3.35
Case 3	0.817	0.799	2.45	2.25

The stray loss correction factor in frequency domain is calculated from (14) and (18). The stray loss correction factor in time domain is directly calculated from obtained simulation results.

IV. CONCLUSIONS

The accuracy of calculated stray loss under heavy saturation is largely influenced by the chosen definition of the effective permeability of the magnetic core. The described Fourier method yields significantly higher accuracy than energy based methods. Furthermore, the waveform of input current excitation has considerable impact on the stray loss, particularly under magnetic saturation of the core. The proposed waveform correction factor in combination with the conventional surface impedance method enables time efficient evaluation of the stray loss for nonsinusoidal current excitation under saturation.

ACKNOWLEDGMENT

This work was performed as a part of the project "Thermal Modelling of Transformers" (project number: 255178) funded by the Research Council of Norway, Statnett, Hafslund and Lyse Nett.

REFERENCES

- [1] D. Labridis and P. Dokopoulos, "Finite element computation of eddy current losses in nonlinear ferromagnetic sheaths of three-phase power cables," *IEEE Trans. on Power Delivery*, vol. 7, pp. 1060-1067, 1992.
- [2] H. Hedia, J. F. Remacle, P. Dular, A. Nicolet, A. Genon and W. Legros, "A sinusoidal magnetic field computation in nonlinear materials," *IEEE Trans. Magn.*, vol. 31, no. 6, pp. 3527-3529, 1995.
- [3] Y. Du Terrail, J. C. Sabonnadiere, P. Masse and J. L. Coulomb, "Nonlinear complex finite elements analysis of electromagnetic field in steady-state AC devices," *IEEE Trans. Magn.*, pp. 549-552, July 1984.
- [4] W. Wang, A. Nysveen, N. Magnusson and R. Nilssen, "Computation of transformer iron losses under saturation using the Fourier method Part 1: Spectra for core loss calculation," *International Conference on the Computation of Electromagnetic Fields*, Paris, July 2019.
- [5] S. Yuferev and L. Di Rienzo, "Surface impedance boundary conditions in terms of various formalisms," *IEEE Trans. Magn.*, vol. 46, no. 9, pp. 3617-3628, Sep. 2010.
- [6] J. Gyselinck, P. Dular, C. Geuzaine, and R. V. Sabariego, "Surface impedance boundary conditions in time-domain finite-element calculations using the magnetic-vector-potential formulation," *IEEE Trans. Magn.*, vol. 45, no. 3, pp. 1280-1283, Mar. 2009.
- [7] COMSOL Multiphysics® v. 5.4. www.comsol.com. COMSOL AB, Stockholm, Sweden.

Paper III

W. Wang, A. Nysveen and N. Magnusson, “Apparatus for loss measurements under multidirectional and dc-bias flux in electrical steel laminations,” *Rev. Sci. Instrument.* Vol.91, Issue 8, 2020, DOI: 10.1063/5.0011076.

Apparatus for loss measurements under multidirectional and dc-bias flux in electrical steel laminations

Cite as: Rev. Sci. Instrum. 91, 084705 (2020); doi: 10.1063/5.0011076

Submitted: 17 April 2020 • Accepted: 9 August 2020 •

Published Online: 21 August 2020



W. Wang,^{1,a)} A. Nysveen,¹ and N. Magnusson²

AFFILIATIONS

¹Department of Electric Power Engineering, Norwegian University of Science and Technology, NO-7491 Trondheim, Norway

²SINTEF Energy Research, NO-7465 Trondheim, Norway

^{a)}Author to whom correspondence should be addressed: weiwan@ntnu.no

ABSTRACT

Conventional standardized power loss measurements for electric steels are performed at flux densities with a single sinusoidal and unidirectional excitation. However, the flux inside electrical steel laminations can deviate significantly from the standard condition, and the loss is sensitive to such deviations of the flux in time and space. In this article, we describe the design and construction of an apparatus for loss measurements under two scenarios: (1) The main flux in the rolling direction is superimposed with flux in either the transverse or normal direction, while varying magnitude and phase angle between two fluxes and (2) the main flux having a dc-bias. The main flux in the rolling direction is generated in a square lamination frame by the current in excitation coils. The transverse and normal direction fluxes are generated by the current in auxiliary excitation coils wound around powder cores. The dc-bias flux is created either by an ac current with a small dc offset in the excitation coils or by a separate coil excited by a dc current. We implement and compare the two dc-bias methods and discuss the commons and differences. Finally, we present experimental results showing the possibilities for loss measurements under the combined action of magnetic flux in different directions and under dc-bias.

Published under license by AIP Publishing. <https://doi.org/10.1063/5.0011076>

I. INTRODUCTION

Variable power production and load, due to, e.g., wind and solar energy and charging of electrical vehicles, lead to new load patterns for power equipment, where the acceptance of short-time overloads can reduce the need for new investments. In addition, the effect of geomagnetically induced currents (GICs) is a concern for network owners. These considerations lead to an increased importance of the loss in power equipment operating outside its design specifications. In transformers and rotational machines, the laminated iron cores are, in addition to the main flux following the direction of the core, exposed to the magnetic leakage flux, which can be significant at high loads. In power transformers, the leakage flux enters the laminated core from different directions [see the flux lines entering the core in Fig. 1(a) and the definition of flux directions in Fig. 1(b)], leading to additional power loss in the laminations close to the windings. Depending on the orientation of the leakage

flux relative to the lamination, different loss mechanisms dominate the additional loss.

- Flux configuration 1: On the limb surface of the magnetic core, the leakage flux normal to the plane (ND) of the lamination induces eddy currents and thereby generates eddy current loss.¹⁻³
- Flux configuration 2: Under the yoke of the core, the leakage flux enters the core perpendicular to the rolling direction (RD) in the plane of the lamination [transverse direction (TD)]. Due to the thin laminations, the eddy currents induced by the flux become small, and the power loss is dominated by hysteresis loss. In many cases, the transverse leakage flux and the main flux are not in phase. The total magnetic field, then, becomes rotating, and the power loss is associated with rotational hysteresis loss.⁴⁻⁷

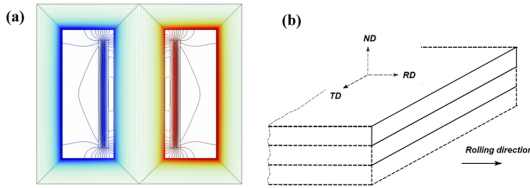


FIG. 1. (a) Flux distribution of a single-phase transformer obtained by a numerical simulation. The transformer shown is operating under resistive load. The flux distribution is presented at the time instant when the leakage flux density is at its maximum (i.e., the load current is at its peak, and the main flux is at its zero crossing). (b) Definition of the flux directions in the grain-oriented steel laminations. RD: rolling direction; ND: normal direction; and TD: transverse direction.

The strong anisotropy of the lamination structure⁸ and the magnetic anisotropy of grain-oriented (GO) steel prevent the incident flux to cross many of the lamination layers or reach far into the core in the transverse direction. Instead, the penetrated flux tends to close its loop on the surface layers of the lamination or along the edge of the lamination plane [see the flux line concentration and flux density distribution inside the core in Fig. 1(a)]. Consequently, the surface layers and edges of the lamination are prone to be saturated, even when the incident leakage flux density is well below the saturation flux density of the steel, resulting in that the leakage flux becomes important also at relatively small amplitudes. Furthermore, the phase angle between the main flux and the leakage flux may play an important role for the loss since eddy current loss and hysteresis loss are sensitive to both magnitude and the variation in time of the magnetic flux density.

The power loss in lamination cores is also sensitive to the dc-bias of the main flux.^{9–11} Geomagnetic disturbances^{12–14} can lead to GIC events where a dc current generates a dc-bias of the main field (and the same may occur due to power converter cross-modulation^{15,16}). Dc magnetization leads to half-cycle saturation of the core in power transformers. This may result in harmonic pollution, reactive power consumption,¹⁴ and transformer over-heating.¹⁷

Various power loss measurement apparatuses for magnetic materials have been proposed, which can be categorized into wattmetric,^{18,19} mechanical type²⁰ (torque magnetometers), thermometric,^{21,22} and fieldmetric.^{23,24} The Epstein frame¹⁸ and the Single Sheet Tester (SST)¹⁹ methods are the two standardized methods for measurements of the magnetic properties of electrical steel sheets, both based on the wattmeter method. The Epstein frame consists of four coils into which strips to be tested are inserted and assembled in a square. The losses are calculated from the current of the primary winding and the voltage of the secondary winding. In the single sheet tester, the sheet specimen is placed inside two windings (in addition, here, the primary winding yields the current and the secondary winding the voltage for the loss calculation) between a double-C laminated yoke.¹⁹ Despite the simplicity and applicability of the SST method, the Epstein method is at present still regarded as the sole reference method for the determination of the material quality.²⁵ The fieldmetric methods, while not yet standardized, are becoming widely used in rotational loss measurements, where

two-dimensional SST with various yoke configurations has been developed.^{23,26,27} However, due to the limited area of uniform magnetization (comparable with the grain size of the material), the measurement does not allow for averaging of the properties over a large volume.⁴

In both the standardized methods (Epstein frame and SST), the power loss is determined for flux densities with a single sinusoidal and unidirectional excitation. To meet the increasing importance of studying the loss in electrical sheets with the combined action of main flux and either the leakage flux (including different phase shifts) or dc-bias flux, we have developed a measurement system based on the wattmeter method and the basic Epstein frame geometry. The system is designed to characterize the power loss due to ac magnetic flux densities in RD combined either with dc-bias flux densities in the same direction or with flux densities in the TD direction. Additionally, the system allows for a replica of the actual leakage configurations in the laminated core for qualitative studies of the associated losses.

This paper is organized as follows. The loss components are introduced in Sec. II. The measurement principle is described in Sec. III, along with the equivalent circuit element models. The apparatus design is presented in Sec. IV, with the details on construction of the lamination sample frame and the excitation systems. In Sec. V, the experimental results demonstrating the capability of the system are presented. Finally, a summary of the results is given together with the conclusions in Sec. VI.

II. LOSS COMPONENTS IN ELECTRICAL STEELS

Magnetic loss can be conceptually separated into eddy current loss, hysteresis loss, and excess loss.²⁸ Eddy current loss and hysteresis losses arise due to successive reversal of magnetization in the iron core. The difference between the measured and calculated losses (eddy current and hysteresis loss) has been referred to as the anomalous loss (or excess loss).²⁹ Regardless of this discrepancy, the two-component approach (eddy current and hysteresis loss) is still widely used, owing to its simplicity.⁴

Eddy current loss (P_e) has its origin in induced voltages in the laminations in response to a sinusoidal magnetic flux in the lamination plane. Since the thickness of the sheet is much smaller than the skin depth power frequency, the eddy current loss can be expressed as²⁹

$$P_e = k_e f^2 t^2 B_{peak}^2, \quad (1)$$

where k_e is a material dependent constant, f (Hz) is the frequency of the magnetization, t (m) is the thickness of individual sheets, and B_{peak} (T) is the flux density. However, the relationship (1) can be largely violated when the flux is not oriented along the lamination plane. This is the case, for instance, when the leakage flux is normal to the lamination plane.¹

Hysteresis loss is caused by the irreversible domain wall movement and magnetization rotation within the domains in the magnetic material in response to a variable magnetic flux. Hysteresis loss is proportional to the enclosed area of the B - H curve (the hysteresis loop) under quasi-static alternating magnetization,²⁹

$$P_h = k_h f B_{peak}^n, \quad (2)$$

where k_h is a material dependent constant, B_{peak} (T) is the flux density, and n is the Steinmetz constant having a value between 1.6 and 2.0 for hot rolled laminations and a value of more than 2.0 for cold rolled laminations.²⁹ However, when the flux has a dc-bias, the hysteresis loop becomes asymmetric. Depending on the level of the dc excitation, the loss feature can deviate significantly from the symmetric ac excitation,¹⁴ and hence, the power loss, then, depends on both the applied ac and dc fluxes.

When the material is subjected to a magnetic flux with its direction rotating in the plane of the lamination, the loss will be enhanced. As a comparison, the average power loss per unit mass for an alternating magnetization,⁵ P_a , and rotational magnetization,³⁰ P_r , is given by

$$P_a = \frac{1}{\rho T} \int_0^T \left(\frac{dB_x}{dt} \cdot H_x \right) dt, \quad (3a)$$

$$P_r = \frac{1}{\rho T} \int_0^T \left(\frac{dB_x}{dt} \cdot H_x + \frac{dB_y}{dt} \cdot H_y \right) dt, \quad (3b)$$

where ρ (kg/m³) is the mass density of the material, T (s) is the period of magnetization, and $B_{x(y)}$ (T) and $H_{x(y)}$ (A/m) are the flux density and magnetic field strength in the x(y) direction.

III. MEASUREMENT PRINCIPLE

The instrument serves two main purposes: (1) material power loss characterization under multidirectional flux or dc-bias conditions and (2) loss measurements with a replica of actual leakage flux configurations. The former requires a homogeneous field in a specified region and the measurement of power loss in such a region (isolating the contribution outside of the region) such that the specific loss can be obtained. In a unidirectional flux measurement such as an ac RD flux test or dc-bias test, this is straightforward since the flux is uniformly distributed in the whole sample, and the loss contributed by the measurement device is negligible. The measurement principles of these types of tests are illustrated in Secs. III A and III C. When the multidirectional flux is considered, the flux-homogenous region shall be identified, and the loss contribution outside the region as well as the contribution from the auxiliary devices shall be excluded. Such a test is described in Sec. III B (RD flux superimposed with TD flux). The actual leakage flux configuration is far from homogeneous as

described in Sec. I. In a replica of such flux configurations, the inhomogeneous field should emulate real configurations. The measured loss variations give qualitative information of the behavior in real transformers. Since the loss is generated by an inhomogeneous field, the incremental power loss, instead of specific loss, is evaluated.

A. Wattmeter-based loss measurement for RD flux

The wattmeter-based loss measurement equipment, such as the Epstein frame tester, comprises primary winding(s) used for setting up flux, secondary winding(s) used for voltage (flux) measurement, and the specimen to be tested. The setup forms an unloaded transformer. The schematic diagram for RD flux loss measurements is given in Fig. 2(a). The primary winding [to the left in Fig. 2(b)] is supplied with a sinusoidal current, generating the magnetic flux. The current in the secondary winding has a component in phase with the flux, known as the magnetization current, and a component 90° out of phase of the flux as a result of eddy current and hysteresis loss in the core.³¹ The current in the primary coil and the voltage of the secondary coil are supplied to the wattmeter, generating the loss from the current and voltage components in phase with each other. If the sample had no losses, the current and voltage would be 90° out of phase. In addition, the measurement disregards any power loss in the primary winding since the voltage drop of this winding is not measured.⁴ In the physical realization [Fig. 2(b)], the primary windings and the secondary windings form concentric windings, where the primary windings are located on the outside of the secondary winding. The individual primary windings and the individual secondary windings are connected in series.

The secondary voltage $V_{2,rms}$ is calculated from the desired value of magnetic polarization (which is practically equal to the magnetic flux density) by

$$V_{2,rms} = \sqrt{2} \pi f N_2 A B_{peak}, \quad (4)$$

where N_2 is the total number of turns of the secondary winding and A (m²) is the cross-sectional area of the corresponding core. Since the internal impedance of the voltage measurement is high, the voltage measurement is practically equal to the induced voltage, and the power consumed by the instruments in the secondary circuit is negligible. In a measurement, the power supply is tuned until the secondary voltage of the laminated frame reaches the values calculated from the designated flux densities. Then, the power losses

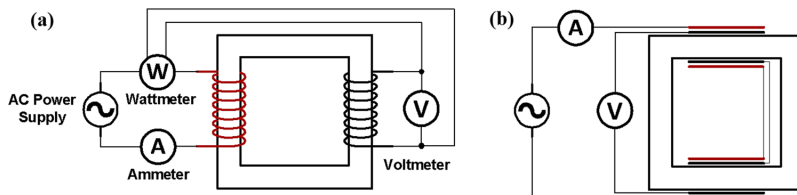


FIG. 2. The principle of wattmeter-based RD loss measurement (a) and the schematic diagram demonstrating the physical realization (b). The measurement system consists of primary winding, secondary winding, and the specimen (core). The current from the primary side and the voltage from the secondary side are incorporated into the wattmeter. In the physical realization (b), the primary windings (red) are located on the outside of the secondary windings (black).

from the power analyzer are recorded. The specific loss P_s (W/kg) is calculated by

$$P_s = \frac{N_1 P_m}{N_2 m}, \quad (5)$$

where P_m (W) is the reading from wattmeter and m (kg) is the mass of the sample.

B. Loss due to RD flux superimposed with TD flux

A schematic diagram for the measurement of the loss due to the combined action of RD and TD flux is given in Fig. 3. The main (RD) flux circulating the frame is generated by an ac power supply in the same way as in Sec. III A. To create the TD flux in the lamination, a notched ring core (NRC) is introduced. As for the main frame, the NRC is wound with primary and secondary windings, forming a concentric winding. The primary windings of the main frame and the NRC are excited by independent voltage supplies such that the phase shift between the two sources can be adjusted flexibly. The NRC is clamped on one branch of the lamination where the incident flux is forced to cross the lamination plane transverse to the rolling direction.

The secondary winding of the NRC is used as a voltage pickup coil. Based on Eq. (4), the voltage of the NRC is set to obtain the desired values of the magnetic flux densities. In a measurement, two power supplies are tuned until the secondary voltages of the lamination frame and the NRC reach the values calculated from the designated flux densities. Then, the power losses from the power analyzer are recorded. The total net loss P_{net} of the test specimen is a sum of the loss measured by the two coil systems withdrawing the power loss in the NRC,

$$P_{net} = \frac{N_1}{N_2} \bar{P}_m + \frac{N_1^a}{N_2^a} \bar{P}_m^a - P_{pow}, \quad (6)$$

where \bar{P}_m (W) and \bar{P}_m^a (W) are the losses obtained from the wattmeter of the main excitation system (supplies the RD flux) and the NRC excitation system (supplies the TD flux), respectively. The measurement is performed when both the lamination frame and the NRC are excited simultaneously. P_{pow} (W) is the power loss of the NRC, which needs to be measured according to the IEC standard³² under specified flux densities and frequency prior to fabrication. Furthermore, the specific loss of the effective volume involved in the RD flux superimposed with the TD flux can be defined,

$$P_s = \frac{1}{m_e} (P_{net} - P_{ineff}), \quad (7)$$

where m_e (kg) is the mass of the effective volume involved in the multidirectional flux. P_{ineff} (W) is the loss of the ineffective volume

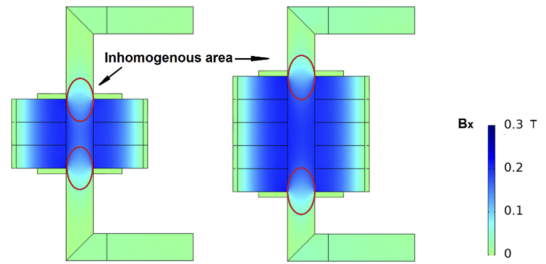


FIG. 4. Example of the transverse flux distribution (flux density in the horizontal direction, B_x) in the lamination. The end (inhomogeneity) effect is canceled out by subtracting the measurement of the 3-unit core from the measurement of the 5-unit core.

that is not exposed to the TD flux since only a unidirectional flux is involved in this region. The value of P_{ineff} can be obtained from the ac RD flux measurement.

The transverse flux distribution is less homogeneous at the ends of the frame volume (measurement volume) covered by the NRC as some of the TD flux passes outside the measurement volume (and thereby lower the flux inside the measurement volume); see Fig. 4. To counteract the effect of the flux inhomogeneity, we have assembled two NRCs with different dimensions, one NRC comprising three units of the rings and the other five units. The loss contributed by the inhomogeneity is, then, minimized by subtracting the measurement using the 3-unit NRC from the measurement using the 5-unit NRC. The difference between the two measurements is, then, the contribution from the TD flux area of two units in the middle where the flux is practically homogeneous (effective volume). Therefore, the measurement quantities P_m^a (W) and \bar{P}_m (W) in (6) are replaced with

$$\begin{cases} P_m^a = P_{m5}^a - P_{m3}^a, \\ \bar{P}_m = \bar{P}_{m5} - \bar{P}_{m3}, \\ \bar{P}_m^a = \bar{P}_{m5}^a - \bar{P}_{m3}^a, \end{cases} \quad (8)$$

where subscripts 3 and 5 indicate the measurement with the 3-unit core and 5-unit core, respectively.

C. Loss due to RD flux with dc-bias

The schematic diagram of the loss measurement system under the dc-bias is given in Fig. 5. Two methods of introducing dc-bias in the flux can be implemented. In the first method, we add the

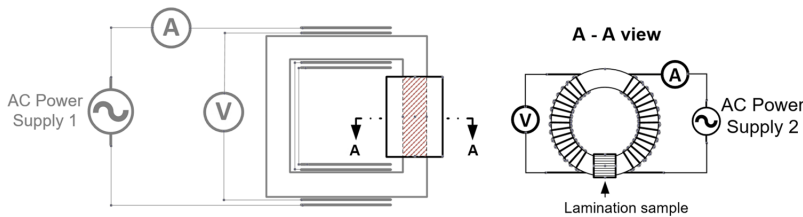


FIG. 3. Schematic diagram of the loss measurement system with the RD flux superimposed with the TD flux. The gray part is identical with Fig. 2. The ac power supply 2 connects to the primary winding wrapping around the NRC and supplies the TD flux. The NRC is clamped on one branch of the lamination such that the transverse flux crosses the lamination plane (red area).

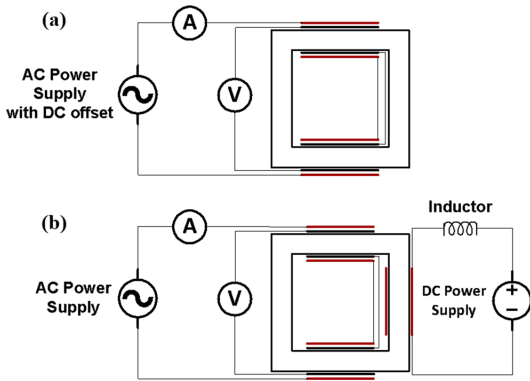


FIG. 5. Schematic diagram of the loss measurement system under the dc-bias. (a) The excitation voltage applied on the primary coil has a small dc-bias. (b) The dc-bias is introduced by a separate coil (on the right) connected to a dc power supply and an inductor for current smoothing.

voltage offset directly from the power supply [Fig. 5(a)]. In a measurement, the ac voltage source is tuned until the induced secondary voltage of the lamination frame reaches the value calculated from the designated flux density, and the dc voltage offset is tuned until the dc component of the primary current reaches the designated value. Then, the power losses from the power analyzer are recorded. The advantages of this approach are its simplicity and that it is similar to the real GIC scenario. The disadvantage is the need for delicate tuning of the dc voltage offset (dc-bias is an order of magnitude smaller than the ac signal due to the low resistance and the high number of turns of the primary winding). In the second method, we introduce a dc flux using a separate excitation coil [Fig. 5(b)], which enables an easy tuning since the dc flux is excited separately. The ac voltage source is tuned in the same way as in method 1, whereas

the dc current [corresponding to dc magnetomotive force (mmf)] is directly tuned to the designated value. However, a large inductance is required to smooth the current induced by the coupling system. In both the methods, the loss measurement is straightforward, and Eq. (5) is used to calculate the specific power loss.

D. Replica of actual leakage flux configuration

As described in Sec. I, we categorize the leakage flux into two typical configurations in actual situations. That is, depending on the position exposed, the leakage flux can either be normal or transverse to the core lamination. In the either case, inside the lamination, the penetrated flux turns to be parallel to the RD and returns to the leakage channel on the same side of the lamination plane. Therefore, the power loss is practically determined by the incident leakage flux (either TD or ND) combined with the penetrated flux parallel to RD. To reflect these actual flux configurations, a C-shaped core (CSC) is utilized to produce an “artificial leakage flux.” Instead of enforcing the flux crossing the lamination plane as in Sec. III B, the CSC imposes and absorbs the flux on the same side of the lamination. We mount the CSC in two positions so that the incident flux can enter either transverse (TD) or normal (ND) to the lamination plane, whereas the penetrated flux along the edge or surface is parallel to the RD.

Schematic diagrams for measurements representing actual leakage flux configurations are given in Fig. 6. As for the NRC, the CSC has primary and secondary windings. The primary windings of the CSC and the main frame are excited by independent voltage supplies such that their phase angle can be adjusted flexibly, whereas the secondary winding of the CSC is used as a voltage pickup coil. In configuration Fig. 6(a), the CSC is mounted on the side of the lamination where the incident flux is in the TD, whereas in configuration Fig. 6(b), the CSC is mounted on top of the lamination where the incident flux is in the ND. In a measurement, two power supplies are tuned until the induced secondary voltages of the lamination frame and the CSC reach the values calculated from the designated flux densities. Then, the power losses from the power analyzer are recorded.

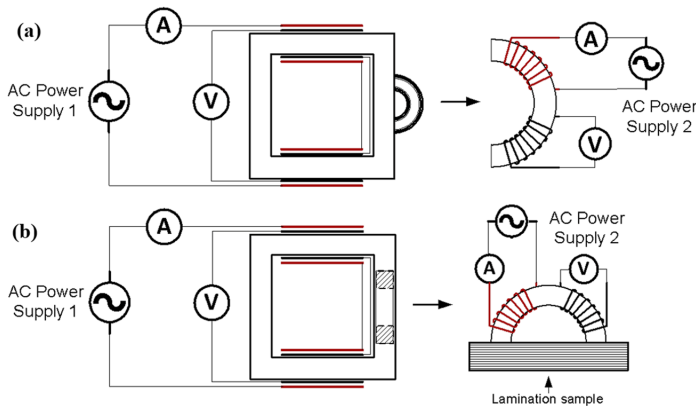


FIG. 6. Schematic diagram of the loss measurement system representing the actual leakage flux configurations. The AC power supply 1 connects to the primary windings wrapping around the square frame and supplies the main flux. The AC power supply 2 connects to the winding wrapping around the CSC. In the configuration (a), the CSC is mounted on the side of the lamination and supplies the TD flux to the lamination. In the configuration (b), the C-shaped core is mounted on the surface of the lamination and supplies the ND flux to the lamination.

To investigate the variation in loss due to an added flux, the concept of incremental loss, P_{incr} (W), is introduced, which is the difference between P_{net} (under the superimposed flux) and the arithmetic sum of the loss measured with the individual excitation systems alone (under the unidirectional flux),

$$P_{incr} = P_{net} - \left(\frac{N_1}{N_2} P_m + \frac{N_1^a}{N_2^a} P_m^a - P_{pow} \right) = \frac{N_1}{N_2} (\bar{P}_m - P_m) + \frac{N_1^a}{N_2^a} (\bar{P}_m^a - P_m^a), \quad (9)$$

where P_m (W) and P_m^a (W) are the losses of the main excitation system and the auxiliary excitation system measured individually. Note that \bar{P}_m is different from P_m since it changes with the applied flux.

Note that the replica of the leakage flux configuration only yields qualitative results and cannot directly be used for material characterization since the loss depend on the geometry chosen (e.g., size of the lamination frame and the cross section of CSC).

IV. LOSS MEASUREMENT SYSTEM

A. Lamination sample frame

The strips to be tested (cold rolled grain-oriented electric steel, Grade 30P120, Standard³³ JIS 2553, Japan) were cut along the rolling direction (with an angle tolerance of 1°), where the edge of the sheet defined the reference direction, and were, then, assembled into a frame. The frame was similar to an Epstein frame, with some important distinctions:

- The strips were assembled in a square with mitered joints (see Fig. 7), instead of double-lapped joints used in the Epstein frame. The angle of overlap was 45°. The mitered joints were preferred for two reasons: (1) the loss in the corner joints was minimized since the flux in the joint became parallel to that of grain orientation;²⁹ (2) the filling factor became close to that of a real transformer.
- The lamination frame consisted of two coil groups positioned on the opposite sides of the frame (see Fig. 7). Each coil group had two concentric windings: an outermost primary winding (magnetizing winding) and an innermost secondary winding (voltage pickup winding). The number of turns was selected to adapt to the power source, the measuring equipment, and the frequency.
- The overall thickness of the lamination stack was 30 mm (larger than the Epstein frame sample) to match the thickness of the powder core in the auxiliary excitation system.

TABLE I. Parameters of the lamination sample frame and the coils.

Parameters	Value	Unit
Total number of sheets	4 × 103	...
Total number of coils	2 or 3 ^a	...
Sheet width	30	mm
Sheet thickness	0.30 ± 0.03	mm
Frame outer length	280 ± 0.5	mm
Frame inner length	220 ± 0.5	mm
Frame cross-sectional area	900 ^b	mm ²
Effective frame cross-sectional area	871	mm ²
Length of individual coils	190	mm
Number of turns, primary coil	2 × 100	...
Number of turns, secondary coil	2 × 100	...
Primary coil wire diameter	2	mm
Secondary coil wire diameter	1	mm

^a3 is the number of coils used for the dc-bias test with separate excitation.
^b900 mm² is the geometric cross-sectional area.

Additionally, the chosen volume secured that the imposed flux channel was not limited by the thickness of the sheets.

The detailed design parameters are listed in Table I.

The laminated frame works as a no-load transformer, on which the maximum flux density applied is below the saturation point. Therefore, the power loss due to the leakage flux from the frame is insignificant. In addition, metallic loops are avoided around the branch of the frame as it would lead to extra loss, which would influence the measurement results. The coils were fixed to insulating supports (inner width 31 mm) and an aluminum baseplate.

The complete frame had several mechanical clamps to avoid displacement of the laminations due to strong vibration caused by magnetostriction. Equation (4) implies that a proper definition of the cross-sectional area is crucial to obtain the actual flux density. Considering a large deviation of the individual sheet thickness from the nominal value, the statistically reliable effective cross-sectional area,¹⁸ A , was used,

$$A = \frac{m}{4l\rho}, \quad (10)$$

where m (kg) is the total mass of the test specimen, l (m) is the length of a test specimen strip, and ρ is the mass density (7.65 kg/dm³ for 30P120³³). The calculated filling factor was 0.968.

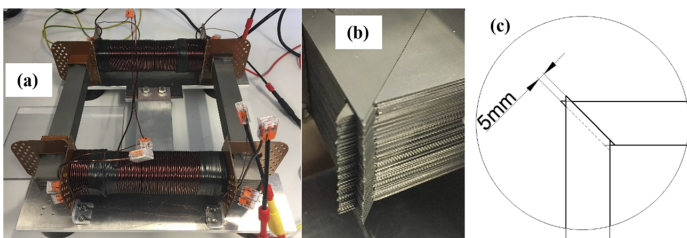


FIG. 7. The frame of the lamination sample with coils. (a) The lamination frame and the coils formed the magnetic circuit. The frame comprised a sheet lamination with 103 layers, 30 mm in height. The individual primary and secondary windings of the two coils were connected in series. [(b) and (c)] The mitered joints have a 5 mm offset, and the angle of overlap was 45°.

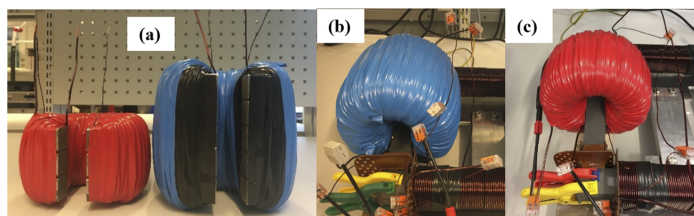


FIG. 8. NRCs and the excitation systems. (a) Notched ring cores (NRCs) are made of three units and five units of 25.4 mm wide powder rings with 30 mm slots. NRCs of five units (b) and three units (c) are mounted on the middle of the lamination branch.

B. NRCs and their excitation systems

The NRCs and the excitation coil systems are shown in Fig. 8. High flux (Magnetics©) powder cores, offering much higher saturation flux density (1.5 T) than ferrites and lower loss than powder iron cores, were used as the starting material. For experiments where low flux densities (<0.5 T) are of interest, a ferrite core can be an alternative to reduce core loss. The 30 mm opening (the notch) for the frame was machined from each 25.4 mm wide ring core. The two NRCs used were assembled using three and five units of powder rings, yielding total widths of 76.2 mm and 127 mm, respectively. The excitation and voltage pickup coils were wound around the NRCs. The detailed design parameters are listed in Table II. The attainable flux densities (peak values), the corresponding applied voltages, and the excitation currents are listed in

TABLE II. Parameters of the NRCs and the excitation systems.

Parameters	Value	Unit
Relative permeability of the ring	125	...
Outer diameter of ring	132.6	mm
Inner diameter of ring	78.6	mm
Height of ring	25.4	mm
Cross-sectional area of ring	678	mm ²
Total cross-sectional area, 3-unit NRC	3 × 678	mm ²
Total cross-sectional area, 5-unit NRC	5 × 678	mm ²
Number of turns, primary coil, 3-unit NRC	200	...
Number of turns, primary coil, 5-unit NRC	350	...
Number of turns, secondary coil, 3-unit NRC	100	...
Number of turns, secondary coil, 5-unit NRC	100	...
Primary coil diameter	1.95	mm
Secondary coil diameter	0.8	mm

TABLE III. Flux density, voltage, and excitation current ranges on the main and the NRC excitation systems at 50 Hz.

Excitation coil	Flux density (T)	RMS voltage range (V)	Excitation current (A)
Lamination frame	0–1.6	0–62	0–0.72
NRC (3 unit)	0–0.8	0–72	0–5.5
NRC (5 unit)	0–0.8	0–211	0–3.2

Table III. The loss in the lamination frame and the NRCs must be pre-measured individually over the span of flux densities used in the experiments.

C. CSC and its excitation system

Figure 9 shows the CSC with excitation and voltage pickup coils. Since the permeability of the powder core is much lower than that of GO steel, the impact of the main flux on the powder core is negligible when the GO steel works in its linear region. In the measurement where the flux superimposition takes place, the permeability of the GO steel reduces considerably. Consequently, the stray flux from the frame can enter the auxiliary core and influence measured power loss. To avoid the measurement inaccuracy introduced by the flux interaction, 1 mm thick plastic spacers were used to magnetically insulate the main frame flux from the saturated GO steels. The ring unit used in CSC was identical with the one in the NRC (see Table III). The coil parameters are listed in Table IV.

The CSC was placed in the middle of one branch of the frame using mechanical clamps. There are two possible positions for the CSCs, as described in Fig. 6. To obtain the incident flux in the normal

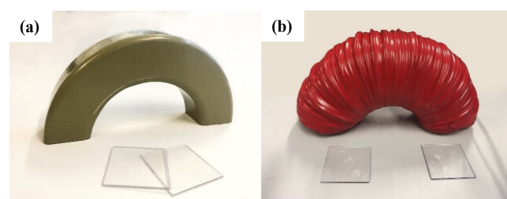


FIG. 9. CSC and the excitation system. (a) The C-shaped core (CSC) was made by a half ring unit. (b) The excitation and voltage pickup coils were wound around the CSC. Plastic spacers were used to create air gaps.

TABLE IV. Parameters of the CSCs and the auxiliary excitation systems.

Parameters	Value	Unit
Number of turns, primary coil	200	...
Number of turns, secondary coil	100	...
Primary coil diameter	1.95	mm
Secondary coil diameter	0.8	mm

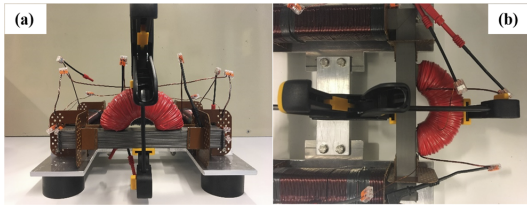


FIG. 10. The CSC was mounted on one branch of the lamination frame. (a) The CSC mounted on the plane of the lamination, yielding the incident flux in the normal direction. (b) The CSC mounted on the side of the lamination, yielding the incident flux in the transverse direction.

TABLE V. Flux density, voltage, and excitation current ranges on the main and the CSC excitation systems at 50 Hz.

Excitation coil	Flux density (T)	RMS voltage range (V)	Excitation current (A)
Lamination frame	0–1.6	0–62	0–0.72
CSC	0–0.8 ^a	0–24	0–6.1

^a0.8 T is the maximum flux density applied on the CSC, which is well below the saturation flux density of the powder core (High Flux Magnetics). The tests were performed with flux densities where the distortion of the induced voltage waveform was low (THD < 5%).

direction, the CSC was placed on the plane of the lamination; see Fig. 10(a). With the CSC mounted on one side of the lamination, the incident flux entered the laminations in the transverse direction; see Fig. 10(b). The desired flux densities and the corresponding applied voltages and excitation currents are listed in Table V. The losses in the auxiliary excitation system were pre-measured under the same given flux.

D. Measurement instruments

The main measurement instruments were a power supply and a high precision power analyzer; see Fig. 11. The lamination frame was connected to the instruments according to the circuit diagrams



FIG. 11. Measurement instruments. The setup consisted of the lamination test sample (1), the power analyzer, YOKOGAWA WT3000 power analyzer (2), and the power supply, ITECH IT7627 high power programmable AC power supply (3).

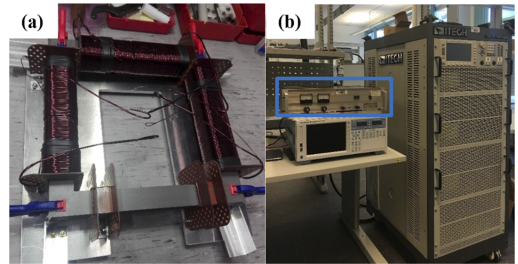


FIG. 12. Experimental setup for loss measurements under the dc-bias. In method 2, a dc-bias was introduced by a separate coil excited by a dc power source. (a) The coil for dc excitation was added as a third winding on the upper branch. (b) The dc excitation coil was controlled using a separate dc power source.

described in Sec. III. The power supply used could provide independent voltage sources where the phase difference, frequency, and magnitude between them were fully controllable. The current and voltage measurements were made with the power analyzer, where the power loss was obtained. Oscilloscope functions were embedded in both the power supply and the power analyzer such that the voltage, current waveforms, and the phase difference could be verified and recorded online.

Two distinct methods of introducing dc-bias were implemented according to Sec. III C. In the first method [Fig. 5 (a)], the resultant steady state dc current was determined by the dc voltage offset V_{dc} (V) and dc resistance R_{dc} (Ω) of the circuit. The definition is in line with the GIC definition,³⁴

$$I_{dc} = \frac{V_{dc}}{R_{dc}}, \quad (11)$$

The reading of the power loss P , peak value I_{peak} , and dc component I_{dc} (A) of the (magnetization) current were recorded from the power analyzer. The waveforms of the voltages and currents were saved to construct the magnetization curve.

In the second method, a separate excitation coil (Fig. 12) was used to introduce the dc flux. The turn number of the dc excitation coil (40 turns) was chosen based on the capacity of the measurement system and the power supply. With a high number of turns, the induced voltage on the dc excitation circuit becomes high, requiring a large inductance to smooth the current ripple. A lower number of turns demands a high dc current, which should be supplied by the dc power source and handled by the measurement instruments. A large inductance (600 mH was used in our test, giving ~3% current

TABLE VI. Voltage and current applied for loss measurement under the dc-bias.

Parameter	Range	Unit
Flux density	0–1.6	T
AC rms voltage applied	0–62	V
DC voltage range, method 1	0–0.5	V
DC current range, method 2	0–20	A

ripple) was used to smooth the induced current. The attainable ac flux densities (peak values), the corresponding voltages, and the dc voltages and currents are listed in Table VI.

V. MEASUREMENT EXAMPLES

A. Loss measurement with RD flux superimposed with TD flux

Loss measurement results for the sample exposed to RD superimposed with the TD flux of varying magnitudes are given in Fig. 13. For the entire TD flux density span, the difference in power loss between $B_{RD} = 1\text{ T}$ and $B_{RD} = 1.6\text{ T}$ is almost constant. Compared to the RD flux density, the TD flux has a major impact on the power loss, particularly when the TD flux density is high ($\geq 0.4\text{ T}$), whereas the phase angle has a lower impact on the power loss. Homogenous TD flux induces significantly higher per unit loss than the RD flux. However, the actual TD flux in the core is far from homogeneous and confined within a small region; thus, the loss contribution is insignificant.

B. DC-bias measurements

An example of the measurement of the B - H characteristics of the sample under different dc-bias levels is demonstrated in Fig. 14(a), using method 1. The comparison of the magnetization currents obtained from two methods is described in Fig. 14(b), and the corresponding frequency spectra are shown in Fig. 14(c). It is seen that the dc flux adds to the amplitude of the ac flux in one half-cycle and subtracts in the other half-cycle, resulting in half-cycle saturation.

The offset of the dc flux density depends on the magnitude of the dc current, the number of turns, and the reluctance of the flux path. The dc flux density cannot be measured by an inductive measurement method; therefore, a direct method, using a Hall effect sensor, is demanding due to the difficulty in placing the sensor in the lamination. To overcome the problem, we adopted a comparative method to derive the flux offset indirectly. In this approach, we used the ac over-excitation test result as a reference, i.e., a B - I_{peak} characteristic curve. I_{peak} obtained from the dc-bias test was compared to the preserved B - I_{peak} curve, where the maximum flux density B_{max}

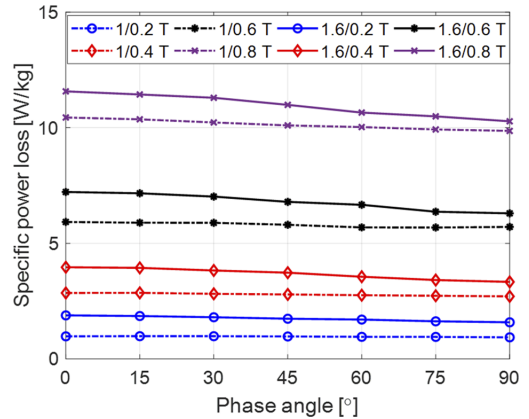


FIG. 13. Measured specific power loss vs phase angle in the region having the RD flux superimposed with the TD flux. RD flux densities were 1 T (dashed line) and 1.6 T (solid line). TD flux density varies from 0.2 T to 0.8 T.

was identified. Since the peak-to-peak flux density was obtained by the ac voltage source, the dc-bias was, then, calculated by

$$\Delta B = B_{max} - B_{ac}, \quad (12)$$

where B_{ac} corresponds to the applied ac voltage. The calculated offset flux densities corresponding to Fig. 14(a) were 0.236 T, 0.311 T, 0.349 T, and 0.371 T, respectively.

The comparison of magnetization currents [Fig. 14(b)] shows the similarity in the magnetization current waveforms. The difference is, in method 2, that the average of the current $I(t)$ over a period T should be zero, which gives the constraint,

$$\int_0^T I(t) dt = 0. \quad (13)$$

Despite the difference in spectra, the loss measured using the two methods is very similar; see Fig. 15. The small difference can be attributed to the ripple in the dc current using method 2. Another

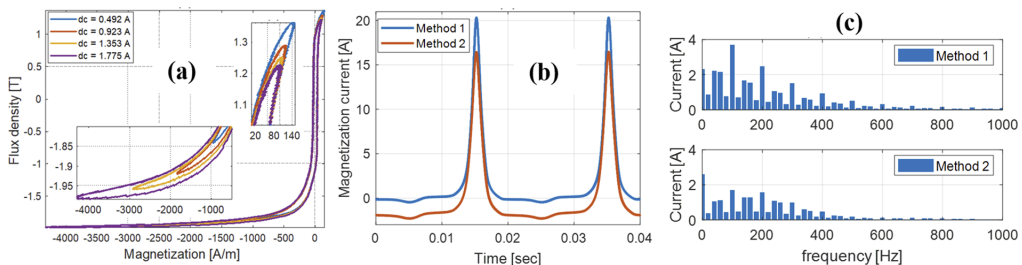


FIG. 14. Examples of loss measurements under the dc-bias. (a) Magnetization characteristic (B - H curve) under four different dc-bias levels using method 1. (b) Comparison of magnetization currents at $NI = 355\text{ A}$ (the number of turns is implicitly accounted) using the two methods. (c) Comparison of the spectra of magnetization currents using the two methods.

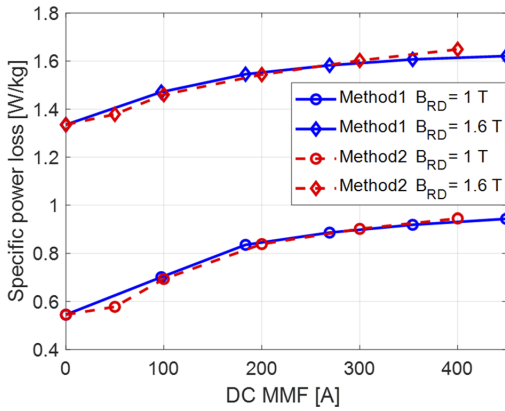


FIG. 15. Measured specific power loss vs dc magnetomotive force (dc-bias level) with the low ac flux density (1 T) and the nominal flux density (1.6 T). The dc magnetomotive force (mmf) is varied from 0 A to 450 A (the number of turns is implicitly accounted).

important observation is that the saturation effect of the power loss occurs as the dc magnetomotive force (mmf) increases. The moderate change in the hysteresis loss can be explained by the variation of the hysteresis loop in Fig. 14(a). Due to the dc offset of the flux, the area of the hysteresis loop increases in one half-cycle and reduces in the other half-cycle. As dc mmf further increases, the peak flux exceeds the saturation point in one half-cycle. Consequently, the increase rate of the hysteresis loop area starts to slow down in one half-cycle, while the decrease rate of the area is maintained in the other half-cycle. In combination, the total hysteresis loss asymptotically approaches a maximum value with increasing dc mmf.

Due to larger values of the magnetization current in method 1, the winding losses and stray losses (associated with the magnetic current) become higher when using method 1 than using method 2. Therefore, to be conservative, method 1 is recommended for transformer dc-bias tests.

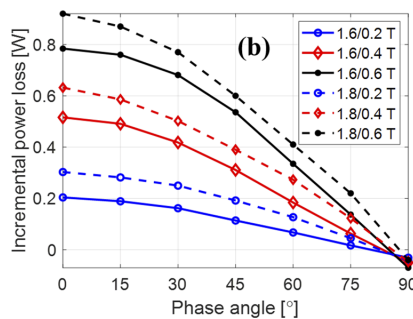
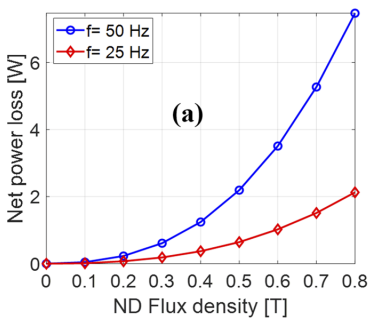


FIG. 16. Examples of loss measurements with the replicas of actual leakage flux configurations. (a) Net power loss in the lamination vs flux density in the normal direction (without RD flux) at 25 Hz and 50 Hz. (b) Incremental power loss vs phase angle in the transverse direction at 50 Hz. The RD flux densities are 1.6 T and 1.8 T, and the TD flux density varies from 0.2 T to 0.6 T.

C. Replicas of actual leakage flux configuration

Measurement results with replica of actual leakage flux configurations are demonstrated in Fig. 16. In Fig. 16(a), the power loss increases dramatically with an increase in ND flux density and frequency. The incremental loss due to the RD flux superimposed with the TD flux is demonstrated in Fig. 16(b). We can observe a significant increase in power loss with a decrease in phase angle between the RD and TD fluxes. This increment is due to the fact that the sum of the RD flux generated by the main field coil and the RD flux coming from the TD flux (as it flows in the RD direction to close the magnetic loop of the C-core) at small phase angles results in enhanced RD flux density amplitudes and thereby increased loss. Hence, the conventional no-load test underestimates the losses under inductive loading (small phase angle). The small discrepancy at 90° phase angle implies that the conventional no-load test gives a good estimation on overall core loss in normal operation.

As illustrated in Secs. I and III D, the leakage flux enters the core normal or transverse to the lamination plane. Initially, the flux is constrained within a small depth where it maintains its orientation inside the core; we call it the local zone. Inside the local zone, the induced loss due to the ND flux is dominated by the eddy current loss, whereas the loss due to the TD flux is dominated by the rotational power loss (when the TD flux and the RD flux are not in phase). Outside the local zone, the penetrated flux changes direction, turns to be parallel to the RD, and eventually returns to the leakage channel on the same side of the lamination plane. Here, the flux follows the edge of the core window and has a significantly larger influence area, which forms the global zone.

As the power losses measured under actual leakage flux configurations are combinations of the RD flux and ND (or TD) flux, it consists of loss contributed from both the local zone and the global zone. Flux superimposition not only increases the resultant magnitude of the flux density but also extends the influence region due to flux saturation. Figure 16(b) reveals that both the magnitudes of the RD flux and ND (or TD) flux and the phase angle between them play a crucial role in power loss enhancement, and the incremental loss predominantly takes place in the global zone. A small phase difference results in a larger increase in the resultant flux density and thereby a larger incremental loss, whereas the resultant flux density due to a 90-degree phase difference has a negligible increase in magnitude.

VI. SUMMARY AND CONCLUSIONS

In this paper, the detailed design of an apparatus for the measurement of losses in electrical steel laminations under the multidirectional and dc-bias flux has been presented. Experimental measurements demonstrate the apparatus' ability to provide loss measurements in a large range of flux densities and orientations important for studying iron core losses in, e.g., transformers under saturation.

The loss measurement system and measurement method could complement the existing standardized tests (Epstein testing and SST) in characterizing the losses influenced by the leakage flux and flux offset under various operation conditions and serve as a guide to design engineers regarding the loss distribution and potential local (or global) heat enhancement generated by the leakage flux and flux offset.

ACKNOWLEDGMENTS

This work was performed as a part of the project "Thermal Modeling of Transformers" (Project No. 255178) funded by the Research Council of Norway, Statnett, Hafslund, and Lyse Nett.

DATA AVAILABILITY

The data that support the findings of this study are available from the corresponding author upon reasonable request.

REFERENCES

- ¹T. Booth and H. Pfützner, *J. Magn. Magn. Mater.* **133**, 183–186 (1994).
- ²N. Hihat, J. P. Lecointe, S. Duchesne, E. Napieralska, and T. Belgrand, *Sensors* **10**, 9053–9064 (2010).
- ³T. Yagisawa, Y. Takekoshi, and S. Wada, *J. Magn. Magn. Mater.* **26**, 340–342 (1982).
- ⁴S. Zurek, *Characterisation of Soft Magnetic Materials under Rotational Magnetization*, 1st ed. (CRC Press, London, 2018).
- ⁵H. Pfützner, *IEEE Trans. Magn.* **30**(5), 2802–2807 (1994).
- ⁶L. R. Dupré, F. Fiorillo, C. Appino, A. M. Rietto, and J. Melkebeek, *J. Appl. Phys.* **87**(9), 6511–6513 (2000).
- ⁷T. Kochmann, *J. Magn. Magn. Mater.* **160**, 145–146 (1996).
- ⁸J. Wang, H. Lin, Y. Huang, and X. Sun, *IEEE Trans. Magn.* **47**(5), 1378–1381 (2011).
- ⁹X. Zhao, L. Li, J. Lu, Z. Cheng, and T. Lu, *IEEE Trans. Magn.* **48**(2), 747–750 (2012).
- ¹⁰J. G. Kappenman and V. D. Albertson, *IEEE Spectrum* **27**(3), 27–33 (1990).
- ¹¹G. Ma, L. Cheng, L. Lu, F. Yang, X. Chen, and C. Zhu, *J. Magn. Magn. Mater.* **426**, 575–579 (2017).
- ¹²P. R. Price, *IEEE Trans. Power Delivery* **17**(4), 1002–1008 (2002).
- ¹³R. Pirjola, *IEEE Trans. Plasma Sci.* **28**(6), 1867–1873 (2000).
- ¹⁴R. S. Girgis and C.-D. Ko, *IEEE Trans. Power Delivery* **7**(2), 699–705 (1992).
- ¹⁵Y. Jiang and A. Ekström, *IEEE Trans. Power Electron.* **12**(2), 287–293 (1997).
- ¹⁶E. V. Larsen, R. A. Walling, and C. J. Bridenbaugh, *IEEE Trans. Power Delivery* **4**(1), 667–673 (1989).
- ¹⁷H. C. Tay and G. W. Swift, *IEEE Trans. Power Appl. Syst. PAS-104*(1), 212–219 (1985).
- ¹⁸IEC 60404-2: 2008, Magnetic Materials-Part 2: Methods of Measurement of the Magnetic Properties of Electrical Steel Strip and Sheet by Means of an Epstein Frame.
- ¹⁹IEC 60404-3: 2009, Magnetic materials-Part 3: Methods of Measurement of the Magnetic Properties of Electrical Steel Strip and Sheet by Means of a Single Sheet Tester.
- ²⁰F. Brailford, *J. IEE* **95**, 38–48 (1948).
- ²¹F. Fiorillo *et al.*, in *Proceedings of the 1st 1&2DM Workshop* (1&2DM, Braunschweig, Germany, 1992), p. 162.
- ²²C. Ragusa *et al.*, *J. Magn. Magn. Mater.* **320**(20), e623–e626 (2008).
- ²³M. Enokizono, T. Suzuki, J. Sievert, and J. Xu, *IEEE Trans. Magn.* **26**(5), 2562–2564 (1990).
- ²⁴V. Gorican *et al.*, in *Proceedings of the 6th 1&2DM Workshop* (1&2DM, Bad Gastein, Austria, 2000), p. 66.
- ²⁵C. Appino, E. Ferrara, F. Fiorillo, L. Rocchino *et al.*, *Int. J. Appl. Electromagn. Mech.* **48**, 123–133 (2015).
- ²⁶W. Brix, K. Hempel, and F. Schulte, *IEEE Trans. Magn.* **20**(5), 1708–1710 (1984).
- ²⁷T. Nakata, N. Takahashi, K. Fujiwara, and M. Nakano, *IEEE Trans. Magn.* **29**(6), 3544–3546 (1993).
- ²⁸R. H. Pry and C. P. Bean, *J. Appl. Phys.* **29**(3), 532–533 (1958).
- ²⁹S. V. Kulkarni and S. A. Khaparde, *Transformer Engineering: Design and Practice*, 1st ed. (Marcel Dekker, New York, 2004), p. 42.
- ³⁰N. Stranges and R. D. Findlay, *IEEE Trans. Magn.* **36**(5), 3457–3459 (2000).
- ³¹H. Saadat, *Power System Analysis*, 3rd ed. (PSA Publishing, U.S., 2010), p. 105.
- ³²IEC 60404-6: 2018, Magnetic materials-Part 6: Methods of measurement of the magnetic properties of magnetically soft metallic and powder materials at frequencies in the range 20 Hz to 100 kHz by the use of ring specimens.
- ³³JIS C 2553: 2019, Cold-rolled grain-oriented electrical steel strip and sheet delivered in the fully processed state, Japanese Industrial Standard.
- ³⁴IEEE C57.163-2015, IEEE Guide for Establishing Power Transformer Capability while under Geomagnetic Disturbances.

Paper IV

W. Wang, A. Nysveen and N. Magnusson, “The influence of multidirectional leakage flux on transformer core losses,” *Journal of Magnetism and Magnetic Materials*, 2021. <https://doi.org/10.1016/j.jmmm.2021.168370>.

The influence of multidirectional leakage flux on transformer core losses

Wei Wang¹, Arne Nysveen¹, Niklas Magnusson²

¹Norwegian University of Science and Technology, Trondheim, NO-7491 Norway, weiwan@ntnu.no

²SINTEF Energy Research, NO-7465 Trondheim, Norway

Abstract—In a power transformer, the leakage flux enters the laminations of the iron core in different directions. Depending on the orientation of the leakage flux, it can add eddy current and hysteresis losses to the well-documented losses caused by the main flux. To study the principles of the influence of the leakage flux on the losses in transformer cores, the problem was isolated to an experiment on a stack of laminations in an Epstein-like frame. The frame carried the main flux, while artificial leakage flux is created and forced to enter the laminations in the two directions perpendicular to the main flux. Additionally, the system was modelled using finite elements to interpret the physical phenomena. The results revealed that the loading conditions have a significant impact on the local eddy current loss and on the overall power loss. The identified additional magnetic losses show that under inductive loading, conventional no-load tests can underestimate the core losses considerably.

Index Terms—Eddy current; Lamination; Magnetic anisotropy; Magnetic flux leakage; Magnetic losses; Power transformer.

I. INTRODUCTION

RENEWABLE energy and heavy industries introduce more variable load patterns for power apparatuses such as power transformers than what they originally have been designed for. The understanding of the magnetic losses under such load patterns, can allow for a controlled upgrading, including acceptance of short time overloads of existing transformers. Such operation outside the transformers' design specifications can greatly reduce the need for costly reinvestments in the power grid. On the other hand, higher loads lead inevitably to higher leakage flux, which can stress the transformers.

Laminated iron cores close to the windings are exposed to this leakage flux. Depending on the location, the leakage flux enters the core from different directions, going from being parallel to perpendicular to the lamination plane when going from inside the yoke window to outside the yoke. The leakage flux generates additional power losses [1], which can both influence the overall power loss level in the core and the local power loss, the latter with the risk of generating excessive heat close to the core surface, which can result in deterioration of the core insulation and degradation of the insulating oil. With the variable load situations arising, knowledge of the additional magnetic losses appearing due to stray flux becomes increasingly important.

The influence of the leakage flux on stray losses in the structural parts of transformers have been extensively studied [2]-[3]. For the magnetic core, the magnetic properties are measured in the rolling direction (RD) in the standardized specification [4]-[5]. While not yet standardized, 2-dimensional single sheet testing (SST) with various yoke

configurations have been proposed [6]-[9]. Due to the limited area of uniform magnetization, the measurement does not allow for averaging of the properties over a large volume [6]. In addition to the investigation on the plane of a single sheet, loss measurements have been performed in lamination due to flux in the normal direction (ND) [10]-[12]. However, dedicated studies on the impact of the leakage flux on the core losses largely lack. As the leakage flux imposes onto lamination core in different channels [13] and with various phase [14], such studies should account both for the spatial loss distribution and different phase angles (i.e. resistive or inductive load conditions). In both standardized methods [4]-[5], the power loss is determined for flux densities with a single sinusoidal and unidirectional excitation. To study the magnetic loss in electrical sheets with the combined action of multi-directional flux, a measurement system based on the wattmeter method and the basic Epstein frame geometry was developed [15]. The system was designed to characterize the power loss due to ac magnetic flux densities in RD combined with flux densities in the transverse or normal direction. Additionally, the actual leakage configurations were emulated in the laminated core for the studies of the associated losses.

In this paper, we investigate the loss features under leakage flux entering the laminations and interacting with the main flux. The magnetic losses are measured for different flux magnitudes and orientations, and at varying phase angle between the leakage flux and the main flux. Additionally, the results are physically interpreted using finite element analysis.

II. LEAKAGE FLUX CONFIGURATIONS AND POWER LOSS CHARACTERISTICS

The orientation of the leakage flux inside a single-phase transformer is schematically demonstrated in Fig. 1. The directions where the leakage flux enters the laminated core lead to the following definitions:

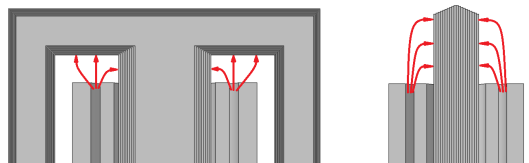


Fig. 1. Schematic drawing of the leakage flux at the top of the winding of a single-phase transformer. Left: TD; Right: ND.

1. **Transverse direction (TD):** Below the yoke, the flux enters the core in parallel with the plane of the lamination and perpendicular to the rolling direction.

2. **Normal direction (ND):** Ninety degrees outside the yoke, the flux enters the core perpendicular to both the plane of the lamination and the rolling direction.

The definition of the flux direction relative to a grain-oriented (GO) lamination block is illustrated in Fig. 2.

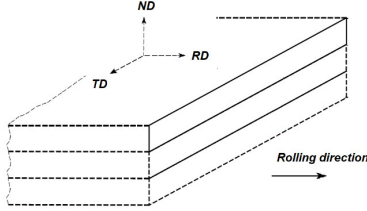


Fig. 2. Flux orientations in the grain-oriented steel laminations. RD: rolling direction; ND: normal direction; TD: transverse direction.

An example of leakage flux configuration is demonstrated in the simulation of a single-phase transformer (Fig. 3). The model is linear and no magnetic saturation is considered in the simulation. The high voltage (outer) winding sets up the main flux which circulates around the core window; the low voltage (inner) winding is connected to a load and the current in it sets up a balanced MMF. The leakage flux channel mainly locates between the two windings. Outside of the winding channel, the leakage flux entering the core (in either TD or ND) at the top of the transformer eventually turns and becomes parallel to the rolling direction before it again leaves the core at the bottom of the transformer. This flux path inside the core suggests two zones with different loss characteristics:

1. **Local zone:** Where the flux enters the core in either ND or TD, the flux orientation is maintained within a small depth in the core. The induced loss is associated with either eddy current loss (due to ND flux) [10]-[12] or rotational power loss (at TD flux) [6].
2. **Global zone:** As the entering flux changes direction and becomes parallel to the main flux (in RD), it follows the edge of the core window.

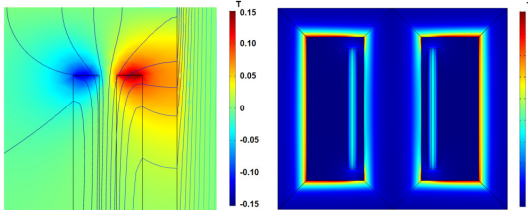
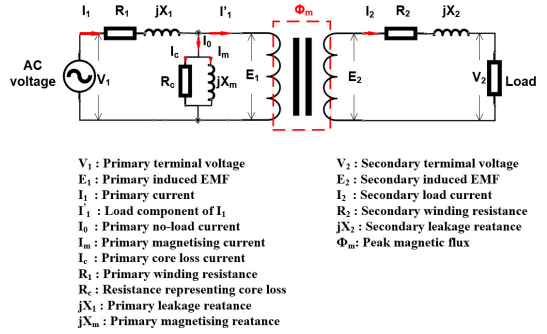


Fig. 3. Illustration of the local zone (left) and the global zone (right) of the leakage flux distribution in the core of a single-phase power transformer. Left: Leakage flux density component in x-axis (perpendicular to the limb). Right: Penetrated flux concentrated along the edge of the core window.

A transformer is operated under various loaded conditions. The magnitude of the secondary current I_2 depends on the secondary terminal voltage V_2 and the load impedance. The phase angle between I_2 and V_2 depends on the nature of the load. The load can be resistive, inductive or capacitive. The well-known schematic diagram of a loaded transformer at

load condition is shown in Fig. 4.



- | | |
|---|--------------------------------------|
| V_1 : Primary terminal voltage | V_2 : Secondary terminal voltage |
| E_1 : Primary induced EMF | E_2 : Secondary induced EMF |
| I_1 : Primary current | I_2 : Secondary load current |
| I'_1 : Load component of I_1 | R_2 : Secondary winding resistance |
| I_0 : Primary no-load current | jX_2 : Secondary leakage reactance |
| I_m : Primary magnetising current | Φ_m : Peak magnetic flux |
| I_c : Primary core loss current | |
| R_1 : Primary winding resistance | |
| R_c : Resistance representing core loss | |
| jX_1 : Primary leakage reactance | |
| jX_m : Primary magnetising reactance | |

Fig. 4. Schematic diagram of a loaded transformer.

The primary no-load current I_0 induces the magnetomotive force (MMF) $N_0 I_0$, which set up the flux Φ_m in the transformer core. Likewise, the secondary current I_2 induces the demagnetizing MMF $N_2 I_2$ on the secondary winding of the transformer, setting up the counteracting flux Φ_2 . N_1 and N_2 are the number of turns in the primary and secondary windings, respectively. An equilibrium is established when the primary current creates ampere-turns balance with the current of the secondary winding. The phasor diagrams of the actual transformer under resistive loading and inductive loading conditions are shown in Fig. 5.

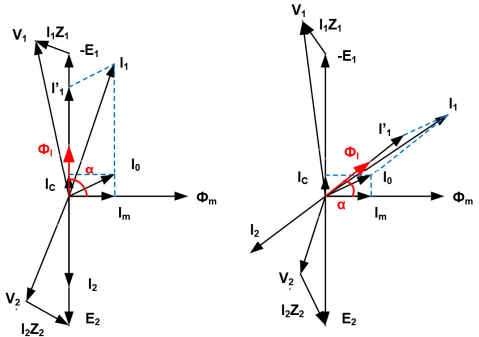


Fig. 5. The example of phasor diagram representing a loaded single-phase transformer. Left: resistive loading; Right: inductive loading.

The part of the flux produced by the primary winding, which does not link with the secondary winding, forms the leakage flux. The phase of the leakage flux Φ_1 is in phase opposition with the load current. As shown, under resistive loading, the phase difference, α , between the core flux and the leakage flux is 90° , whereas under inductive load, α can decrease significantly depending on the phase of the load current. The phasor diagrams in Fig. 5 has demonstrated how load characteristic changes the phase difference between the main flux and the leakage flux. Therefore, the superimposition of the leakage flux and the main flux inside the transformer core is complicated not only by the directions, but also by the phase difference.

III. EXPERIMENT

As described in section II, the core losses not only depends on the main flux flowing in the rolling direction, but also influenced by the imposed multidirectional leakage flux. However, the standardized measurement methods [4]-[5] are insufficient to determine how different factors affect the power loss. To study the loss behavior with the combined action of main flux and leakage flux, a set of experiments were carried out. The experiments were organized in two parts: the reference measurement (III. B) was performed by using standardized measurement method (SST) for material characterization. The measurement results (magnetization curve and specific loss) provided the input for the later finite element analysis. The specific measurements for multidirectional flux (III. D and E) were performed based on the measurement system [15], which was designed to characterize the power loss due to ac magnetic flux densities in RD combined with flux densities in the transverse or normal direction.

A. Test samples

The strips to be tested (cold rolled grain oriented electric steel, Grade 30P120, JIS 2553 [16], Japan) were cut along the rolling direction (with angle tolerance of 1°), where the edge of the sheet defined the reference direction. The burr shall be <0.02 mm in specimen cutting. For unidirectional reference measurements, single strips (50 mm×150 mm) were used for single sheet tests (SSTs). For measurements in multidirectional flux, the sheets were cut into 30 mm×280 mm strips with 45° angle corner at both ends, and then assembled to form a frame [15] (see Fig. 8), similar to an Epstein frame, with mitered joints with the angle of overlap being 45°. The overall thickness of the lamination stack was 30 mm.

B. Reference measurements

To be used as a reference in the loss evaluation, the specific loss of the GO electrical steel was measured at 50 Hz as function of flux density according to the standard [5]. The losses were measured in the rolling direction (RD) and the transverse direction (TD) by means of single sheet tests (SSTs), see Fig. 6.

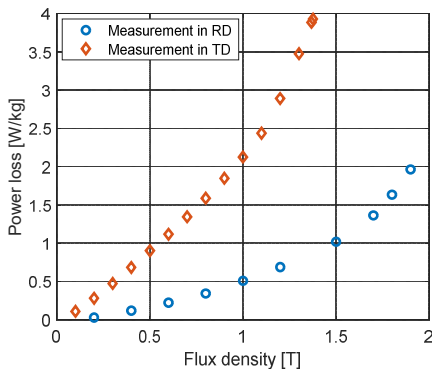


Fig. 6. The measured power losses in the GO electrical steel versus flux density. The measurement was performed in the rolling direction (RD) and the transverse direction (TD).

For the material definition to be used in the finite element analysis in Section IV, the magnetic permeabilities in two orthogonal directions up to the saturation level are obtained to account for the material anisotropy and the nonlinear effect [12]. The corresponding measurements were performed on the GO steel in RD and TD by SSTs. Two μ - B curves (μ_x - B_x curve for $B_y=0$ and μ_y - B_y curve for $B_x=0$) are shown in Fig. 7.

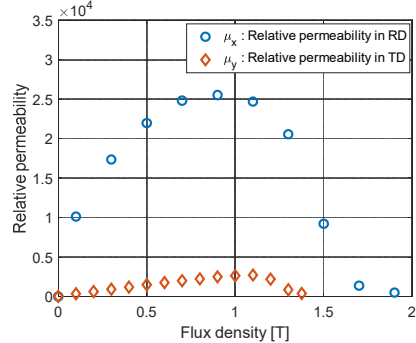


Fig. 7. The components of the permeability tensor versus flux density measured using the single sheet tester (SST). (μ_x : rolling direction, RD; μ_y : transverse direction, TD).

C. Loss measurement instrument for multidirectional flux

The measurement system developed for measurements of the losses under the combined action of RD and either TD or ND flux is described in detail in [15]. An overview of the system is given.

The main flux is generated in an Epstein-like frame with excitation coils and voltage pick-up coils, see Fig. 8. Each coil group had two concentric windings: an outermost primary winding (magnetizing winding), and an innermost secondary winding (voltage pick-up winding). A C-shaped powder core is used to produce an ‘artificial leakage flux’ (Fig. 9). The C-shaped core can be positioned such that it imposes the flux either in TD or ND.

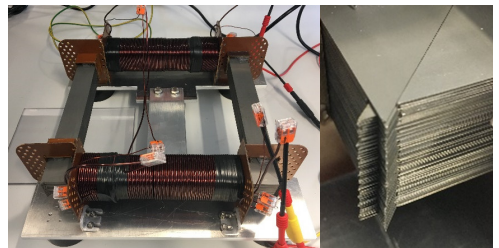


Fig. 8. The frame of the lamination sample with coils. The lamination frame and the coils formed the magnetic circuit. The frame comprised a sheet lamination with 103 layers, 30 mm in height. The individual primary and secondary windings of the two coils were connected in series. The mitered joints have a 5 mm offset and the angle of overlap was 45°.

The test object (Fig. 8) has two major differences comparing to a single-phase transformer (Fig. 1). First, the main flux circulates in the square frame instead of a core window. From flux distribution perspective, the Epstein-like frame is equivalent to a ‘half’ single-phase transformer.

However, the shape of steel strips used to build the frame is uniform and the complexity of assembly work is reduced. Moreover, for the material preparation and characterization, the standardized procedure [4] is available to follow.

Secondly, a C-shaped core is used to emulate leakage flux generated by the windings. Compared to the winding leakage flux, the artificial leakage flux has well defined incident areas, positions and directions, fully controllable magnitudes and phases of the flux densities. More importantly, by using specified leakage flux produced by the C-shaped core, the abovementioned factors can be studied independently. The detailed design parameters are listed in Table I.

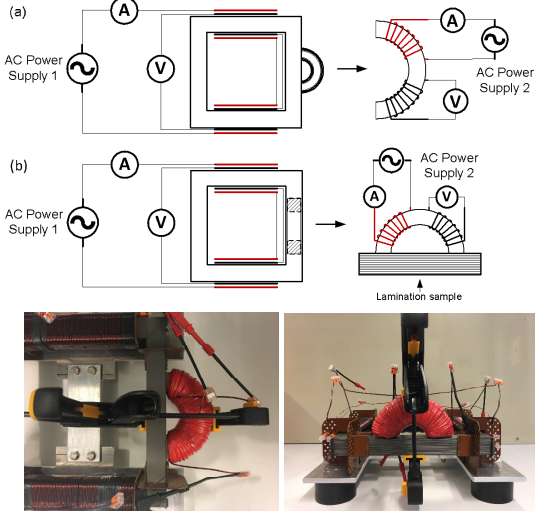


Fig. 9. The loss measurement system with artificial leakage flux superimposed with the main flux. The AC power supply 1 is connected to two coils wound around the square frame and the coil current generates the main flux in the frame. The AC power supply 2 is connected to a coil wound around the C-shaped core and the coil current generates the leakage flux to the lamination. The C-shaped core is mounted either on the side of the lamination (a) for TD flux or on the top of the lamination (b) for ND flux.

The measurement principle is based on the wattmeter method, where the primary current and secondary (induced) voltage are used to obtain the power loss. The secondary voltage $V_{2,rms}$ is calculated from the desired value of magnetic flux density B_{peak} by

$$V_{2,rms} = \sqrt{2}\pi f N_2 A B_{peak} \quad (1)$$

where N_2 is the total number of turns of the secondary winding and A is the cross-sectional area of the corresponding core. Since the secondary voltage contains only inductive voltage, the winding (resistive) loss is not involved in the measurement and thereby not sensitive to the temperature variation.

The net loss P_{net} (the total power loss subtracted by the loss in the powder core) of the test specimen and the incremental loss P_{incr} (the difference between the net loss P_{net} under superimposed flux and the arithmetic sum of the loss measured with individual excitation systems alone under unidirectional flux) due to flux superimposition are obtained.

$$P_{net} = \frac{N_1}{N_2} \tilde{P}_m + \frac{N_1^a}{N_2^a} \tilde{P}_m^a - P_{pow} \quad (2)$$

$$P_{incr} = P_{net} - \left(\frac{N_1}{N_2} P_m + \frac{N_1^a}{N_2^a} P_m^a - P_{pow} \right) \quad (3)$$

$$= \frac{N_1}{N_2} (\tilde{P}_m - P_m) + \frac{N_1^a}{N_2^a} (\tilde{P}_m^a - P_m^a)$$

where \tilde{P}_m and \tilde{P}_m^a are the losses obtained from the wattmeter of the main excitation system (supplies the RD flux) and the auxiliary excitation system (i.e. the C-shaped core supplies the TD/ND flux) respectively [15]. The measurement is performed when both the lamination frame and the C-shaped core are excited simultaneously. In contrast, P_m and P_m^a are the losses of the main excitation system and the auxiliary excitation system measured individually. P_{pow} is the power loss of the C-shaped core, which needs to be measured according to [17] under specified flux densities and frequency prior to fabrication.

The phase difference between the artificial leakage flux and the main flux can be varied from 0° to 90° , which corresponds to from inductive to resistive loading of transformers.

TABLE I
PARAMETERS OF THE LAMINATION SAMPLE FRAME AND COILS

Parameters	Value	Unit
Total number of sheets	4×103	/
Total number of coils	2	/
Sheet width	30	mm
Sheet thickness	0.30±0.03	mm
Frame outer length	280±0.5	mm
Frame inner length	220±0.5	mm
Frame cross-section area	900	mm ²
Effective frame cross-section area	871	mm ²
Length of individual coils	190	mm
Number of turns, primary coil	2×100	/
Number of turns, secondary coil	2×100	/
Primary coil wire diameter	2	mm
Secondary coil wire diameter	1	mm

900 mm² is the geometric cross-sectional area.

D. Losses due to combined RD and TD magnetic flux

Loss measurements of the electrical steel were performed under the combined action of RD main flux and TD leakage flux at power frequency (50 Hz). The RD flux density (peak value) was set to 1.6 and 1.8 T. The TD flux was varied up to 0.6 T and was applied at different phase angles relative the RD flux.

The incremental loss (the total loss subtracted by the RD and TD loss measured individually) is given as function of phase angle in Fig. 10. The incremental loss increases with the magnitudes of the TD flux density as well as the RD flux density. The highest incremental loss occurs when the two fluxes are in phase, whereas the field components act practically independent of each other when the RD and TD fluxes are 90 degrees out of phase. This increment is predominated by the effect of the flux superimposition. As described in Section II, the flux inside the lamination is largely constituted by the one parallel to the RD. Therefore, a smaller phase difference results in a higher flux density and thereby higher power loss.

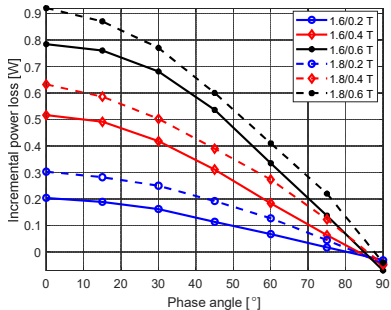


Fig. 10. Incremental power loss versus phase angle with the main flux superimposed with the transverse flux. The main flux densities are 1.6 T and 1.8 T; the transverse flux density varies from 0.2 T to 0.6 T.

E. Losses due to combined RD and ND magnetic flux

The power loss due to ND flux was measured at 50 Hz and 25 Hz and the flux density was varied from 0.2 T to 0.8 T, see Fig. 11. The power loss increases rapidly with the ND flux density and with frequency. This is due to the combined effect of the nonlinearity and anisotropy of the steel lamination, where the flux saturation extends the eddy current region and further increases the eddy current loss [12].

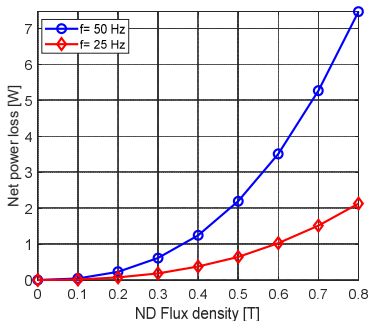


Fig. 11. Net power loss in the lamination versus flux density in the normal direction (without RD flux) at 25 and 50 Hz.

The measurement is further performed under the combined action of RD main flux and ND flux of varying phase angle. The frequency was 50 Hz, the RD flux density (peak value) was set to 1.6 T and the TD flux was either 0.2 or 0.4 T. The results are shown in Fig. 12.

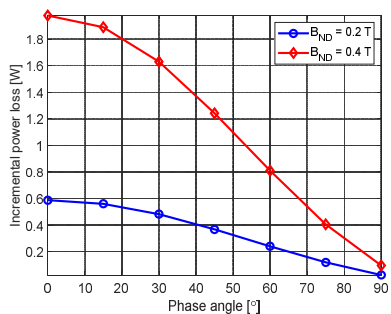


Fig. 12. Incremental power loss versus phase angle with the main flux superimposed with the normal flux. RD flux density $B_{RD}=1.6$ T; ND flux density and TD flux density are $B_{ND}=0.2$ or 0.4 T.

Similar to the case of TD flux, the incremental loss induced by the ND flux increases as the phase difference between the two fluxes decreases. At the phase angle of 90 degrees, there is almost no difference in loss compared to the sum of the losses measured individually ND and TD flux.

However, comparing to the TD flux density of the same level, the ND flux produces much larger incremental loss and this incremental loss increases disproportionately to the magnitude of the ND flux density.

IV. FINITE ELEMENT ANALYSIS

A. Finite element model

The measured power losses consist of different types of losses, inseparable by the measurement results alone. To understand the physical phenomena of the experiment and to gain insight of the loss mechanisms associated with different flux configurations, the finite element (FE) models were developed. A two-dimensional (2D) FE model was developed to investigate the TD flux. Considering that the eddy current distribution is three-dimensional (3D), a 3D FE model was developed to investigate the ND flux. The geometry view of the 2D and 3D model is illustrated in Fig. 13.

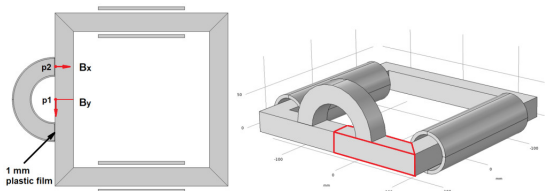


Fig. 13. The geometry view of the 2D and 3D models. Left: 2D model to study the TD flux and its flux superimposition with RD flux. Right: 3D model to study ND flux and its flux superimposition with RD flux.

The homogenization scheme is implemented in the material definition in the 3D finite element models [12] [18]. The equivalent relative permeability in the ND, μ_z is 30, determined by the stacking factor of the lamination and the equivalent conductivity in the ND, σ_z is 208 S/m, calculated based on the intrinsic conductivity of the electrical steel and the lamination geometry [19].

B. Simulation of TD flux combined with RD

Power losses measured in Section III.D consists of the loss contributed by the RD flux as well as the rotational field. The former is determined by the magnitude of the resultant RD flux density and the latter relies on both the RD flux and the TD flux. A numerical simulation was employed to calculate the two contributions separately.

Firstly, the flux density distribution in the lamination was examined. The simulation was made under unidirectional flux (without RD flux in the lamination frame) as well as under flux superimposition of varying phase angle. Figure 14 demonstrates the comparison of the flux distribution in the lamination with and without flux superimposition.

- With TD flux alone, the flux turns to become parallel to RD along the edge. Due to material anisotropy, the flux concentrates in a narrow flux channel and the magnitude of the RD flux density (0.67 T, B_y defined at P1 in Fig. 13) is larger than the incident ND flux density (0.2 T, B_x defined at P2 in Fig. 13).
- With RD flux alone, the flux distributes homogeneously in the lamination frame with practically no flux flowing in the C-shaped core. However, when the permeability of the lamination steel is close to that of the C-shape core (heavy saturation), some flux could flow into the C-shaped core. To avoid this flux interaction, 1 mm plastic films (air gap) were positioned between the C-core and the main frame to isolate the flux (Fig. 13) [15].
- When superimposing TD flux in phase with the RD flux, B_y increases. As demonstrated in the B_y curve, the superimposition is not linear, i.e. the resultant flux density under flux superimposition is not the arithmetic sum of previous two fluxes. Instead, the saturation effect significantly extends the TD flux influence area (global zone). The combined effect of the increased magnitude of the RD flux density as well as the extended area contributes to the loss increment (Fig. 10).

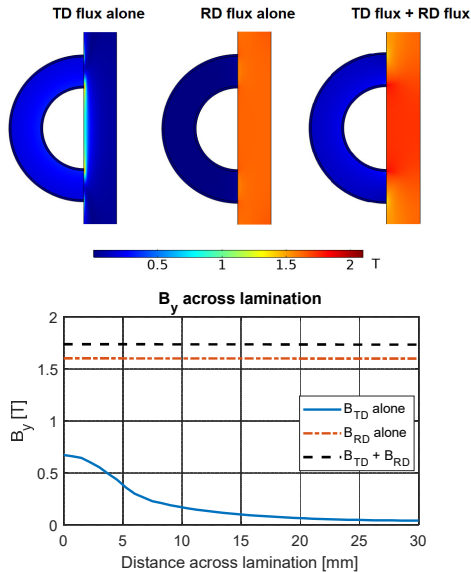


Fig. 14. Flux distribution in the steel lamination with incident TD alone (Left: $B_{TD}=0.2$ T; $B_{RD}=0$ T), RD alone (Middle: $B_{TD}=0$ T; $B_{RD}=1.6$ T) and with incident TD flux superimposed with RD flux (Right: $B_{TD}=0.2$ T; $B_{RD}=1.6$ T). The lower curve figure give the flux density in vertical direction B_y along the line in the middle of the lamination (red line in Fig. 13) corresponding to three scenarios in the upper figure.

Figure 15 demonstrates the flux density distribution in the horizontal direction. The contour of the B_x explicitly defines the ‘local zone’ associated with the TD flux as previously described in Fig. 5 (left). Apparently, the area of the local zone increases with a decreasing phase angle. At 90° phase angle,

the area of the local zone is minimum. However, the area of the local zone is significantly smaller than the global zone, which indicates its relatively small loss contribution to the overall loss. This will be justified by the following calculation.

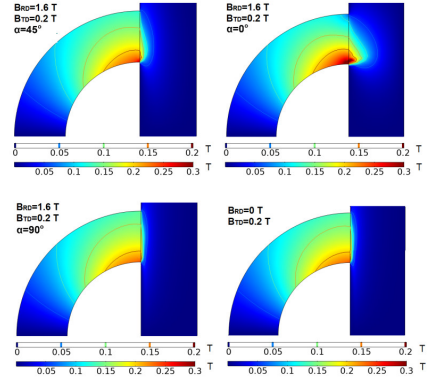


Fig. 15. Flux density in the horizontal direction B_x with incident TD flux superimposed with RD flux and with incident TD flux alone (lower right).

The power loss involving the rotational magnetic field can be estimated by the sum of the losses in two orthogonal directions [20]. Thereby, the total power loss is calculated by

$$P_{tot} = \int_V [P_x(\max_T(B_x)) + P_y(\max_T(B_y))] dV \quad (4)$$

where $P_x(B)$ and $P_y(B)$ are the specific loss density with respect to the peak flux density in TD and RD respectively. The reference specific loss [W/kg] measurement in two orthogonal directions (RD and TD) obtained by SST has been implemented in the finite element model. Considering the flux in two orthogonal directions not being always in phase (the peaks do not appear at the same time), the maximum value over a period shall be used.

The calculation example is given under TD flux density $B_{TD}=0.2$ T and RD flux density $B_{RD}=1.6$ T. As demonstrated in Table II, the power loss can be predicted accurately by (1). The calculation results gives an insight to the constitution of the measured power loss, which reveals that that the power loss is predominated by the RD flux and a decreased phase angle gives a rise on the resultant RD flux density, and thereby induces higher loss. On the contrary, the contribution from TD flux is small and can be ignored in practice.

TABLE II
NET POWER LOSS DUE TO TD FLUX COMBINED WITH RD FLUX

Phase angle [°]	Flux density at p1, B_y [T]	Net power loss in the core lamination [W]			Measurement /
		RD	TD	Total	
0	1.737	8.923	0.0270	8.95	8.92
15	1.733	8.917	0.0268	8.94	8.91
30	1.726	8.906	0.0255	8.93	8.88
45	1.711	8.882	0.0229	8.90	8.83
60	1.672	8.810	0.0187	8.83	8.79
75	1.646	8.784	0.0152	8.80	8.74
90	1.607	8.677	0.0122	8.69	8.69

C. Simulation of ND flux combined with RD

Power losses induced by the ND flux consists of eddy current loss and hysteresis loss, where the latter is determined by the magnitude of the resultant RD flux density. The simulation is firstly made solely under ND flux (without flux superimposition). The calculation agrees very well with the measurement (see Fig. 16), showing that the eddy current constitutes the majority of the total power loss under ND flux. The small contribution from hysteresis loss explains why the measured power loss (in Fig. 11) has a frequency dependent factor less than the power of 2 (approximately 1.8).

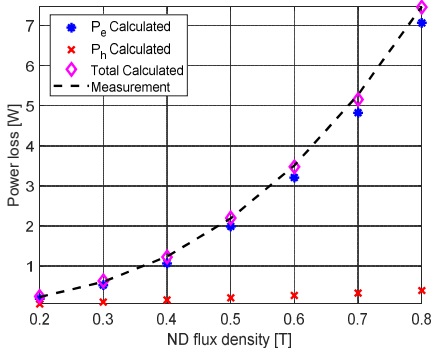


Fig. 16. The calculated power loss and the measured power loss under varying ND flux density. The calculated power loss has been separated by simulations, where P_e is the calculated eddy current loss and P_h is the calculated hysteresis loss.

With ND flux superimposed with RD flux, the distribution of the eddy currents has significantly changed and the phase difference between two fluxes plays a vital role in power loss enhancement. Fig. 17 shows the eddy current distribution under the flux superimposition between RD flux (1.6 T) and ND flux (0.2 T) at 90° and 0° , respectively.

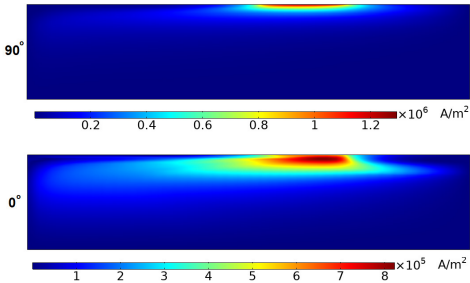


Fig. 17. The eddy current distribution in the lamination (red region highlighted in Fig. 13) under the ND flux (0.2 T) superimposed with the RD flux (1.6 T) at phase angle of 90° and 0° .

It is evident that the eddy current is concentrated close to the surface at 90° phase angle. In contrast, at 0° phase angle, the eddy current region is largely extended due to the saturation caused by flux superimposition. The extended eddy current volume leads to a significant loss increment, which explains the strong phase dependent eddy current loss shown in Fig. 12.

Under flux superimposition, the decreased phase angle also increases the hysteresis loss due to increased magnitude of the flux density, similar to the scenario discussed in Section III.B. As shown in Fig. 18, this incremental hysteresis loss can be comparable to the incremental eddy current loss. However, eddy current loss density is significantly larger than that of the hysteresis loss. More importantly, as the eddy current loss increases more rapidly with ND flux than the hysteresis loss, it becomes rather dominating (see Fig. 12) under higher ND flux density (0.4 T).

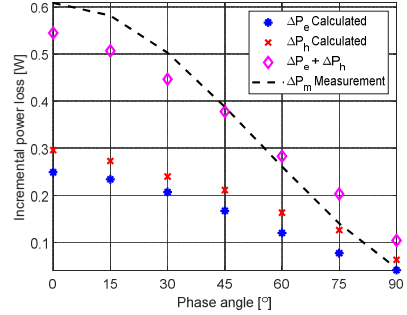


Fig. 18. The calculated incremental power loss and the measured incremental power loss under varying phase angle, ND flux density is 0.2 T and RD flux density is 1.6 T.

V. DISCUSSION

Loss impact has been categorized into the local zone and the global zone in the core lamination, according to the flux path and its orientation. The associated loss characteristic was investigated experimentally in Section III and numerically in Section IV.

A. Local zone

The leakage flux enters into the iron core perpendicularly to the core surface, either normal to the lamination plane or in the lamination plane but transverse to the rolling direction. Due to the leakage flux configuration and the material anisotropy, the penetrated flux is constrained within a small volume (Figs. 15 and 17) regardless the flux density and phase angle.

The induced loss associated with ND is eddy current loss and the induced loss associated with TD is the rotational power loss. Compared to the loss in the RD, the eddy current loss and the rotational loss produce much higher per volume loss (i.e. higher loss density), and can therefore lead to local hotspots. This has been confirmed experimentally in Section III.D and numerically in Section IVC, where the eddy current loss increases rapidly with the ND flux density (Fig. 11). More importantly, we found that the phase angle between the RD flux (main flux) and the ND flux also plays a significant role in the eddy current enhancement (Fig. 12).

In literature [21], the influence of the homogenous TD flux on power loss has been investigated experimentally. It concludes that the TD flux can generate significant larger power loss than RD flux of the same level. However, we have demonstrated that, in a lamination structure, the TD flux is constrained within such a small volume (see Fig. 15) that the

associated rotational loss is rather insignificant compared to the eddy current loss induced by the ND flux (see Table II).

B. Global zone

The penetrated flux inside the core lamination is largely dominated by the flux parallel to the main flux (in RD), which circulates along the edge of the core window (Fig. 5, right). This flux path constitutes the global zone. Obviously, the influence region of the global zone is so much larger than the local zone that it has an impact on the overall core loss.

Since the flux involved in the global zone is in RD, the eddy current is limited by the lamination structure and the hysteresis loss dominates the power loss. The hysteresis loss hardly attribute to any local hot spot. Instead, it can considerably increase the overall power losses due to the larger volume it involves, particularly under inductive loading. In Fig. 10, taking the lowest TD flux density (0.2 T) as an example, the incremental loss is 0.2 W when it is in phase with the RD flux (1.6 T). This corresponds to 2.3% of the total frame loss. Considering the actual leakage flux has multiple exposures in a real transformer, the incremental loss could be substantial under inductive loading.

The incremental loss can be estimated based on the reference measurement on the laminated steels. The measured power loss is formulated in terms of Steinmetz's equation:

$$P_{est} = k_s B^n \quad (5)$$

where k_s is a material dependent constant (also incorporating constant frequency), B is the peak flux density, and n is the Steinmetz constant having a value of slightly more than 2.0 for cold rolled laminations [14]. As an approximation, 2.0 is used. Thus, the incremental loss ΔP_{est} can be expressed as:

$$\begin{aligned} \Delta P_{est} &= P_{net} - (\widetilde{P}_m + \widetilde{P}_l) \\ &= k_s (B_m + \Delta B)^2 - \left[k_s B_m^2 + k_s (\Delta B)^2 \right] \end{aligned} \quad (6)$$

where B_m is the peak value of the initial main flux density; ΔB is the incremental flux density. Here, we assume the penetrated flux in the global zone concentrates in a channel with the width equal to the width of the exposure, and thereby the average flux density in the global zone equates the imposed TD leakage flux density B_l . This assumption leads to an under-estimation of the power loss, since the real flux density is inhomogeneous and the power loss is a convex function (see equation (5)) of flux density. Nevertheless, under this assumption, the incremental flux density ΔB can be simply expressed as B_l and the phase difference α between B_m and B_l :

$$\Delta B = B_l \cos \alpha \quad (7)$$

By inserting (7) into (6), we obtain:

$$\begin{aligned} \Delta P_{est} &= k_s (B_m + B_l \cos \alpha)^2 - k_s B_m^2 - k_s B_l^2 \\ &= k_s (2B_m B_l \cos \alpha + B_l^2 \cos^2 \alpha - B_l^2) \end{aligned} \quad (8)$$

At a large phase angle ($\alpha \approx 90^\circ$), the incremental loss becomes a small negative value:

$$\Delta P_{est} \approx -k_s B_l^2 \quad (9)$$

which can be observed in Fig. 10.

At a smaller phase angle ($\alpha \ll 90^\circ$), the first term in (8)

dominates, whereas the last two terms can be omitted, thus

$$\Delta P_{est} \approx 2k_s B_m B_l \cos \alpha \quad (10)$$

Equation (10) implies that the incremental loss is proportional to the main flux density B_m and B_l . This is in line with the measurement results shown in Fig. 10. Furthermore, we can calculate a percentage increase based on (10).

$$\frac{\Delta P_{est}}{P} \% \approx \frac{2k_s B_m B_l \cos \alpha}{k_s B_m^2} \% = \frac{2B_l \cos \alpha}{B_m} \% \quad (11)$$

$$\frac{\Delta P_{est}}{P} \% \stackrel{\alpha=0}{\approx} \frac{2B_l}{B_m} \% \quad (12)$$

Equation (11) and (12) can be used to estimate the loss percentage increase in the global zone due to flux superimposition. For example, the main flux density of 1.6 T superimposed with the leakage flux of 0.2 T leads to a $2 \times 0.2 / 1.6 = 25\%$ increase of power loss relative to the nominal condition (1.6 T) in the global zone. This corresponds to 2.2% of the total frame loss (considering volume ratio), which has a good agreement with the measurement (2.3%).

Little discrepancy at 90° phase angle (in Fig. 10) implies that the conventional no-load (unidirectional) test gives a good estimation on overall core loss in normal operation. However, underestimates the losses under inductive loading.

VI. CONCLUSIONS

The demonstrated combined experimental and numerical approach to determine the nature and importance of multidirectional leakage flux on the magnetic losses in transformer core lamination can be an effective tool for loss analyses.

The results show that the loading angle has a significant impact on the eddy current loss in the local zone as well as the overall power loss in the global zone of the transformer core. A smaller loading angle can aggravate the risk of local overheating and enhances the overall core losses. The conventional no-load test may underestimate magnetic core loss considerably under inductive loading due to ignorance of penetrated leakage flux.

In contrast, the rotational magnetic loss that appears locally has a negligible contribution, regardless of the phase and the magnitude of the superimposed leakage flux density.

ACKNOWLEDGMENT

This work was performed as a part of the project "Thermal Modelling of Transformers" (project number: 255178) funded by the Research Council of Norway, Statnett, Hafslund and Lyse Nett.

REFERENCES

- [1] M. Kozłowski and J. Turowski "Stray losses and local overheating hazard in transformers", CIGRE 1972, pp no. 12-10.
- [2] Y. Liu et al, "Study of the Stray Losses Calculation in Structural Parts for HVDC Converter Transformers Based on the TEAM Problem 21 Family", *IEEE Transactions on Magnetics*, vol. 31, pp. 605-612, 2016.
- [3] S. A. Mousavi, *Electromagnetic Modelling of Power Transformers for Study and Mitigation of Effects of GICs*, Ph.D. dissertation, Royal Institute of Technology, Stockholm, 2015, pp. 194-195.

- [4] *Magnetic materials-Part 2: Methods of Measurement of the Magnetic Properties of Electrical Steel Strip and Sheet by Means of an Epstein Frame*, IEC 60404-2: 2008.
- [5] *Magnetic materials-Part 3: Methods of Measurement of the Magnetic Properties of Electrical Steel Strip and Sheet by Means of a Single Sheet Tester*, IEC 60404-3: 2009.
- [6] S. Zurek, *Characterisation of Soft Magnetic Materials Under Rotational Magnetisation*, 1st ed. CRC Press, London, 2018.
- [7] M. Enokizono, T. Todaka, S. Kanao and J. Sievert, "Two-dimensional magnetic properties of silicon steel sheet subjected to a rotating field," *IEEE Transactions on Magnetics*, vol. 29, no. 6, pp. 3550-3552, Nov. 1993.
- [8] M. Enokizono, T. Suzuki, J. Sievert, and J. Xu, "Rotational power loss of silicon steel sheet," *IEEE Transactions on Magnetics*, vol. 26, no. 5, pp. 2562–2564, Sep. 1990.
- [9] T. Nakata, N. Takahashi, K. Fujiwara and M. Nakano, "Measurement of magnetic characteristics along arbitrary directions of grain-oriented silicon steel up to high flux densities," *IEEE Transactions on Magnetics*, vol. 29, no. 6, pp. 3544-3546, Nov. 1993.
- [10] N. Hihat et al, "Experimental and Numerical Characterization of Magnetically Anisotropic Laminations in the Direction Normal to Their Surface", *IEEE Transactions on Magnetics*, vol. 47, pp. 4517-4522, 2011.
- [11] T. Yagasiwa, Y. Takekoshi, and S.Wada, "Magnetics properties of laminated steel sheet for normal fluxes," *J. Magn. Magn. Mater.*, no. 26, pp. 340-342, 1982.
- [12] W. Wang, A. Nysveen and N. Magnusson, "Eddy Current Loss in Grain-Oriented Steel Laminations Due to Normal Leakage Flux," in *IEEE Transactions on Magnetics*, vol. 57, no. 6, pp. 1-4, June 2021.
- [13] D. Pavlik, D. C. Johnson and R. S. Girgis, "Calculation and reduction of stray and eddy losses in core-form transformers using a highly accurate finite element modelling technique," in *IEEE Transactions on Power Delivery*, vol. 8, no. 1, pp. 239-245, Jan. 1993.
- [14] S. V. Kulkarni and S. A. Khaparde, *Transformer Engineering: Design and Practice*, 1st ed. Marcel Dekker, Inc., New York, pp. 42, 2004.
- [15] W. Wang, A. Nysveen and N. Magnusson, "Apparatus for loss measurements under multidirectional and de-bias flux in electrical steel laminations," *Rev. Sci. Instrument.* vol.91, Issue 8, 2020.
- [16] *Cold-rolled grain-oriented electrical steel strip and sheet delivered in the fully processed state*, Japanese Industrial Standard. JIS C 2553: 2019.
- [17] *Magnetic materials - Part 6: Methods of measurement of the magnetic properties of magnetically soft metallic and powder materials at frequencies in the range 20 Hz to 100 kHz by the use of ring specimens*, IEC 60404-6: 2018.
- [18] J. P. A. Bastos and G. Quichaud, "3D modelling of a non-linear anisotropic lamination," *IEEE Transactions on Magnetics*, vol. 21, no 6, pp 2366-2369, November 1985.
- [19] J. Wang, H. Lin, Y. Huang and X. Sun, "A New Formulation of Anisotropic Equivalent Conductivity in Laminations," *IEEE Transactions on Magnetics*, vol. 47, pp. 1378 -1381, 2011.
- [20] H. Pfützner et al, "Rotational Magnetization in Transformer Cores-A Review", *Transactions on Magnetics*, vol. 47, no. 11, pp. 4523-4533, 2011.
- [21] T. Kochmann, "Relationship between rotational and alternating losses in electrical steel sheets," *Journal of Magnetism and Magnetic Materials*, pp. 145-146, 1996.

Paper V

W. Wang, A. Nysveen and N. Magnusson, "Eddy Current Loss in Grain-Oriented Steel Laminations due to Normal Leakage Flux," *IEEE Transactions on Magnetics*, vol. 57, no. 6, pp. 1-4, June 2021, no. 6301604, doi: 10.1109/TMAG.2021.3069727.

Eddy Current Loss in Grain-Oriented Steel Laminations due to Normal Leakage Flux

Wei Wang¹, Arne Nysveen¹, *Senior Member, IEEE*, and Niklas Magnusson²

¹Electric Power Department, Norwegian University of Science and Technology, Trondheim, NO-7491 Norway

²SINTEF Energy Research, NO-7465 Trondheim, Norway

Leakage flux penetrating laminated iron cores in power transformers and large generators induces eddy current and local loss. Due to the strong magnetic anisotropy of the lamination structure, the penetrating flux tends to saturate the lamination in its plane, even when the incident stray flux density is low. Therefore, the combined effect of anisotropy and nonlinearity has a great impact on the eddy current distribution and the associated power losses. Moreover, the incident normal flux often interacts with the main flux, where the phase angle between the two fluxes may play a significant role. A measurement device is developed to emulate the actual leakage flux in a steel lamination and the power losses are measured at the flux densities of various magnitudes and phases. The measurement results are compared and interpreted by the results obtained from a finite element analysis, where the homogenization approach for material modelling is implemented, taking the combined effect of magnetic anisotropy and the saturation into account.

Index Terms— Eddy current, Finite element analysis, Magnetic anisotropy, Power losses, Saturation magnetization.

I. INTRODUCTION

VARIABLE power production and consumption due to e.g. renewable energy sources and charging of electrical vehicles, lead to new load patterns for power apparatuses. In large transformers and generators, the laminated iron cores close to the windings are exposed to leakage flux. The normal leakage flux penetrating the core perpendicularly to the plane of the lamination induces eddy currents and generates power loss [1]. Hence, the core loss can be load dependent and under certain loads, the excessive local loss may lead to hot spots on the core surfaces, and result in deterioration of the core insulation and degradation of the insulating oil.

In the past decades, several experimental works involving normal flux [1]-[2] have been carried out. Those works focus on material characterization under unidirectional flux in a single sheet. However, the actual normal flux is usually superimposed with the main flux. Depending on the loading condition, the phase angle between the two fluxes varies, which may change the induced eddy current distribution and the associated power losses. The research on power loss behavior under flux superimposition is largely lacking, and so far, no experimental investigation has been made on the effect of the phase angle between multidirectional fluxes on the eddy current loss.

The finite element method (FEM) has been widely used in eddy current calculation for decades. To reduce the computational effort several homogenization approaches for modelling laminated cores have been proposed [3]-[5], which enables a direct calculation of classical eddy current and the associated loss in lamination structures. The loss decomposition method [6] allows for calculation of hysteresis loss and excess eddy current loss that have different frequency

dependency through a post-processing approach.

The primary aim of this paper is the experimental investigation on the loss influence by the normal flux considering actual leakage flux configuration and the flux superimposition of varying phase angle. The physical interpretation of the effects as well as the theoretical calculation was based on finite element analysis, where the homogenization approach was used to calculate the incremental classical eddy current loss. The hysteresis loss and the excess loss were treated together by a post-processing approach. The obtained measured results were compared with the calculated results.

II. ANISOTROPIC MATERIAL DEFINITIONS

In classic homogenization scheme [3]-[4], the lamination structure is treated as a single domain, and the permeability and the electrical conductivity of the domain are defined as tensors. The three diagonal components of the permeability tensor differ in a grain-oriented (GO) material (Fig. 1).

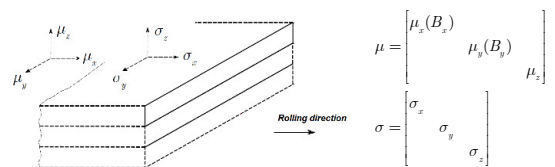


Fig. 1. Illustration of anisotropy of steel lamination. The permeability tensor, μ , and the electrical conductivity tensor, σ , definitions for the lamination of a grain-oriented material.

The effect of the iron-air structure on the permeability in the normal direction, μ_n , is considered by means of a stacking factor γ [4].

$$\frac{1}{\mu_n} = \frac{\gamma}{\mu_f} + \frac{1-\gamma}{\mu_a} \quad (1)$$

where μ_f and μ_a are the permeability of the iron and the air.

Manuscript received November 30, 2020; Corresponding author: Wei Wang (e-mail: weiwang@ntnu.no).

Color versions of one or more of the figures in this paper are available online at <http://ieeexplore.ieee.org>.

Digital Object Identifier (inserted by IEEE).

The average stacking factor is calculated by:

$$\gamma = \frac{m}{\rho V} \quad (2)$$

where m is the weight of the lamination, V is the volume of the lamination; ρ is the mass density of the steel, 7.65 kg/dm^3 . The test lamination is made of cold-rolled GO electrical steel strips (30P120 [7]). The nominal thickness is 0.30 mm with a 10% variation. The calculated stacking factor is 0.97 , thus μ_n is approximately 30 according to (1).

To account for the nonlinearity effect, B - H curves up to the saturation level are required. At least two B - H curves (B_x - H_x curve for $B_y=0$ and B_y - H_y curve for $B_x=0$) shall be used for a grain-oriented material. In our test, the two curves were obtained from the single sheet tests (SSTs) in the rolling direction and the transverse direction, respectively. Multiple samples were measured and the permeabilities (mean value) in two orthogonal directions are presented in Fig. 2.

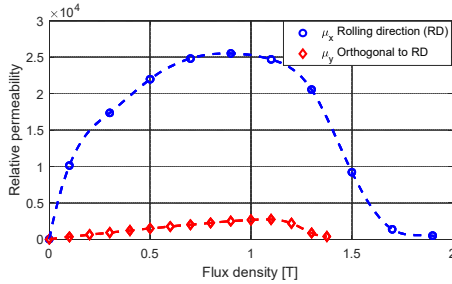


Fig. 2. The components of the permeability tensor versus flux density measured using the single sheet tester (SST). (μ_x : rolling direction; μ_y : orthogonal to rolling direction)

A geometry dependent equivalent electrical conductivity [5] is used in the normal direction.

$$\sigma_n = \left(\frac{\delta}{b}\right)^2 \sigma_f \quad (3)$$

where σ_f is the isotropic conductivity [7] of the GO steels, and δ and b are the thickness and the width of the sheet.

TABLE I

THE PERMEABILITY TENSOR AND THE ELECTRICAL CONDUCTIVITY TENSOR

Relative permeability		Electrical conductivity [S/m]	
μ_x	$\mu_x(B)$ ref. to Fig. 2	σ_x	2.08×10^6
μ_y	$\mu_y(B)$ ref. to Fig. 2	σ_y	2.08×10^6
μ_z	30	σ_z	2.08×10^2

III. EXPERIMENTAL INVESTIGATION

A. Measurement principles and instrument

To emulate the actual leakage flux configuration in the steel lamination exposed to normal flux, we have developed an instrument for loss measurements under multidirectional flux [8]. In the loss measurement system (Fig. 3), the main flux was generated in a square lamination frame with excitation coils and voltage pick-up coils. The normal direction flux was

generated in a C-shaped powder core, in which the flux (with varying magnitude and phase angle) was controlled by the auxiliary excitation coils. The net loss P_{net} in the test specimen is calculated by:

$$P_{net} = P_m + P_m^a - P_{pow} \quad (4)$$

where P_m and P_m^a are the measured power losses from the wattmeter of the main excitation system and the auxiliary excitation system. The measurement reading is obtained with double excitations. The power loss of the C-shaped powder core P_{pow} is calibrated [9] under specified flux densities and frequency prior to fabrication.

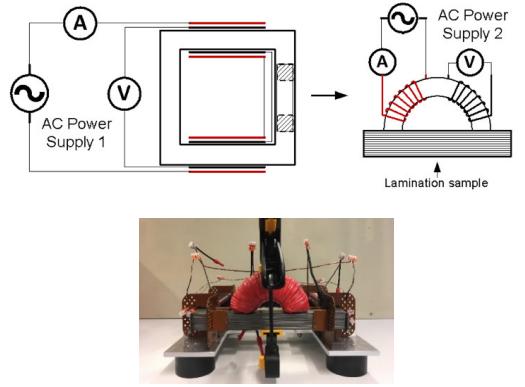


Fig. 3. Loss measurement system with main flux superimposed with leakage flux in the normal direction. The AC power supply 1 connects to the windings wrapping around the square frame and supplies main flux. The AC power supply 2 connects to the winding wrapping around the C-shaped powder core and supplies artificial leakage flux. The C-shaped core is mounted on the surface of the lamination to generate the normal flux. The power source is ITECH IT7627 and the power analyzer is YOKOGAWA WT3000.

B. Measurement under single excitation

The power loss is measured under a single excitation (without main flux in the lamination frame) by the C-shaped powder core. The measurement is performed at 50 and 25 Hz, and the flux density is varied from 0.2 to 0.8 T (Fig. 4). A rapid increase of the power loss with increasing flux density and frequency can be observed.

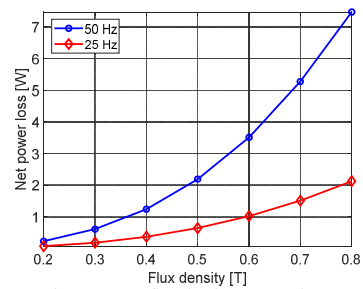


Fig. 4. Net power losses versus flux density measured at 50 and 25 Hz. The measurement is performed under single excitation by the C-shaped powder core.

The loss dependency on flux density B_l and frequency f can be formulated in form of Steinmetz's equation:

$$P \propto f^{1.8} B_l^{2.5} \quad (5)$$

Relation (5) deviates considerably from the classic loss equation where the eddy current loss is proportional to the square of the flux density and square of the frequency.

C. Measurement under multiple excitations

Measurements are performed under multiple excitations with varying phase angle between the main excitation and the auxiliary excitation. The flux density produced in the main frame B_m is set to 1.0 and 1.6 T, whereas the flux density in the C-shaped core B_l is set to 0.2 and 0.4 T. The incremental loss (the difference between the loss measured under superimposed flux and the arithmetic sum of the loss measured with individual excitation systems alone under unidirectional flux) due to flux superimposition are obtained.

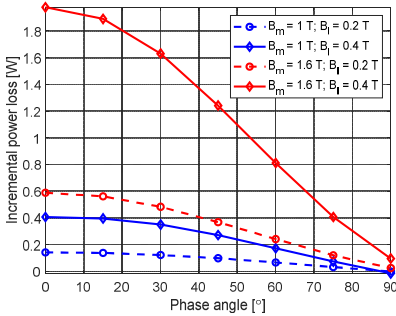


Fig. 5. Incremental power loss versus phase angle measured at different main flux densities B_m combined with different normal leakage flux densities B_l .

As demonstrated in Fig. 5, the power loss increases significantly with increasing flux densities (both the normal flux and the main flux) and with a decreasing phase angle. Apparently, flux superimposition has a greater impact on eddy current loss at a smaller phase angle. In contrast, there is only little discrepancy on loss increase at 90° phase angle.

IV. FINITE ELEMENT ANALYSIS OF EDDY CURRENT LOSS

A. Finite element model

A three-dimensional finite element model (Fig. 6) was developed to investigate eddy current loss in the steel lamination under normal flux as well as the effect of the flux superimposition. The homogenization scheme described in Section II was implemented for the GO. The classical eddy current losses were calculated corresponding to the scenarios illustrated in Sections IIIB and IIIC.

The governing equations for the three-dimensional eddy current field in the steel lamination are expressed in terms of a magnetic vector potential and an electric scalar potential (\vec{A} , φ - \vec{A} formulation).

$$\nabla \times \left[[\mu]^{-1} \nabla \times \vec{A} \right] + [\sigma] \left(\frac{\partial \vec{A}}{\partial t} + \nabla \varphi \right) = 0 \quad (6)$$

$$\nabla \cdot \left\{ -[\sigma] \left(\frac{\partial \vec{A}}{\partial t} + \nabla \varphi \right) \right\} = 0 \quad (7)$$

where $[\mu]$ and $[\sigma]$ are the tensor of the magnetic permeability and the conductivity, which are defined in Table I.

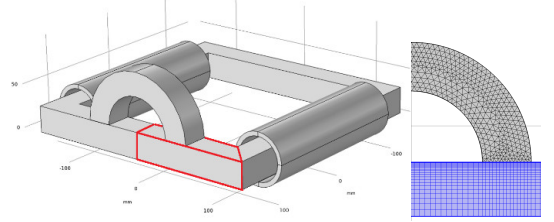


Fig. 6. View of the geometry model and refined mesh in FEM at eddy current concentrated region. In the lamination (blue), the mesh density is growing with geometric sequence towards surface plane. The model was implemented in COMSOL Multiphysics®.

B. Simulation under unidirectional flux

The time-domain simulation was made under the normal flux corresponding to IIB. Figure 7 shows the flux density and the eddy current distribution in the steel lamination at 0.4 T normal flux density. As expected, the majority of the penetrated flux turns to become parallel to the rolling direction and the eddy current induced by the normal flux is constrained within a thin layer (< 3 mm) under the exposure area (interface with C-shaped core).

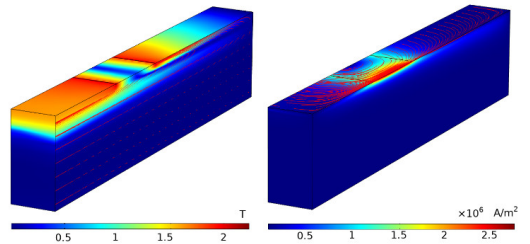


Fig. 7. The flux density (left) and the eddy current (right) distribution in the lamination (a half part of the red region in Fig. 6) at 0.4 T normal flux density. The eddy current is constrained within a thin layer under the exposure area.

The power losses other than the classical eddy current loss are traditionally expressed as hysteresis and excess eddy current loss [6]. The flux density variation in the flux superimposition region influences those losses. We treat these losses together in the post-processing approach. The preserved relationship between this loss and the flux density is obtained from the standardized specific loss measurement [9] performed on the lamination frame.

The simulation result is listed in Table II. To demonstrate the effect of the magnetic nonlinearity, we add linear cases (constant permeability) for comparison to the nonlinear implementation. In the linear simulation, μ_x and μ_y are set to 10000 and 1000, respectively.

TABLE II
POWER LOSS IN THE STEEL LAMINATION DUE TO NORMAL FLUX

Normal flux density [T]	Calculated power loss in the lamination [W]				Measured total losses [W]
	Classical eddy loss	Classical eddy loss	Hysteresis+excess eddy loss	Total power loss	
	$P_{e,n}$ (nonlinear)	$P_{e,l}$ (linear)	P_{hex}	$P_{e,n} + P_{hex}$	
0.2	0.18	0.15	0.06	0.24	0.23
0.3	0.53	0.34	0.11	0.64	0.61
0.4	1.07	0.60	0.16	1.23	1.24
0.5	1.99	0.94	0.21	2.20	2.19
0.6	3.21	1.36	0.27	3.48	3.51
0.7	4.82	1.84	0.33	5.15	5.27
0.8	7.06	2.41	0.39	7.45	7.47

The calculated total power loss by the nonlinear implementation have a good agreement with the measurement, whereas the linear approach largely underestimates the eddy current loss, even at very low flux densities. As expected, the classical eddy loss is strictly proportional to the square of the flux density in the linear case. In the nonlinear case, the eddy loss has a flux density dependency of power 2.5 (larger than 2). Thus, the rapid increase of the eddy loss attributes to the flux saturation effect, which largely extends the eddy current region and amplifies the eddy current loss.

C. Simulation under superimposed multidirectional flux

The simulation is made under superimposed multidirectional flux corresponding to IIC. Figure 8 demonstrates the development of the eddy current region in the lamination with a varying phase angle. The main flux density and the normal flux density are 1.6 T and 0.2 T, respectively.

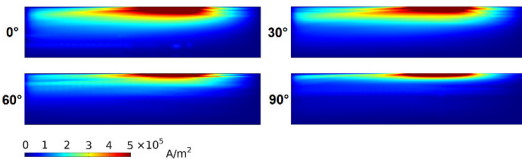


Fig. 8. The maximum eddy current distribution in the lamination under a weak normal flux (0.2 T) superimposed with the main flux (1.6 T) at different phase angles.

The eddy current is more surface concentrated at a larger phase angle (90°), similar to the case without main flux (Fig. 7). In contrast, at a low phase angle, the eddy current region extends deeply due to the saturation effect caused by flux superimposition. The flux superimposition not only expands the classical eddy current loss volume but also enhances the hysteresis loss and excess eddy current losses (Table III).

TABLE III
POWER LOSS DUE TO NORMAL FLUX AND SUPERIMPOSED MAIN FLUX

Phase angle [°]	Calculated power loss in the lamination [W]			Measured total losses [W]
	Classical eddy loss	Hysteresis+excess eddy loss	Total	
	P_e	P_{hex}	$P_e + P_{hex}$	
0	0.43	8.90	9.33	9.39
15	0.42	8.87	9.29	9.37

30	0.39	8.84	9.23	9.29
45	0.35	8.81	9.16	9.17
60	0.30	8.76	9.06	9.05
75	0.26	8.73	8.99	8.92
90	0.25	8.66	8.91	8.83

V. CONCLUSIONS

The classical eddy current loss dominates the local power loss of the GO-steel lamination when the lamination is exposed to a normal flux, and the loss increases with the flux density more rapidly than what traditional formula predicts. The anisotropy of the lamination structure makes the penetrated flux saturate easily, thereby expands the eddy current region. When the normal flux is superimposed with a main flux at a low phase angle, the power loss can be further amplified. Hence, the core loss can be locally load dependent.

Power apparatuses such as transformers are often operated and tested (no-load test) close to 90° loading angle. Under inductive loading (i.e., at smaller loading angle), special attention must be paid to the local heat enhancement in the core lamination exposed to the normal leakage flux.

The physical interpretation of the effects shows that the combined effect of anisotropy and nonlinearity must be considered in eddy current loss calculation involving normal flux, even when the flux density is very weak.

ACKNOWLEDGMENT

This work was performed as a part of the project "Thermal Modelling of Transformers" (project number: 255178) funded by the Research Council of Norway, Statnett, Hafslund and Lyse Nett.

REFERENCES

- [1] T. Booth, H. Pfitzner, "Characteristics of transformer core material for flux normal to the sheet plane," *J. Magn. Magn. Mat.*, vol. 133, pp. 183-186, 1994.
- [2] N. Hihat, K. Komez, E. Napieralska Juszcak and J. P. Lecoate, "Experimental and Numerical Characterization of Magnetically Anisotropic Laminations in the Direction Normal to Their Surface," *IEEE Trans. Magn.*, vol. 47, no. 11, pp. 4517-4522, Nov. 2011.
- [3] V. C. Silva, G. Meunier and A. Foggia, "A 3-D Finite Element Computation of Eddy Currents and Losses in Laminated Iron Cores Allowing for Electric and Magnetic Anisotropy," *IEEE Trans. Magn.*, vol. 31, pp. 2139-2141, May 1995.
- [4] J. P. A. Bastos and G. Quichaud, "3D modelling of a non-linear anisotropic lamination," *IEEE Trans. Magn.*, vol. 21, no. 6, pp. 2366-2369, November 1985.
- [5] J. Wang, H. Lin, Y. Huang and X. Sun, "A New Formulation of Anisotropic Equivalent Conductivity in Laminations," *IEEE Trans. Magn.*, vol. 47, pp. 1378-1381, 2011.
- [6] S. E. Zirkaa, Y. I. Moroza, P. Marketosb and A. J. Moses, "Comparison of engineering methods of loss prediction in thin ferromagnetic laminations," *J. Magn. Magn. Mat.*, vol. 20, pp. 2504-2508, 2008.
- [7] *Cold-rolled grain-oriented electrical steel strip and sheet delivered in the fully processed state*, Japanese Industrial Standard. JIS C 2553: 2019.
- [8] W. Wang, A. Nysveen and N. Magnusson, "Apparatus for loss measurements under multidirectional and de-bias flux in electrical steel laminations," *Rev. Sci. Instrum.*, vol. 91, issue 8, 084705, 2020.
- [9] *Magnetic materials - Part 6: Methods of measurement of the magnetic properties of magnetically soft metallic and powder materials at frequencies in the range 20 Hz to 100 kHz by the use of ring specimens*, IEC 60404-6: 2018.

Paper VI

W. Wang, A. Nysveen and N. Magnusson, “Common and differential mode of dc-bias in three-phase power transformer,” *Journal of Electrical Engineering*, 2022.
<https://doi.org/10.1007/s00202-022-01592-7>



Common and differential mode of dc-bias in three-phase power transformers

Wei Wang¹ · Arne Nysveen¹ · Niklas Magnusson²

Received: 17 February 2021 / Accepted: 9 June 2022
© The Author(s) 2022

Abstract

Dc magnetization due to the geomagnetically induced currents (GICs) and HVDC (High Voltage Direct Current) systems may cause core saturation and result in serious destruction in the transformer performance as well as the power system stability. Based on susceptibility, transformers are classified into different groups. For instance, a three-phase, three-limb transformer is considered less vulnerable to effects of GIC compared to a single-phase or a three-phase, five-limb transformer. However, our study shows that such classifications do not apply to the dc magnetization caused by converter modulation. In this article, we introduce the concept of common mode and differential mode to distinguish dc-bias caused by different mechanisms. Main focus is given on differential mode dc current since it has rarely been reported in any literature. The differential mode dc current was demonstrated by system simulations of classic three-level voltage source converters as well as modular multilevel converter. Detailed experimental investigations were made on a three-phase, three-limb transformer, where the loss impact as well as reactive power consumption were studied. The test shows a significant difference in stray loss between the two modes in three-phase power transformers. Finally, we discuss the effect of delta winding on dc-bias of different modes.

Keywords AC-DC power converters · Dc magnetization · Geomagnetically induced current · HVDC transmission · Transformers · Saturation magnetization

1 Introduction

Geomagnetically induced currents (GICs) [1–4] and HVDC system operation [5–9] are two main causes of dc magnetization in power transformers. It is well known that dc magnetization can lead to half-cycle saturation of the transformer core, and adversely affect the performance of the power transformer as well as the power system [4]. The excessive magnetization current can create hot spots in windings and structural parts [10], increases reactive power absorption and cause voltage instability [11]. In the worst scenario, the destruction of grid transformers [12] and system blackouts [13] may occur due to dc magnetization. To eliminate dc currents, mitigation measures often involve substantial investments such as in dc blocking devices [14] for

GIC or fundamental frequency blocking filters [15] for the converter related dc currents.

GIC is associated with the phenomenon of geomagnetic disturbance (GMD). The coronal mass ejections (CME) originated from the sun interacts with the magnetosphere of the earth and induce a longitudinal quasi-dc potential on the transmission lines, which drives the flow of GICs [4]. The quasi-dc current flow in the ground via the star windings of the grid transformer at the grounded neutral points. Since the directions of the currents in the three phases are identical, those currents are often referred as zero sequence.

HVDC systems can introduce dc currents into power transformers in two ways. The stray dc current due to HVDC electrode operations (monopolar or bipolar operation) can flow into solidly earthed transformers between two substations. This dc current can have two major consequences: saturation of the grounded transformers and corrosion of the ground grid of the station nearest the cathode [8]. Mitigation schemes are extensively discussed in [16].

Another major cause of dc magnetization by HVDC systems is the modulation effect of power converters. A rapid increase in the number of HVDC transmission lines creates

✉ Wei Wang
weiw@ntnu.no

¹ Norwegian University of Science and Technology, NO-7491 Trondheim, Norway

² SINTEF Energy Research, NO-7465 Trondheim, Norway

a situation where ac and dc lines may share the same corridor or even share the same towers [6, 7]. A neighboring ac line can induce a substantial fundamental current onto the dc line. The induced fundamental voltage and current on the dc side of the converter will then transfer to the ac side and appears as a dc-bias [5]. Parameter sensitivity study on the coupling effect has been reported in [7, 17], where the parallel length, separation distance between ac/dc lines, line transposition and ground resistivity are discussed. Literature [17] focuses on VSC-HVDC transmission system, where a frequency domain model is derived for parameter sensitivity study. With the equivalent impedance representation of the network, the factors such as dc capacitors and modulation index are studied analytically.

Since 1989, when the blackout due to GIC occurred in Canada [13], the phenomenon has been drawn significant attention. The guideline [4] has classified power transformers into four groups based on their susceptibility to effects of GIC and has been widely used for selecting or validating power transformers subjected to dc current. However, as comparison, we will demonstrate that the feature of the dc current generated by converter modulation is significantly different from GICs and the stray current introduced by HVDC electrode operations. First, GICs are characterized by a large number of narrow consecutive pulses over a period of hours separated by a few high peak pulses of less than a few minutes duration [4]. In contrast, the dc currents generated by HVDC systems (either by converter modulation or by electrode operation) are mostly constant. Another important difference, which has not been addressed in any literature, is the directions of the dc currents in three phase windings. GICs and the stray dc current introduced by HVDC systems are well known to be of zero sequence, whereas, this is not the case for the dc current generated by converter modulation.

In this article, we investigate the performance of a three phase, three-limb transformer, subjected to different types of dc currents. Main focus will be given on the modulation related dc currents due to the lack of research and understanding of this phenomenon. First, we analyze the modulation effect in voltage source converters (VSCs) and demonstrate the dc current distribution in the three phases. Then, we introduce the concept of common mode and differential mode to distinguish dc-bias of different directions. By experiment, we compare the loss impact as well as reactive power variation in three-phase power transformers of the two modes. Last, we discuss the effect of delta winding on dc-bias of different modes.

2 Modes of dc-bias in power transformers

To distinguish dc currents generated by different mechanisms, we introduce *common mode* (CM) for GICs and stray

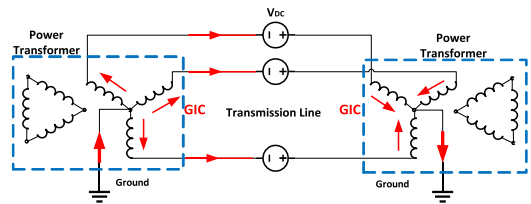


Fig. 1 Geomagnetically induced current distribution in three-phase power system and power transformers

currents, and *differential mode* (DM) for converter modulation related dc current, based on their current directions. System-oriented models are developed to demonstrate dc current introduced by the modulation effect.

2.1 Common mode

The scenario of GIC generation in the network is depicted in Fig. 1. GIC is a quasi-dc current (low frequency, typically 0.01 Hz to 0.5 Hz) that flows in the power system, closing its path through transmission lines, windings and neutral points of grid transformers and ground. Factors that influence the level of GIC include geomagnetic latitude, ground resistivity, network topology and the design of the power transformer. In spite of its destructive impact, high level GICs can hardly sustain over a long period. Often, the peak pulses have time constant less than a few minutes, which is smaller than the thermal time constant of the magnetic core (typically in a range of half hour), but larger than the thermal time constant of the structural steels. Therefore, the thermal issue caused by GIC is mostly related to the hot spots caused by stray flux, not the overall power loss.

Different from GICs, the stray currents are driven by the potential difference between substations due to HVDC electrode operation. That is, the current emanating from the anode partly enters the earth of one substation and flows into the grounded neutrals of the transformer towards the other substation (and the cathode) [8]. Apart from the difference in origination, the stray currents feature a stationary dc current. Therefore, a peak pulse specification is not as crucial as GICs.

Regardless of the differences between the two mechanism, stray dc currents due to HVDC electrode operation are similar to GICs: the dc currents are in the same direction in all three phases. At very low frequencies, the high-voltage network is essentially resistive. Considering the symmetric resistance in three phases, the magnitudes of dc currents in three phases are practically equal. Based on these factors, the GICs and the stray currents are classified as CM.

Several factors determine the susceptibility of the power transformer to CM dc current, such as core topology, winding configuration, and the design of structural parts. Among

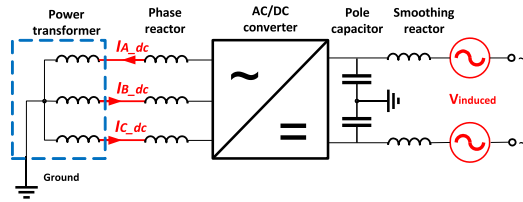


Fig. 2 Fundamental frequency voltage and current on the dc side of the VSC-HVDC converter transfer to the ac side and appear as dc current circulating in the windings of the power transformer

them, the core topology has a major impact on the classification. Single-phase and five-leg core transformers providing low reluctance path for the dc flux, are susceptible to saturation. The three-phase, three-limb transformer, on the other hand, is less susceptible to core saturation due to the high reluctance path for dc flux. In a three-phase, three-limb transformer, the CM flux must pass through the path from the top yoke to the tank top, through the tank walls, and return to the bottom yoke from the tank bottom.

2.2 Differential mode

A dc line in parallel with an ac line is exposed to an inductive coupling. A longitudinal voltage potential of fundamental frequency is induced along the dc line. As depicted in Fig. 2, the induced fundamental frequency voltage and current on the dc side of the converter transfer to the ac side and appear as a dc current (and second-order harmonic) circulating in the windings of the power transformer.

The inductive coupling part is represented as two longitudinal voltage sources in this model. The difference between two voltage sources and the impedance seen from dc side determines the dc current level on the ac bus. Different from CM, the sum of the dc currents appearing on the ac bus is zero. Thus, it is referred as differential mode (DM). As the dc currents are not identical in the three phases, the magnetization of the transformer core becomes non-symmetric. Likewise, the saturation caused by DM dc current can result in excessive heating and an increased noise level in the transformer.

The distribution of the dc currents among the three phases depends on the phase difference between the induced voltage sources and the switching operation. However, this information is not controllable since the two systems do not have to be synchronized. For simplicity, we assume that two fundamental frequency voltage sources u_p and u_n have the same magnitude V_m but are out of phase:

$$\begin{cases} u_p = V_m \cos(\omega_0 t + \theta_0) \\ u_n = -V_m \cos(\omega_0 t + \theta_0) \end{cases} \quad (1)$$

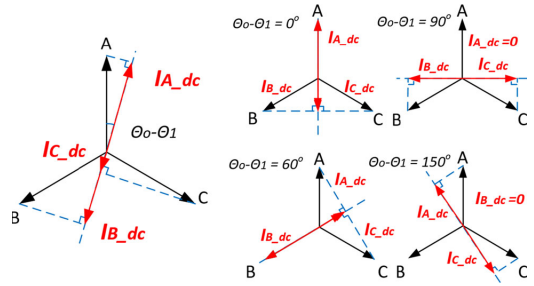


Fig. 3 Phasor representation of the dc component in each phase of the transformer winding due to the modulation effect. $\theta_0 - \theta_1$ determines the magnitudes of dc current in each phase. The scenarios 0° , 60° , 90° and 150° will be investigated in detail

where ω_0 is the fundamental frequency and θ_0 is the phase of the induced voltage source.

The voltage on the ac bus of the converter can be expressed in terms of switching functions [5]:

$$u_{ac} = S_p \times u_p + S_n \times u_n \quad (2)$$

where the switching functions S_p and S_n of the converter are defined as:

$$\begin{aligned} S_p &= \frac{1}{2} \begin{bmatrix} 1 + m \cos(\omega_0 t + \theta_1) \\ 1 + m \cos(\omega_0 t + \theta_1 - \frac{2}{3}\pi) \\ 1 + m \cos(\omega_0 t + \theta_1 + \frac{2}{3}\pi) \end{bmatrix} \\ S_n &= \frac{1}{2} \begin{bmatrix} 1 - m \cos(\omega_0 t + \theta_1) \\ 1 - m \cos(\omega_0 t + \theta_1 - \frac{2}{3}\pi) \\ 1 - m \cos(\omega_0 t + \theta_1 + \frac{2}{3}\pi) \end{bmatrix} \end{aligned} \quad (3)$$

where m is the modulation index and θ_1 is the phase of the switching function.

By inserting (1) and (3) into (2), taking only the dc component of (2) u_{dc} and by simplifying, we obtain:

$$u_{dc} = \frac{m V_m}{2} \begin{bmatrix} \cos(\theta_1 - \theta_0) \\ \cos(\theta_1 - \theta_0 - \frac{2}{3}\pi) \\ \cos(\theta_1 - \theta_0 + \frac{2}{3}\pi) \end{bmatrix} \quad (4)$$

Equation (4) indicates that the relative phase difference between the induced voltage and the switching function of the converter $\theta_0 - \theta_1$ determines the magnitudes in each phase. A phasor interpretation of (4) is described in Fig. 3.

Since the relationship between the phase of induced voltage θ_1 and the phase of the switching function θ_0 is unknown, the magnitudes among three phases varies. To identify the worst case in terms of power losses, we define four scenarios where the phase difference varies from 0 to 150° as illustrated in Fig. 3. Note that the dc current magnitudes of 0° and 90°

Table 1 Dc current defined in each phase of the transformer

$\theta_0 - \theta_1$		Dc current ratio in phase A, B and C				Ref. range [A]
		I_{A_dc}	I_{B_dc}	I_{C_dc}	I_0	
DM	0°	1	- 0.5	- 0.5	0	0.4-1.6
	60°	0.5	- 1	0.5		
	90°	0	- $\sqrt{3}/2$	$\sqrt{3}/2$		
	150°	- $\sqrt{3}/2$	0	$\sqrt{3}/2$		
CM	/	1	1	1	3	0.4-4.0

The applied current in each phase is the multiplication of the current ratio and Ref. range

are the same as 60° and 150°, but distribute in different limbs (the flux path of the middle limb and the side limb are different in a three-phase transformer). To compare the difference between DM and CM, we also define test cases of CM where the dc currents in the three phases are in the same direction. The tests are conducted for a three-phase, three-limb transformer. The ratio and the range of the current applied are listed in Table 1.

In the system study, we made simulations with the setup described in Fig. 2, a classic three-level voltage source converter model and a modular multilevel converter (MMC) [18] model with full control function implemented. The models were built in MATLAB®/Simulink® [19]. The 200 MVA three-level VSC uses Neutral Point Clamped (NPC) topology and Sinusoidal Pulse Width Modulation (SPWM) scheme. On the ac side, the station includes a 230 kV step-down Yg-D transformer and filters. The 150 MVA 12-level MMC levels uses cascaded two-level topology and nearest level control [18]. No filter or smoothing reactor is included in MMC as the harmonic level has been well managed. In both models, the transformers were modeled in a simply way, i.e., tap changers and saturation characteristics were not simulated since the purpose for the simulation was to demonstrate the modulation effect of the power converters. The main circuit parameters for the two converters are summarized in Table 2.

The phase currents on the ac of the converter bus as well as their dc components obtained from the simulations are demonstrated in Fig. 4.

The induced longitudinal fundamental frequency voltage on the dc side causes the unbalanced phase currents on the converter ac buses, as they contain dc component of different levels and directions in each phase. The dc (component) current circulates within three phases and the sum of them must be zero. This modulation effect occurs in both three-level VSC and MMCs, where the dc currents generated in MMCs has less ripple than in three-level VSCs.

Compared to the pulsating nature of GIC, the induced dc current is considered to be more constant (in both direction

Table 2 Main circuit parameters of the converters

Main circuit parameters	Unit	Three-level VSC	MMC
Converter rating	MVA	200	150
System frequency	Hz	50	50
DC voltage	kV	+ /- 100	+ /- 200
AC voltage	kV	230	123
AC filter size	MVar	40	/
Reactance of phase reactor	mH	23.9	50.9
Converter bus voltage	kV	100	123
Transformer rating	MVA	200	150
Transformer leakage reactance	mH	23.9	25.5
Reactance of smoothing reactor	mH	8	/

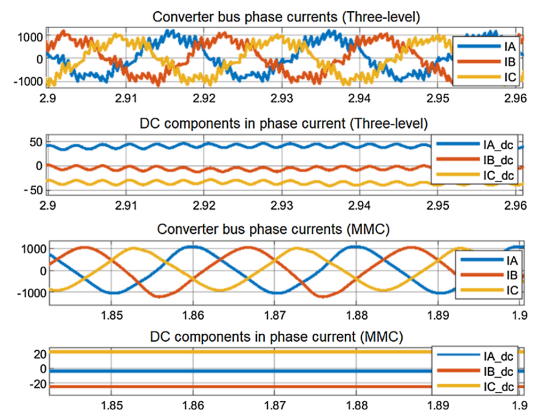


Fig. 4 Phase currents (IA, IB and IC) and their dc components (IA_dc, IB_dc and IC_dc) on the converter ac bus due to harmonic transfer from the dc side. The upper two figures are the result of the three-level VSC and the lower two figures are the result of MMC

and magnitude) as the (phase) regulation of the converter control does not change very often. As a result, a temperature rise can build up in the transformer. Therefore, both the overall power loss (in the core, windings and structural parts) and the located stray loss shall be evaluated for converter modulation related DC magnetization.

Although the mechanism of harmonic transfer is not the scope of this study, we must emphasize the importance of control implementation in the resultant dc current, as it has not been addressed in any literature. Converter internal impedance seen from the dc side is strongly affected by the converter controls and associated bandwidths, particularly in voltage-source converters. For example, the circulating current control (and/or any low-pass active filtering) used in MMCs behaves like a resistor seen from the induced voltage source. Therefore, the dc current derived by the analytical approach [17] without considering control effects may not be valid in practice. Nevertheless, in the following investigation, the dc current level on the ac converter bus is pre-defined and we study the influence of different modes on the power transformer.

3 Test

3.1 Test setup

A 2.5 kVA three-phase, three-limb transformer was used as the test object (Fig. 5), which is connected to the FPGA-based grid emulator (EGSTON®). The EGSTON grid emulator is a 200 kW switching voltage source converter with high bandwidth able to emulate a power system as ac/dc sources. In this test, it is important to program a symmetric ac source with independent, controllable dc components, such that the dc currents are tuned precisely to the predefined values, while the ac voltage is maintained to the nominal values.

Although the phenomenon under investigation is mainly related to grid and distribution transformers, the laboratory transformer is still adopted in our test because:

- The test can be destructive due to extreme saturation condition and excessive losses.
- It is easier to manufacture, modify and assembly iron tank to investigate stray losses.
- The conclusion drawn from a scale-down lab transformer is valid for a larger transformer since the saturation phenomenon is sensitive to materials and dimension ratio, rather than absolute dimensions.

The tank and the clamping plates are made of ordinary carbon steel. The electrical connections are well maintained (no air gap) when connecting the iron plates. The iron tank and the clamping plates can be disassembled such that the

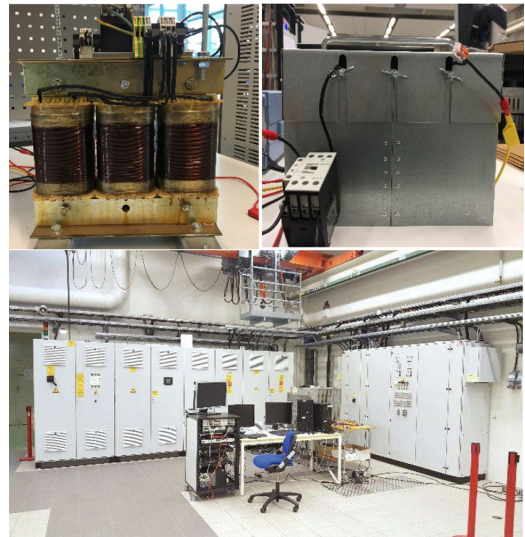


Fig. 5 Test setup. 2.5 kVA three-phase, three-limb transformer for dc-bias test with (upper right) and without (upper left) iron tank. The EGSTON grid emulator (in National Smart Grid Laboratory operated by Norwegian University of Science and Technology and SINTEF Energy) provides controllable voltage source (lower)

core and the stray (in the tank and the clamping steels) losses could be separated. Moreover, the height of the tank (i.e., the distance between the magnetic core and the cover/bottom) was adjustable such that the influence of geometry on stray loss in the tank could be further evaluated.

The number of turns was 280 for both the primary and the secondary windings of the transformer. The primary windings were connected (in star) to a three-phase power converter (three-phase power source, Fig. 6), which provided independent voltage sources for the three phases. The dc voltage bias of each phase was adjusted individually to make the currents reach the predefined values in Table 1. The secondary windings were connected in delta. A switch was used (Fig. 6) such that the impact of open circuit and delta connection could be investigated. No load is connected on the secondary side in the tests (Sect. 3.2, 3.3, 3.4). The current and the voltage in each phase were measured and incorporated into a high precision power analyzer to obtain the power losses and the reactive powers.

3.2 Common mode test

The dc voltage offsets in all three phases were tuned to the same magnitude and direction, where dc currents are CM. The ac nominal voltage ($230 V_{\text{rms}}$) was applied on the primary winding, and the dc voltage offsets were adjusted until

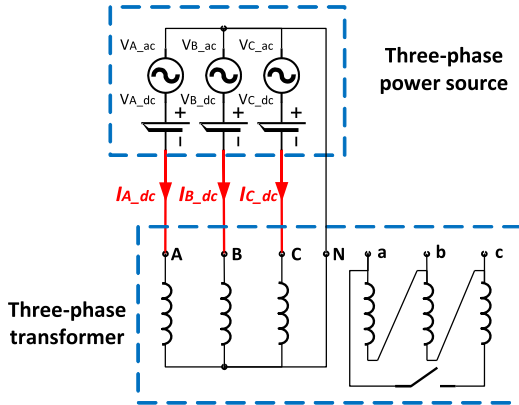


Fig. 6 Transformer winding connection and dc-bias implementation. The primary windings of the transformer were connected to a three-phase power source, where the dc voltage bias of each phase can be tuned. The switch was used to open the secondary delta winding

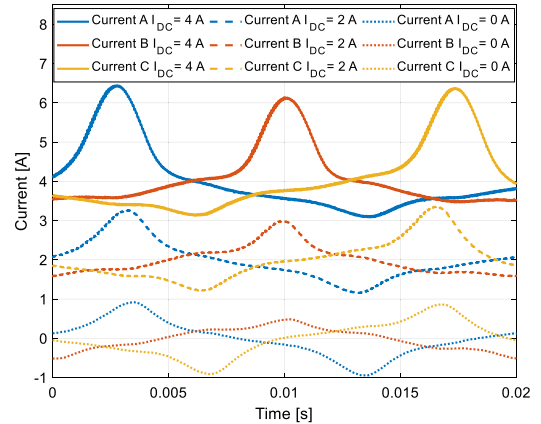


Fig. 7 The measured primary side (magnetizing) currents with different levels of CM dc component

the dc currents reached the preset values in Table 1 (from 0.4 to 4 A).

The measured total power losses consist of core loss, winding loss and stray loss. The winding loss was derived from the obtained current measurement and winding resistance. The core loss was obtained by withdrawing the winding loss from the total loss measured without the tank and the clamping structure. The stray loss was then derived by withdrawing the winding loss and the core loss from the measured total loss. The measurement results are given in Table 3.

The total power loss and the reactive power consumption increase significantly as the dc current increases. Although the core loss constitutes most in the power losses, the majority of the loss increase is from the winding loss, whereas the stray loss increases slightly and the core loss remains almost

constant (the variation < 2%). This confirms the theoretical analysis in Sect. 2.1, namely the three-phase, three-limb transformer has a high reluctance path for the dc flux in CM and it is invulnerable to CM dc current.

Figure 7 shows the measured primary currents over one period at three different levels of dc-bias, i.e., 0 A, 2 A and 4 A. The average current in each phase is equal to the pre-defined dc currents. Without dc-bias (0 A), the average current is zero over a cycle. With dc current, there is a half-cycle asymmetry in the current waveform, which is more notable at 4 A than at 2 A. Moreover, there is an asymmetry in the three phases regardless of the dc current level. This is due to the difference in the reluctance between flux path in phase B (middle) and phase A and C (sides). Nevertheless,

Table 3 Power Losses and Reactive Power due to Dc-bias of CM

DC current [A]	Total losses P_t [W]	Winding loss P_w [W]	Core loss P_c [W]	Stray loss P_s [W]	Reactive power Q [Var]
0	51.02	0.20	50.06	0.76	260
0.4	51.32	0.51	50.05	0.77	386
0.8	52.15	1.31	50.05	0.79	615
1.2	53.33	2.52	50.02	0.81	876.8
1.6	55.04	4.26	49.95	0.84	1140.2
2.0	57.38	6.58	49.93	0.87	1417.7
2.4	60.20	9.36	49.92	0.92	1691.6
2.8	63.57	12.67	49.85	1.06	1971.1
3.2	67.62	16.48	49.81	1.31	2245.4
3.6	72.30	20.93	49.78	1.60	2530.9
4.0	77.54	25.86	49.74	1.95	2813.4

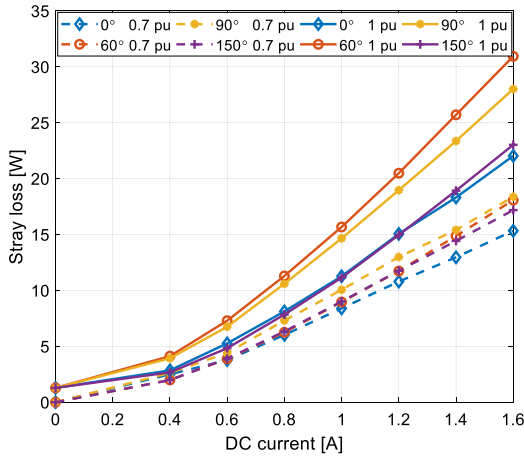


Fig. 8 Stray loss versus dc-bias level under 0.7 p.u. and 1 p.u. ac nominal voltages for four DM configurations

the half-cycle asymmetry in the waveforms of the magnetizing current is rather moderate under the applied CM dc current and transformer core does not reach saturation.

3.3 Differential mode test

The DM dc-bias in the three phases was implemented according to the definition in Table 1. The nominal ac voltage $230 V_{rms}$ (1 pu, corresponding to 1.48 T core flux density) and a lower voltage $161 V_{rms}$ (0.7 pu, corresponding to 1 T core flux density) were applied on the primary winding. The dc voltage offsets were adjusted until the dc currents reached the preset values in Table 1 (from 0.4 to 1.6 A). The power losses and the reactive power assumptions of four configurations were measured. The stray losses and the winding losses are shown in Figs. 8 and 9 respectively. Note that, for all the test cases, the measured core losses remain almost constant ($< 2.5\%$); therefore, they are not demonstrated in detail in the following sections.

Unlike the CM dc current, the stray loss becomes very sensitive to the DM dc current due to the low reluctance path of the dc flux. As seen from Fig. 8, a dramatic loss increase can be observed as the dc-bias increases. In contrast, the power loss under CM dc current of the same levels are order-of-magnitude lower than that of DM.

Furthermore, there is a significant difference in the stray loss among the four configurations. This difference is smaller at lower ac voltage or lower dc current. And, the difference expands as the dc current increases. At the highest dc-bias level (1.6 A), the difference approaches 41% at the nominal ac voltage and 20% at 0.7 pu of nominal ac voltage. The highest stray loss (31 W) occurs when the largest dc current

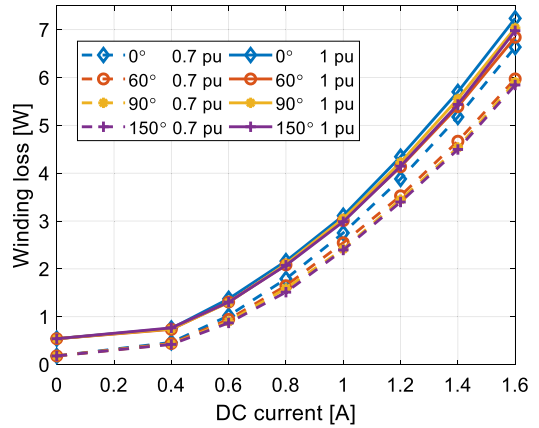


Fig. 9 Winding loss versus dc-bias level under 0.7 p.u. and 1 p.u. ac nominal voltages for four DM configurations

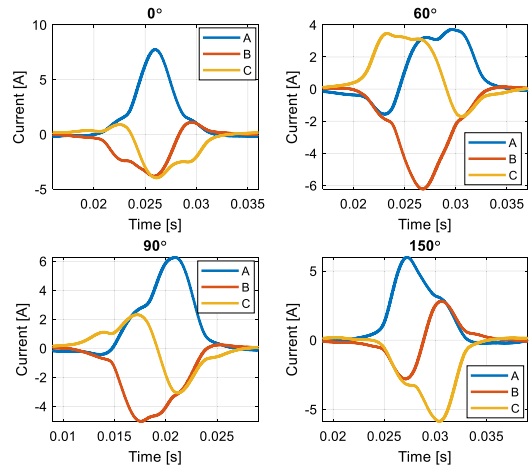


Fig. 10 The measured primary phase currents at different configurations of DM dc currents

is in the middle limb (i.e., 60°) and the lowest loss (22 W) occurs when the largest dc current is in the side limbs (i.e., 0°). The winding loss (Fig. 9) is highest for the 0° case, although the difference is not as notable as the stray losses.

Figure 10 shows the measured primary (magnetizing) currents over one period for the four configurations when the dc current is 1.6 A. Since no current flows in the neutral, the sum of the three-phase currents is zero. The peak values of the currents in DM are significantly larger than that of CM. Among four configurations, the 0° case gives the highest peak current (as well as the highest RMS current) at phase A, resulting in the highest winding loss (Fig. 9).

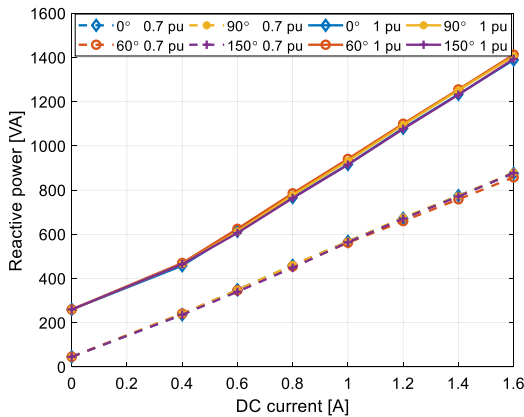


Fig. 11 Total reactive power consumption due to different levels of DM dc currents

Table 4 Reactive Power due to a 1.6 A Dc-bias in DM

Configuration	Reactive power consumption [Var]			
	Phase A	Phase B	Phase C	Total
AC	133.7	83.5	109.1	326.3
0°	658.8	367.7	362.7	1389.2
60°	415.9	588.5	408.7	1413.1
90°	579.0	518.4	308.9	1406.3
150°	547.3	304.4	541.9	1393.6

Compared to the CM dc current, the magnetizing currents of DM have higher amplitudes and shaper spikes (i.e., higher-order harmonic content). Hence, it leads to the higher winding losses.

Different from the rapid increase in power losses (Figs. 8 and 9), the reactive power is practically linear with the dc current (Fig. 11), with little difference between the four configurations.

Although the total reactive power consumption is similar for the four configurations, the reactive power distributions in the three phases are significantly different for each configuration. An example of the reactive power distribution is given in Table 4, for a dc current of 1.6 A. Among the four configurations, the 0° case gives the largest difference between the three phases, which implies the largest voltage imbalance occurring in this scenario. The voltage imbalance (defined as ratio of the negative sequence fundamental voltage and the positive sequence fundamental voltage) of the four DM configurations with respect to different dc current level is shown in Fig. 12. A linear dependence on dc current can be observed and the case 0° gives the largest voltage imbalance.

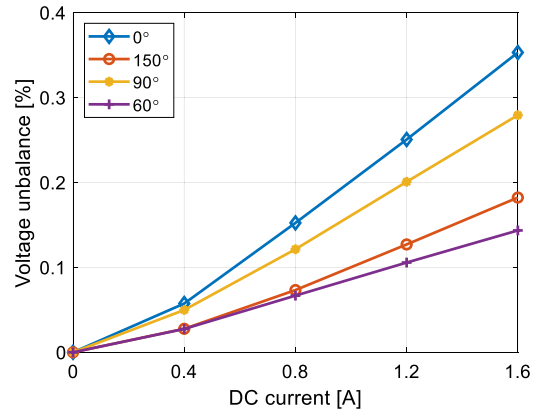


Fig. 12 Voltage imbalance due to different levels of DM dc currents

3.4 Influence of tank and clamping steels

The measurement cases in Section IIIC were repeated after adjustment of the tank and the clamping structure, where the tank height (determined by the distance between the upper yoke and the tank cover and between the lower yoke and the tank bottom, d) was adjusted. Four cases were defined:

- Case 1: $d = 5$ mm.
- Case 2: $d = 20$ mm.
- Case 3: Without tank.
- Case 4: Without tank and clamping plate.

The loss measured in Case 4 equals the core loss (plus winding losses) since no tank and clamping structure were involved. The difference between Case 3 and Case 4 is due to the stray loss from the clamping plates. The difference between Case 1 (or 2) and Case 3 is the stray loss from the tank [20]. The results at a dc current of 1.6 A are given in Table 5.

As expected, both the tank and the clamping structure have a great impact on the stray loss. The loss in those structural parts largely attributes to eddy currents generated in proximity of the magnetic core. Several conclusions can be drawn from Table 5.

- The stray loss in the tank and the clamping plates increases dramatically due to dc-bias. In case 2, for instance, it increases from 1.3 (under pure ac excitation) to 31.3 W (1.6 A dc-bias at 60°).
- Among the four configurations, the stray loss varies considerably. The variations in Case 1 (33%) and Case 2 (37%) are greater than in Case 3 (26%), largely due to the stray loss redistribution in the iron tank.

Table 5 Power Losses due to Dc-bias of DM

Loss type	Configuration	Case number			
		1	2	3	4
Stray loss [W]	AC	1.9	1.3	1.2	0
	0°	32.5	22.8	7.7	0
	60°	43.3	31.3	9.7	0
	90°	40.4	28.7	8.4	0
	150°	34.5	24.3	8.4	0
Winding loss [W]	AC	0.4	0.4	0.4	0.4
	0°	7.2	7.2	7.4	7.7
	60°	6.9	6.8	6.9	7.1
	90°	7.0	7.0	7.0	7.4
	150°	6.9	7.0	7.0	7.3

- The stray loss in the tank is sensitive to the tank height (air gap). The loss increases with more than 10 W (> 40%) when the gap distance reduces from 20 to 5 mm.
- The winding loss increases with dc-bias level. The tank and clamping structures have little impact on winding loss.

In all measurement cases, the tank and the clamping structure have a minor influence (< 5%) on the reactive power.

3.5 Influence of delta winding

Delta connection is widely used in many types of three-phase transformers. Except for being used as a secondary winding, in high rating transformers, a delta connected tertiary winding can be used to reduce the unbalancing currents or to supply an auxiliary load at different voltage levels. The measurement Cases 1, 3 and 4 in Sect. 3.4 were repeated with the secondary winding connected in delta. The results at a dc current of 1.6 A are given in Table 6.

The delta winding significantly reduces the power loss caused by the dc-bias. The majority of the decreased loss is from the stray loss in the tank (> 25 W). Additionally, there is a reduction in the stray loss in the clamping structure (< 4 W), whereas the core loss is practically unchanged. Moreover, with delta winding, the loss difference between the four configurations becomes smaller. The winding loss in the primary side increases slightly with connecting the delta winding, due to the small increased magnetizing current. Last but not the least, in our test, the loss in the delta winding is moderate. However, in practice, attention should be paid to the rating of the delta winding as the induced current might exceed the design value. For instance, a delta winding used as tertiary winding supplying an auxiliary load might not be rated high enough to withstand the induced current caused by high dc bias.

Table 6 Power Losses due to Dc-bias of DM with Delta Winding

Loss type	Configuration	Case number		
		1	3	4
Stray loss [W]	0°	6.3	5.6	0
	60°	5.9	6.3	0
	90°	5.6	5.5	0
	150°	6.1	5.8	0
	Winding loss primary side [W]	0°	7.7	7.8
	60°	7.3	7.3	7.4
	90°	7.4	7.4	7.6
	150°	7.3	7.3	7.4
Winding loss delta [W]	0°	1.7	1.7	0.9
	60°	2.2	2.3	2.0
	90°	2.0	2.0	1.5
	150°	1.6	1.5	0.7

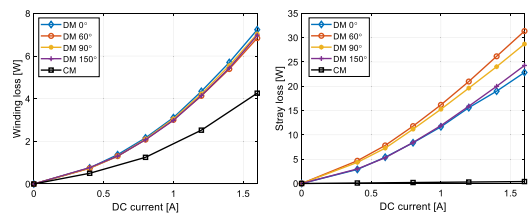


Fig. 13 Winding losses and stray losses due to different levels of DM and CM dc currents. Left: winding losses; Right: stray losses

The measurement were also repeated for CM dc currents. Since the core was not saturated under the applied CM dc current, no significant difference in the losses (core loss, winding loss and stray loss) was observed by adding a delta winding.

4 Discussion

4.1 Comparisons between DM and CM dc current

Comparisons of the power losses for DM and CM dc current are summarized in Fig. 13. Both the winding losses and stray losses of DM are significantly larger than those of CM.

The difference in winding losses can be explained by current total harmonic distortion (THD) of two modes. As an example, in Fig. 14 (DM case 0°), the THD of DM is significantly larger than CM. The harmonic currents account for considerable portion of the winding loss for DM. In contrast, the THD is small and increases very slightly for CM dc current, in which the winding losses is dominated by dc ohm loss. It is also worth noting that the winding losses distribution among three phases can be unbalanced due to asymmetric DM dc current distribution.

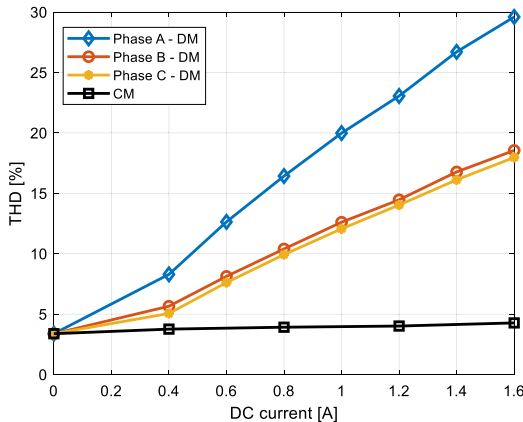


Fig. 14 Current total harmonic distortion (THD) due to different levels of DM and CM dc currents

Detailed harmonic contents due to different levels of DM and CM are presented in Fig. 15. The harmonic current distribution is unbalanced within the three phases for different configurations of DM, which leads to unbalanced winding losses, and more importantly, different stray losses. In contrast, the harmonics of CM are symmetric in the three phases and the magnitudes are much smaller at high frequency.

4.2 Down scaling of transformer

The experiment was carried out on a down-scaled lab transformer, as it is impractical to perform such potentially destructive test on a full-size grid transformer. In principle, the saturation phenomenon is characterized by the flux density in the magnetic core. According to the Ampere's law, the magnetomotive force (defined as NI in ampere-turns) is

$$NI = Hl \quad (5)$$

where N is number of turns, I is current, H is magnetic field strength and l is mean length of the flux path. Then the flux density can be simply expressed by

$$B = \mu H = \mu \frac{NI}{l} \quad (6)$$

where μ is magnetic permeability of the core.

In order to preserve the flux density feature, the down-scaled experiment maintains the same topology of the core and keeps NI/l approximately at the same level as full-scale transformer. It has been seen from the lab test that the transformer performance has been degraded at 1.6 A dc current. Such level of dc current (a few ampere) can cause similar saturation for a transformer with 10^3 times larger rating (full-scale transformer, with the same topology and similar NI/l).

Despite of the similarity in flux density distribution between the lab transformer and full-scale transformer, it is imperative to highlight the important differences between them.

- Large (full-scale) transformers have sophisticated structural steels such as flitch plates close to the magnetic core which are susceptible to the leakage flux affected by saturation.
- The core material used in a grid (full-scale) transformer is often the grain-oriented (GO) steel, which has higher nominal flux density, lower specific loss and steeper magnetization curve below the knee point, compared to the lab (down-scale) transformer which is made of non-grain-oriented (NGO) steel.
- The rated current in a full-scale transformer is much larger than the lab transformer, so the winding loss generated under the same dc current in a full-scale transformer is not as problematic as the down-scaled one, since the percentage current increase (relative to nominal load current) in a full-scale transformer is much less significant.

The grain-oriented steel (typical core material of a grid transformer) often has steeper magnetization curve (i.e., higher permeability) below the knee point and flatter slope above the knee point (i.e., lower permeability). According to Eq. (6), under the same incremental flux (ΔB), higher magnetization current would be induced in the GO material due to its smaller permeability at saturation. This indicates that the magnetization current with GO material has narrower spike (contains higher frequency current harmonics) than the NGO. As a result, the GO material is more sensitive to dc bias, although it is superior in overall core loss reduction.

5 Conclusions

Measurements of power losses and reactive power in CM and DM reveal that there is a significant difference between the two modes of dc currents in three-phase power transformers. Whether a dc current can cause a damage to a power system or a transformer depends on the mode of the dc current.

- Three-phase, three-limb transformer can withstand much higher CM dc current, compared to DM dc current.
- Power transformers are susceptible to DM dc current regardless of their core topologies, due to low reluctance paths and higher flux density offset.
- The magnetizing current under DM dc current has higher THD level than CM and content higher-order harmonics, resulting in both higher stray loss and higher winding loss.
- The core loss is not significantly influenced by the dc-bias. As demonstrated in Table 3, the core loss even decreases

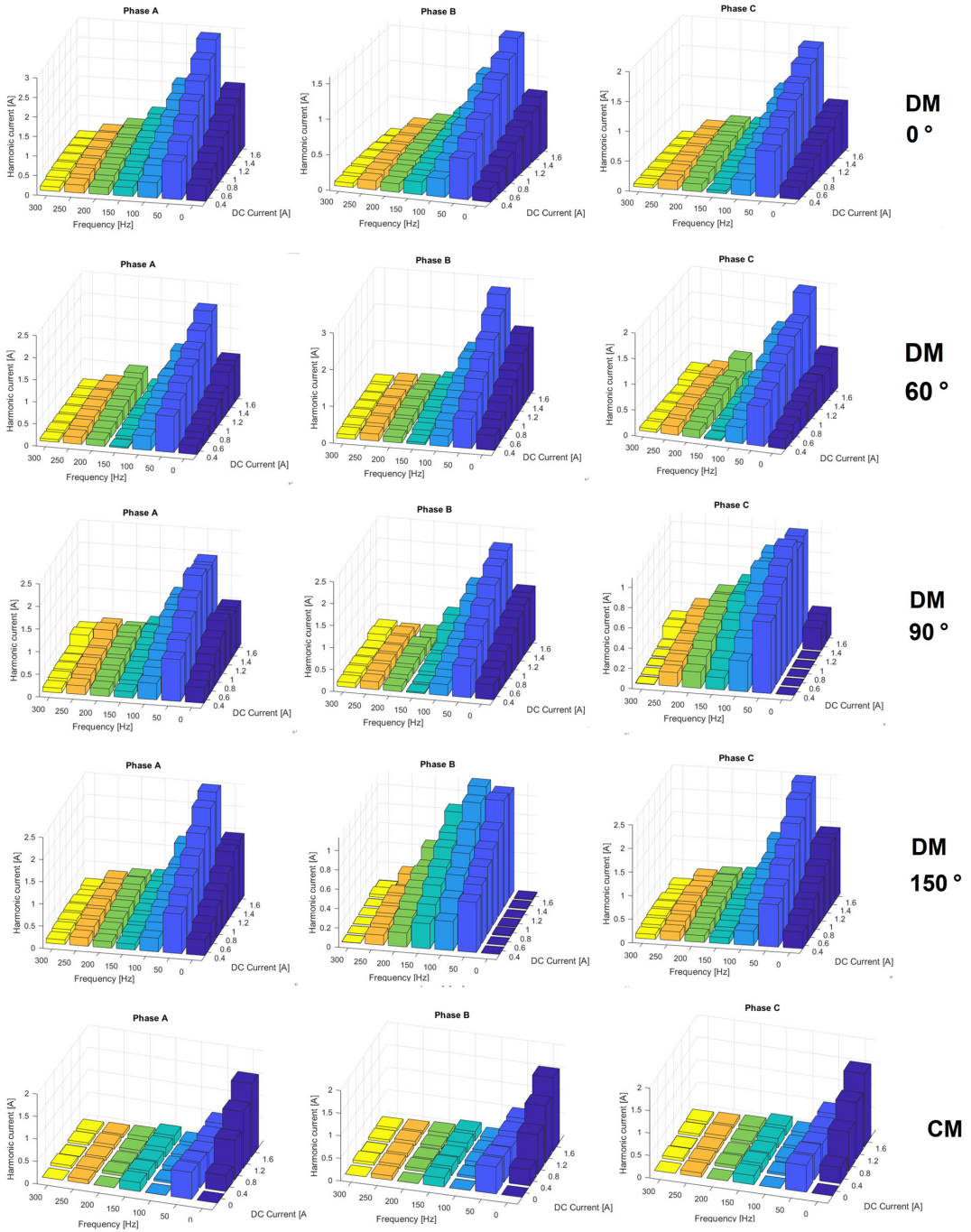


Fig. 15 Current harmonic content due to different levels of DM and CM dc currents

slightly with the dc-bias present, which is in line with the material measurement in [21].

- The power losses caused by high-level DM dc currents depends on dc current distribution in three windings, due to the stray loss redistribution in the iron tank.
- The DM dc currents enhance the reactive power consumption and introduce an unbalanced voltage distribution in the three phases.
- Delta winding can significantly reduce the excessive stray loss (and noise) caused by the DM dc currents, as long as a proper rating is chosen for the delta winding.

The susceptibility classification of power transformers in the guideline [4] applies only to GICs (CM dc currents in general). It is recommended to verify the performance (noise, harmonic distortion, reactive power and/or temperature rise) of a power transformer regardless of its topology, as long as it is exposed to DM dc currents.

Acknowledgements This work was performed as a part of the project "Thermal Modelling of Transformers" (project number: 255178) funded by the Research Council of Norway, Statnett, Hafslund and Lyse Nett.

Funding Open access funding provided by NTNU Norwegian University of Science and Technology (incl St. Olavs Hospital - Trondheim University Hospital).

Open Access This article is licensed under a Creative Commons Attribution 4.0 International License, which permits use, sharing, adaptation, distribution and reproduction in any medium or format, as long as you give appropriate credit to the original author(s) and the source, provide a link to the Creative Commons licence, and indicate if changes were made. The images or other third party material in this article are included in the article's Creative Commons licence, unless indicated otherwise in a credit line to the material. If material is not included in the article's Creative Commons licence and your intended use is not permitted by statutory regulation or exceeds the permitted use, you will need to obtain permission directly from the copyright holder. To view a copy of this licence, visit <http://creativecommons.org/licenses/by/4.0/>.

References


- Price P (2002) Geomagnetically induced current effects on transformers. *IEEE Trans Power Deliv* 17(4):1002–1008. <https://doi.org/10.1109/MPER.2002.4312311>
- Pirjola R (2000) Geomagnetically induced currents during magnetic storms. *IEEE Trans Plasma Sci* 28(6):1867–1873. <https://doi.org/10.1109/27.902215>
- Girgis R, Ko CD (1992) Calculation techniques and results of effects of GIC currents as applied to large power transformers. *IEEE Trans Power Deliv* 7(2):699–705. <https://doi.org/10.1109/61.127070>
- IEEE (2015) IEEE guide for establishing power transformer capability while under geomagnetic disturbances, In: IEEE C57.163 2015
- Jiang Y, Ekström A (1997) General analysis of harmonic transfer through converters. *IEEE Trans Power Electron* 12(2):287–293. <https://doi.org/10.1109/63.558741>
- Larsen EV, Walling RA, Bridenbaugh CJ (1989) Parallel AC/DC transmission lines steady-state induction issues. *IEEE Trans Power Deliv* 4(1):667–673. <https://doi.org/10.1109/61.19259>
- Ulleryd J, Ye M and Moreau G (1998) Fundamental frequency coupling between HVAC and HVDC lines in the Quebec-New England multiterminal system-comparison between field measurements and EMTDC simulations. In: International conference on power system technology (POWERCON). Proceedings (Cat. No.98EX151). <https://doi.org/10.1109/ICPST.1998.729013>
- Rayo J (2017) General guidelines for HVDC electrode design. Cigré working group B4-61
- Gleadow JC, Bisewski BJ and Stewart MC (1993) DC ground currents and transformer saturation on the New Zealand HVDC link In: CIGRÉ international colloquium on high voltage direct current and flexible AC power transmission systems, Wellington, New Zealand
- Mousavi SA (2012) Electromagnetic modelling of power transformers with DC magnetization. Ph.D. dissertation, Dept. Elect. Eng., KTH Royal Institute of Technology, Stockholm
- Bozoki B et al (1996) The effects of GIC on protective relaying. *IEEE Trans Power Deliv* 11(2):725–739. <https://doi.org/10.1109/61.489329>
- Gattens P and Waggel RM (1989) Investigation of transformer overheating due to solar magnetic disturbances. In: IEEE special panel session report
- North American Electric Reliability Council (NERC) (1989) Geomagnetic disturbance. In: North American electric reliability corporation final report, (pp 36–60). www.nerc.com/files/1989-Quebec-Disturbance.pdf
- Kappenman J et al (1991) GIC mitigation: a neutral blocking/bypass device to prevent the flow of GIC in power systems. *IEEE Trans Power Deliv* 6(3):1271–1281. <https://doi.org/10.1109/61.85876>
- Hu JJ and Bisewski B (2011) Evaluation of coupling between dc and ac transmission lines on the same right-of-way: parametric analysis and mitigation methods. In: Minnesota power systems conference (MIPSYCON)
- Faugstad K, O'Brien M, Smith M, Zavahir M (2007) An environmental survey on the operation and impact of HVDC electrode. In: CIGRÉ, Osaka, Japan
- Ding H et al (2011) Analysis of coupling effects on overhead VSC-HVDC transmission lines from AC lines with shared right of way. In: IEEE power and energy society general meeting, MI, USA, 24–28 July 2011. <https://doi.org/10.1109/PES.2011.6038904>
- Sharifabadi K, Hamefors L, Nee HP, Norrga S, Teodorescu R (2016) Design, control, and application of modular multilevel converters for HVDC transmission systems. Wiley-IEEE Press, Chichester
- The Math Works, Inc (2020) MATLAB. (Version 2020a) [Computer Software], <https://www.mathworks.com/>
- Savini A, Turowski J (1988) Electromagnetic fields in electrical engineering. Plenum Press, New York, pp 119–127
- Wang W, Nysveen A, Magnusson N (2020) Apparatus for loss measurements under multidirectional and dc-bias flux in electrical steel laminations. *Rev Sci Instrum* 91(8):084705

Publisher's Note Springer Nature remains neutral with regard to jurisdictional claims in published maps and institutional affiliations.

Paper VII

W. Wang, A. Nysveen and N. Magnusson, "Power losses in three-phase three-limb transformer due to common and differential mode of dc-bias," IET Transaction on Electrical Power Applications, 2021. //doi.org/10.1049/elp2.12113

Power losses in the three-phase three-limb transformer due to common and differential mode of dc-bias

Wei Wang¹  | Arne Nysveen¹ | Niklas Magnusson²

¹Electric Power Department, Norwegian University of Science and Technology, Trondheim, Norway

²SINTEF Energy Research, Trondheim, Norway

Correspondence

Wei Wang, Electric Power Department, Norwegian University of Science and Technology, Elektro E/F, Gloschaugen, O. S. Bragstads plass 2, 7491 Trondheim, Norway.
Email: weiwang@ntnu.no

Funding information

Research Council of Norway, Grant/Award Number: Norges Forskningsråd: 255178

Abstract

Geomagnetically induced currents (GICs) and the converter modulation effect are the two main causes for dc magnetisation in power transformers. It is well known that a small dc-bias can saturate a large transformer and thereby generate high unbalanced magnetising currents, imposing a serious risk of excessive power losses and local overheating. Magnetising currents due to GIC phenomena have been studied extensively, whereas studies on converter related dc-bias are few. In particular, a discussion on loss characteristics related to converter modulation lacks. In this study, the dc-bias of common mode and differential mode in a three-phase, three-limb transformer is investigated experimentally. Additionally, to interpret the physical phenomena, the system was modelled using the finite element method. The results revealed that the power losses are significantly influenced by the dc current direction, arrangement of the structural parts, and the method of winding connection.

1 | INTRODUCTION

DC magnetisation due to geomagnetically induced currents (GICs) [1] and converter modulation [2] may cause core saturation in grid transformers. The dc magnetisation yields high magnetising currents, which increase the noise level in the core and create local hotspots in the winding terminal and in iron structural parts such as the tank and the flitch plates [3, 4]. In the worst case, the generated heat can lead to the full failure of the transformer [5]. Moreover, the excessive magnetising current can deteriorate the performance of the power system [3]. For instance, it increases reactive power consumption, causes voltage instability [6], and the induced current harmonics may lead to incorrect operation of protection relays of HVDC systems, with the risk of tripping the entire transmission system [7].

The GIC originates from the interaction between the coronal mass ejections (CME) of the sun and the magnetosphere of the earth. The electrojet current (generated by the movement of the geomagnetic field relative to the conductive ionosphere) induces a longitudinal quasi-dc potential in series with the transmission lines, driving the flow of induced current, the GIC [3].

Another origin of dc-bias in power transformers is the modulation effect of power converters. When ac and dc

transmission lines share the same corridor or even the same towers [8, 9], the ac line induces fundamental current in the dc lines by inductive coupling. Due to the switching operation of the power electronic converter, the fundamental signal on the dc side of the converter will then be transferred to the ac side and appear as dc-bias (and second order harmonic) [2].

The two mechanisms of dc magnetisation are illustrated in Figure 1. As depicted in the upper figure, the GIC flows through transmission lines and closes its path via the star connected windings of the grid transformer at the grounded neutral points. The GICs are oriented in the same direction in all three phases of the power lines, consequently, in the transformer windings. At very low frequencies (typically 0.01–0.5 Hz), the high-voltage network is essentially resistive. Considering equal resistance in the three phases, the magnitudes of GICs become identical in the three phases. Based on these factors, the GICs are common mode (CM) dominated and causes a zero-sequence magnetising current. In the lower figure, the inductive coupling due to power converter modulation is represented as two longitudinal voltage sources, which determines the dc current level in the transformer windings. Different from GICs, the sum of the dc currents appearing on the ac bus is zero (regardless of whether the transformer is

This is an open access article under the terms of the Creative Commons Attribution License, which permits use, distribution and reproduction in any medium, provided the original work is properly cited.

© 2021 The Authors. *IET Electric Power Applications* published by John Wiley & Sons Ltd on behalf of The Institution of Engineering and Technology.

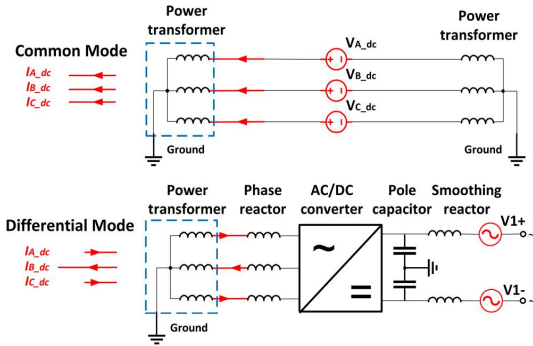


FIGURE 1 Illustration of dc-bias in a three-phase transformer. Upper: the dc-bias is generated by geomagnetic disturbances. The dc current in the transformer winding is of the common mode. Lower: the dc-bias is generated by the converter modulation effect. The dc current in the transformer winding is of the differential mode

grounded or not). Thus, they cannot be in the same direction. These currents are referred to as differential mode (DM).

The GIC phenomenon has been given significant attention and is investigated extensively for decades. The standard [3] has been widely used as a guideline to select or design power transformers subjected to GICs. As for the converter-related dc magnetisation, the physical consequence is similar to GICs in a single-phase transformer, which is used prevalently in large HVDC transmission projects. However, for HVDC projects with constraints in footprint of the converter station (e.g. offshore platform) [10, 11], three-phase transformers are sometimes preferred. In contrast to three single-phase units, where the electromagnetic field is isolated in each phase, the fluxes may interact within the core and structural parts in a three-phase transformer. Such interaction can be significant, particularly when flux saturates the core (due to dc currents).

As the dc currents are not identical in the three phases, it results in unsymmetrical magnetisation of the transformer core. The distribution of the dc voltages, u_{dc} , among the three phases depends on the phase difference, θ , between the induced voltage sources ($V_{1\pm}$ in Figure 1) and the switching operation of the converter [12]:

$$u_{dc} = \frac{mV_m}{2} \begin{bmatrix} \cos \theta \\ \cos\left(\theta - \frac{2\pi}{3}\right) \\ \cos\left(\theta + \frac{2\pi}{3}\right) \end{bmatrix} \quad (1)$$

where m is the modulation index and V_m is the peak voltage on the ac side of the converter. Since θ may take different values, the dc current distribution among the three phases can be largely different under different conditions. Table 1 defines four cases with θ varying from 0° to 150° . For comparison, the CM currents are also included.

The unsymmetrical magnetisation due to the DM dc current in the core may lead to a significantly different

TABLE 1 Examples of dc current ratios defined in each phase of the transformer windings for different phase differences

Mode	θ	DC current ratio in Phases A, B and C			
		$I_{A,dc}$	$I_{B,dc}$	$I_{C,dc}$	$\Sigma I_{ABC,dc}$
DM	0°	1	-0.5	-0.5	0
	60°	0.5	-1	0.5	0
	90°	$\sqrt{3}/2$	$\sqrt{3}/2$	0	0
	150°	$\sqrt{3}/2$	0	$\sqrt{3}/2$	0
CM	/	1	1	1	3

Abbreviations: CM, common mode; DM, differential mode.

physical consequence in terms of losses, noise, and reactive power consumption, which makes the conclusions based on GICs invalid for a three-phase transformer. Understanding the behaviour of the three-phase transformer subjected to DM dc current becomes increasingly important due to recent HVDC projects and has not yet been addressed by any literature. In this study, we experimentally determine the power loss under different cases in a three-phase, three-limb transformer. The influence of dc current directions (CM and DM), the arrangement of the structural parts (tank, clamping plates) and delta connection on the losses are studied for the transformer. To interpret the results and explain the physical phenomena, the transformer is modelled using the finite element method.

2 | EXPERIMENTAL SETUP

2.1 | Test system

A 2.5-kVA three-phase three-limb transformer was used as the test object [12]. Both the primary and the secondary winding had 280 turns. The primary windings were connected (in star) to a three-phase power supply (the FPGA-based grid emulator, EGSTON[®]), with independently controllable phases. The secondary windings were connected in delta and a switch was used to allow the delta connection to be open (Figure 2). The grid emulator is a reconfigurable switching converter being able to emulate a power system as ac/dc sources (100 kVA, 400 V_{ac}/800 V_{dc}). The system offers a symmetric ac source with independent, controllable dc voltages. During the test, the dc currents can be tuned precisely to predesignated values, while the nominal ac voltage is maintained. The primary current and the voltage across each winding were measured in each phase of the transformer, and the measurements were incorporated into a high precision power analyser (YOKOGAWA WT3000), where the power losses were obtained.

The iron tank and the clamping plates (mild steel) can be disassembled such that the core loss, the stray losses of the tank, and the clamping steels can be separated. The height of the tank was adjustable, enabling the influence of geometry on stray loss to be further evaluated (Figure 3).

2.2 | Material measurement on the transformer

The data of the electric steel of a transformer is not always available for the user or even for the transformer designer, particularly when it needs a non-standardised test

such as dc magnetisation. Although standardised material measurement methods for specific power loss [13, 14] as well as specially developed instruments for measurements of losses due to dc bias [15] exist, they cannot always be utilised. Comprehensive measurements are required to cover various combinations of ac and dc magnetomotive force (MMF) and, additionally, the availability of samples can be largely limited.

In a single-phase transformer, the magnetic properties of the electrical steel sheets can be characterised directly on the transformer (ac and dc fields can simultaneously be applied to the core as in [15]). However, for a three-phase transformer, such a standardised test is not applicable since the ac flux and dc flux have different paths in the yoke and the limbs, and the resultant total flux density is non-uniform in the core. In this section, we propose a simple method, which utilises a three-phase transformer to create a uniform flux distribution, and thereby enables a dc-bias test.

The winding connection is represented in the schematic diagram in Figure 4. The primary windings of Phases A and C (two side-limbs) of the transformer are connected in series and excited by a single-phase voltage source. The secondary windings of the Phases A and C are also connected in series and are used as a voltage measurement winding. In this way, the flux along the path l_c in Figure 4 becomes uniform. The ac flux and dc flux have the same path l_c . The flux path l_c comprises the side limbs and yokes. In principle, there is no flux flowing in the middle limb. To verify this, the induced voltage in the middle winding is monitored.

The measured specific power loss (loss per unit mass) versus ac flux density is shown in Figure 5. In all measurements, the induced voltage recorded in the middle limb was less than 1% of the voltage applied on the side limbs indicating that the power loss contributed by the middle limb was negligible. The specific power loss provided by the manufacturer is 1.35 W/kg at 1.0 T (red point in Figure 5), which agrees well with the measurements.

The example of magnetisation characterisation under the dc-bias is demonstrated in Figure 6, where the ac MMF of 1 per-unit (corresponding to 1.48 T) is superimposed with various dc MMFs.

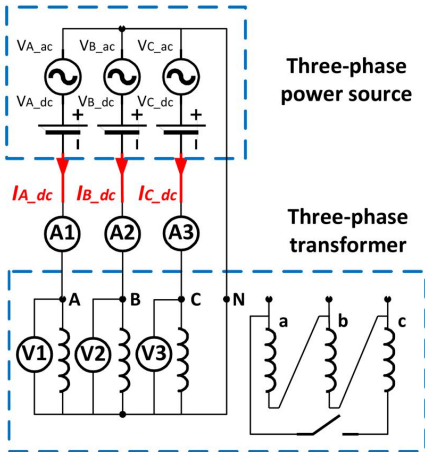


FIGURE 2 Test circuit (transformer winding connection and dc-bias implementation) and the EGSTON grid emulator (controllable three-phase voltage source) in the National Smart Grid Laboratory (NSGL), Norway

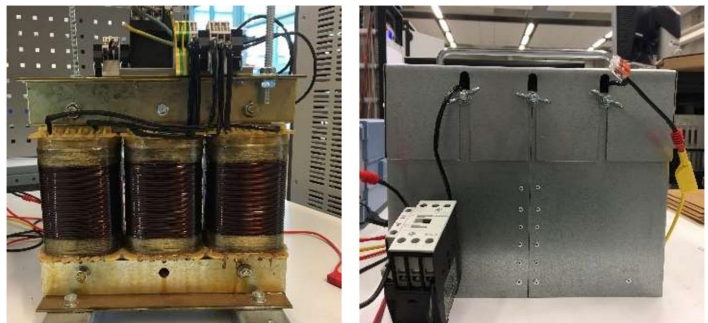


FIGURE 3 The 2.5-kVA three-phase three-limb transformer for dc-bias test

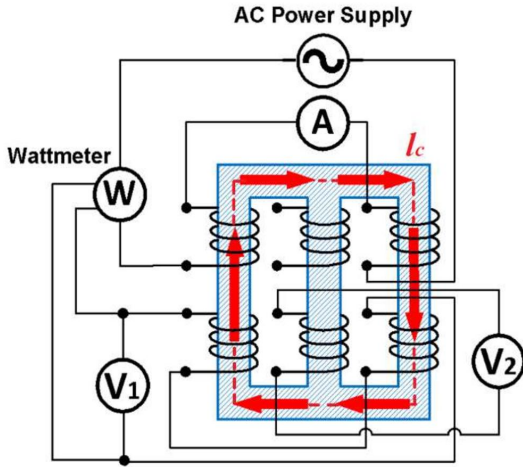


FIGURE 4 Schematic diagram for material magnetisation characterisation using a three-phase three-limb transformer. The dash line l_c and the red arrows represent the flux path in the transformer core. No flux passes through the middle limb. Note that the measurements are performed without tank and clamping steels

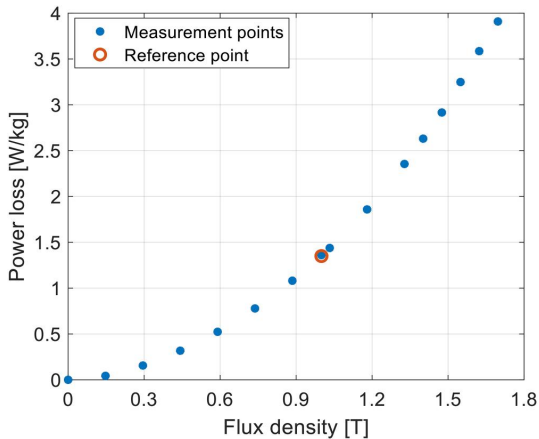


FIGURE 5 Measured specific power loss versus ac flux density. The reference point is given by the manufacturer

The half-cycle saturation is clearly observed from the B - H characteristic in Figure 6. Due to the dc-bias of the flux, the area of the hysteresis loop increases in one half-cycle and decreases in the other half-cycle. For high dc MMFs, the peak flux density exceeds the saturation point in one half-cycle. As a result, a moderate change of the hysteresis loss is expected with the increasing dc MMF. As shown in Figure 7, at low flux density (0.7 pu), the loss increases slightly with dc MMF and asymptotically approaches a constant value. At the nominal flux density (1 pu), the loss decreases slightly as dc MMF increases.

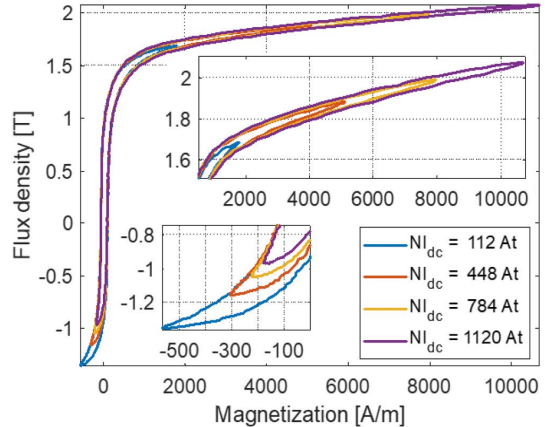


FIGURE 6 Magnetisation characteristic (B - H curve) under ac nominal MMF superimposed with multiple dc-bias levels

3 | FINITE ELEMENT MODELS FOR LOSS CALCULATION

The measured transformer power losses comprise core loss, winding loss, and stray loss, which cannot be easily separated by means of the measurement itself. To gain insight of the constitution and the spatial distribution of the power losses, finite element (FE) models were developed. A two-dimensional (2D) FE model was developed to investigate the core loss and the magnetising current; a three-dimensional (3D) FE model was used to calculate the stray loss (eddy current loss). The geometry of the 2D and 3D models are shown in Figure 8.

The magnetisation characteristic (Figure 9) of the magnetic core was obtained using the approach described in Section 2.2. In normal operation as well as in our test, the leakage flux density is too small to saturate the tank and the clamping plate. Therefore, constant relative permeability (100) was used for the iron tank and the clamping plate (mild steel). The conductivity was 6.99 mS/m.

Transient analyses considering non-linear magnetic properties often require significant computational efforts to obtain steady state solutions. When the problem involves a dc signal, the time constant for reaching steady state, determined by the ratio between the inductance and dc resistance of the winding, becomes extremely large. To deal with such a situation, the time periodic finite element method (TPFEM) [16] and the harmonic balance finite element method (HBFEM) [17] have been proposed. A comparison of the methods is given in [18]. Here, we used 2D TPFEM to calculate magnetising currents and core loss.

The governing equations in terms of a magnetic vector potential A is given by

$$\nabla \times \vec{H} + \sigma \frac{\partial \vec{A}}{\partial t} = \vec{J}_e \quad (2)$$

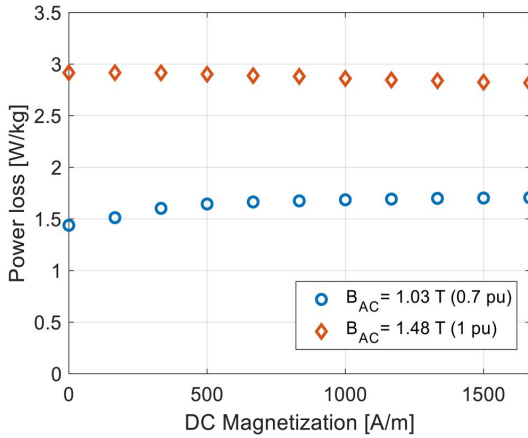


FIGURE 7 Measured specific power loss versus dc magnetisation. Red: nominal ac flux density (1 pu); Blue: low ac flux density (0.7 pu)

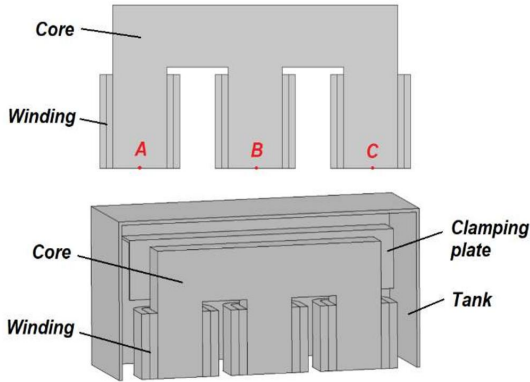


FIGURE 8 Views of the geometry of the FE models. Upper: 2D FE (half) model for core loss calculation. Lower: 3D FE (quarter) model for stray loss calculation

where σ is the conductivity of the material. \vec{J}_e is the periodic excitation current density. When voltage sources are involved (e.g. in 2D FE models), the current density satisfies

$$\vec{J}_e = -\sigma \left(\frac{\partial \vec{A}}{\partial t} + \nabla \Phi \right) \quad (3)$$

where Φ is the electric scalar potential related to the applied voltage sources.

Since saturation is included in the field problem, the magnetic field strength H is a non-linear function of the flux density B

$$\vec{H} = \vec{H}(\vec{B}) = \vec{H}(\nabla \times \vec{A}) \quad (4)$$

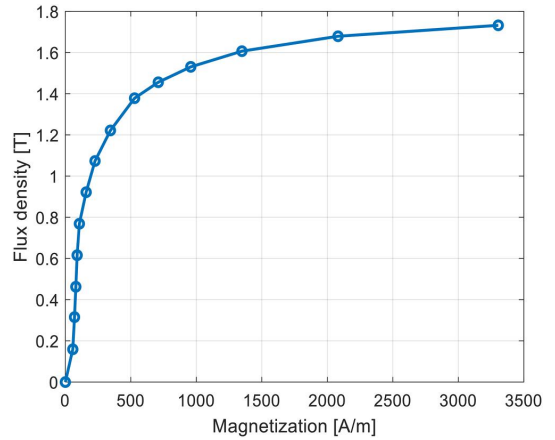


FIGURE 9 Measured magnetisation characteristic (B-H curve) for the transformer core

To implement TPFEM with commercial simulation codes (COMSOL Multiphysics®), the time domain Equation (2) is discretised into multiple coupled stationary problems:

$$\nabla \times \vec{H}(\nabla \times \vec{A}_i) + \sigma \frac{\vec{A}_i - \vec{A}_{i-1}}{2 \frac{T}{N}} = \vec{J}_{e,i} \Big|_{t=\frac{i}{N}T} \quad (5)$$

where T is the period of the excitation and N is the number of the time steps. \vec{A}_i and $\vec{J}_{e,i}$ are the vector potential and excitation current at time step i . Equation (5) represents i discrete equations at specified time instants. A total of 40 points was used in one period in the study.

For the boundary conditions, the symmetric plane (the bottom plane in Figure 8) of the model is defined as a perfect magnetic conductor (i.e. no tangential magnetic field)

$$n \times \vec{H} = 0 \quad (6)$$

Magnetic insulation is defined for the vertical symmetric plane in the 3D model, as well as for the outer boundary of the whole study region

$$n \times \vec{A} = 0 \quad (7)$$

By integration of Equation (3) over the whole coil cross-section and by expressing the electric scalar potential explicitly by means of applied voltage, a set of ordinary differential equations are obtained (following the similar discretisation approach as in Equation 5)

$$\begin{aligned} N_t \cdot \vec{J}_{e,i} - \left[V_{dc} + V_m \cdot \sin\left(2\pi \frac{i-1}{N}\right) \right] \cdot \frac{\sigma}{2l} \\ + N_t \cdot \frac{\sigma}{2} \frac{\int (\vec{A}_i - \vec{A}_{i-1}) ds}{2 \frac{T}{N}} = 0 \end{aligned} \quad (8)$$

where N_t is the number of the turns, l is the out-of-plane depth, and V_{dc} and V_m are the dc voltage offset and the ac voltage amplitude applied, respectively.

With such implementation, the computation time is significantly reduced. When the flux density distribution is obtained, a post-processing approach is adopted to calculate power loss, based on the material measurements made for the P - B relationship, see Figures 5 and 7.

For stray loss analyses involving asymmetric or irregular geometries such as the tank and the clamping plate, 3D modelling must be applied. In 3D FE transient simulations, the obtained magnetising currents are defined as the current excitations [19]. Compared with the voltage source implementation, this requires significantly less memory and thereby saves computation time.

4 | RESULTS AND DISCUSSION

4.1 | Influence of the dc-bias on core loss

Ac nominal voltage (230 V) was applied on the primary winding, where the CM dc currents varied up to 4 A and the DM dc currents varied from 0.4 to 1.6 A. In the tests, the tank and clamping plates were disassembled such that the total power loss only consisted of core loss and winding loss (without stray loss from structural parts). The winding loss was derived from the obtained current and the winding resistance, whereas the core loss was obtained by withdrawing the winding loss from the total power loss.

The test results are presented in Figure 10 (CM dc current) and Table 2 (DM dc current for the four cases in Table 1). The total power loss due to CM currents increased with the dc current. The winding loss dominated the loss increment, whereas the core loss remained practically constant.

A similar behaviour was observed for DM, with the core loss remaining practically constant (with a maximum difference of 2.5%) as dc current increased. However, the winding loss of DM was significantly larger than that of CM at the same dc current level. Among the four different cases in DM, the 0° case gave the highest winding loss, although the difference was small.

Figure 11 shows the measured and calculated primary currents (magnetising currents) for the four DM cases. For comparison, the magnetising current under CM dc current of the same level (1.6 A) is presented. The simulated currents were in good agreement with the measured ones. Due to the ungrounded connection, the sum of the three currents in DM was zero. Although the dc component of the currents was the same (1.6 A), the peak (or harmonic contents) of the DM magnetising currents was significantly larger than that for CM, and thereby induced higher winding loss. Among the four cases in DM, the 0° case gave the highest peak magnetising current (at Phase A) and consequently the highest winding loss.

Figure 12 shows the maximum flux densities in the transformer core. The maximum flux densities are distributed differently in the three limbs for the four DM cases. The

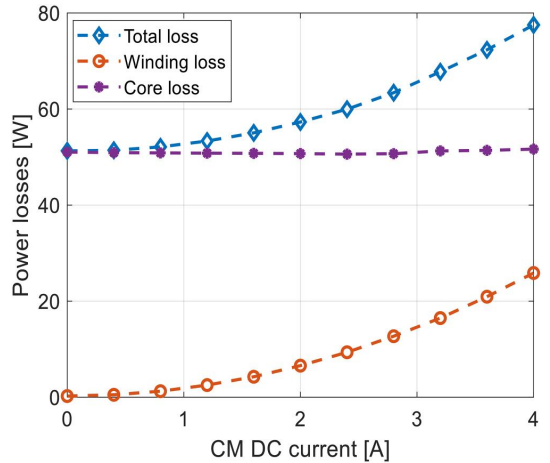


FIGURE 10 Power losses versus dc-bias of CM. The dashed lines are guides to the eye

TABLE 2 Winding losses and core losses due to the dc-bias of DM

DC current (A)	Winding loss (W)				Core loss (W)			
	0°	60°	90°	150°	0°	60°	90°	150°
0.4	0.79	0.79	0.79	0.74	50.0	49.5	49.7	49.8
0.8	2.30	2.16	2.18	2.16	49.8	49.6	49.5	49.5
1.2	4.62	4.28	4.39	4.32	49.5	49.6	49.4	49.1
1.6	7.70	7.13	7.35	7.29	49.3	49.7	49.4	48.8

calculated flux density offsets at the centre of the limbs (at Points A, B, C specified in Figure 8) as well as the calculated core loss are presented in Table 3. The maximum flux densities of DM were significantly higher than those of CM. This difference is due to the fact that the DM flux can close its path inside the core, yielding a smaller reluctance path for the dc flux of DM and a higher flux density offset, whereas the CM flux must close its path outside the core, resulting in a much larger reluctance path and a small flux density offset.

The higher flux densities (or flux density offsets) did not lead to higher core loss. On the contrary, the core loss slightly reduced (Table 2) due to the dc-bias. Despite decreased core loss, the dc-bias produced higher magnetising current and higher winding loss.

The magnetic core in the test transformer is made of isotropic material. As seen from Figure 12, the flux density is not uniform in the corner and joint regions. When anisotropic material (e.g. grain-oriented steel) is used, the flux density would be more uniform throughout the core. More importantly, grain-oriented material often has a much steeper magnetisation curve, which indicates less flux density offset but higher magnetisation current peak under saturation. Therefore, the current harmonic, winding loss and the stray loss are expected to be more pronounced.

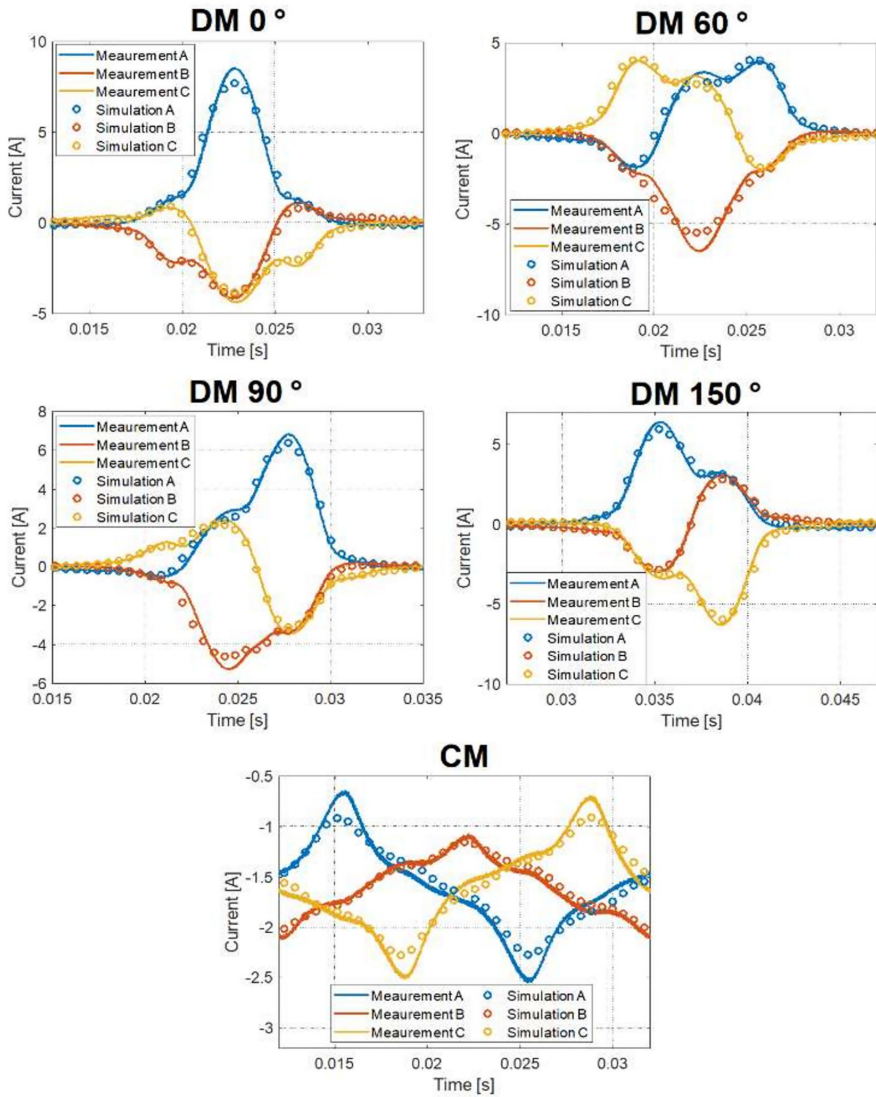


FIGURE 11 Comparison of the measured and calculated primary phase currents over one period at 1.6 A dc current for the four different DM cases and for the CM case. A, B, and C refer to the different positions given in Figure 8

4.2 | Influence of the dc-bias on stray loss

For stray loss investigations, the structural parts were included. The structural parts were added in two steps. First, only the iron tank was added (i.e. the clamping plates were excluded). In this case, the total power loss consisted of core loss, winding loss and the stray loss from the tank. The same ac voltage and dc currents were applied as in Section 4.1, and the winding loss was derived again from the obtained current. As the excitation maintained the same, the core loss was assumed to be identical

to the case without the clamping plate (Section 4.1). Thus, the stray loss could be estimated by withdrawing the winding and core losses from the total loss.

The test results at 1.2 A are presented in Table 4. Both stray loss and winding loss were significantly higher for DM than for CM. The magnetising currents as well as the winding losses remained virtually unchanged when the tank was added. The stray loss differed considerably between the four DM cases, where the 60° case gave the highest loss. The simulated stray loss (i.e. eddy current loss in the tank) waveform over one

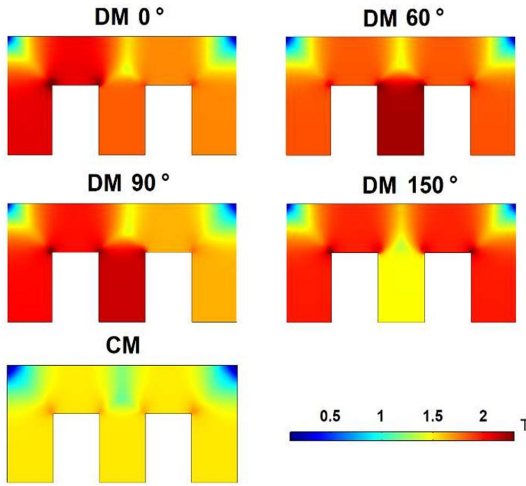


FIGURE 12 The maximum flux density in the magnetic core at 1.6 A dc current for the four DM and the CM cases

TABLE 3 Comparison of flux density offset and core losses due to DC-bias of DM and CM

Mode	θ	Calculated flux density offset in the middle of each limb (T)			Core loss (W) P_c
		ΔB_A	ΔB_B	ΔB_C	
DM	0°	0.61	0.36	0.26	49.4
	60°	0.38	0.75	0.38	49.5
	90°	0.54	0.66	0.14	49.4
	150°	0.51	0	0.51	49.4
CM	/	0.01	0.01	0.01	50.1

TABLE 4 Comparison of power losses with 1.2 A DC-bias in DM and CM

Mode	θ	Measured losses (W)			Calculated stray loss (W)
		Total loss	Winding loss	Stray loss	
DM	0°	59.3	4.5	5.6	6.0
	60°	62.5	4.3	8.6	8.0
	90°	61.4	4.3	7.7	7.0
	150°	58.2	4.3	5.2	5.4
CM	/	52.9	2.5	0.3	0.3

Abbreviations: CM, common mode; DM, differential mode.

period is presented in Figure 13 and the calculated average values are listed in the last column in Table 4. The difference between the calculated stray losses and the measurement likely

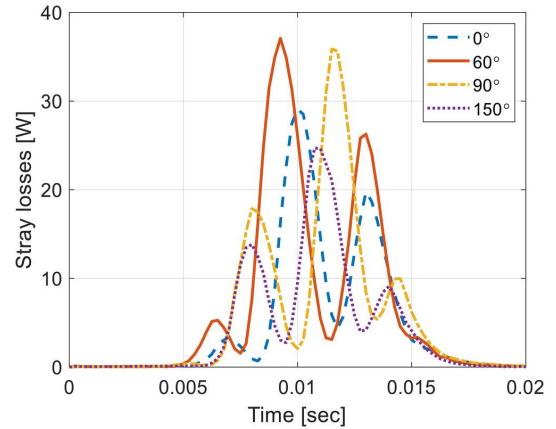


FIGURE 13 The instantaneous stray loss in the iron tank under 1.2 A DM dc current for the four cases. The 0.02 s corresponds to one period

attributes to the neglected geometrical details, such as slots and holes (Figure 3) in the numerical modelling.

Figure 14 shows the maximum stray loss density distribution in the tank for the four cases. The symmetry/asymmetry of the flux density distribution within the core limbs determines the symmetry/asymmetry distribution of the induced stray losses in the tank. For example, at 60° and 150°, the flux density is symmetric with respect to the centre limb (see Figure 12) and so is the loss density (Figure 14). In contrast, at 0° and 90°, the loss concentrates on one side of the tank due to the asymmetric flux density distribution. Among the four cases, the 60° case has the highest magnitude of the loss density, and generates the maximum stray loss.

In the next step, the complete transformer unit was measured (i.e. both tank and clamping plates were included). The stray loss and the winding loss are presented in Figure 15. By including the clamping plates, the stray loss significantly increased. There is a large difference in stray loss between the four DM cases, particularly at higher dc-bias levels. In contrast, the winding losses are almost the same for the four cases.

The stray loss variation and distribution is given for the 60° case in Figure 16. By adding the clamping plates, the total stray loss is increased not only by the added clamping plates, but also by the incremental stray loss in the tank, due to the reduced clearance between the tank and the core. The stray loss of the clamping plates concentrated on the edges close to the winding terminals. The loss concentration area presented in Figures 14 and 16 also indicates the location where the mitigation measures such as a magnetic shunt shall be placed.

4.3 | Influence of delta winding

To evaluate the influence of the delta winding, measurements were made with the secondary winding in delta configuration

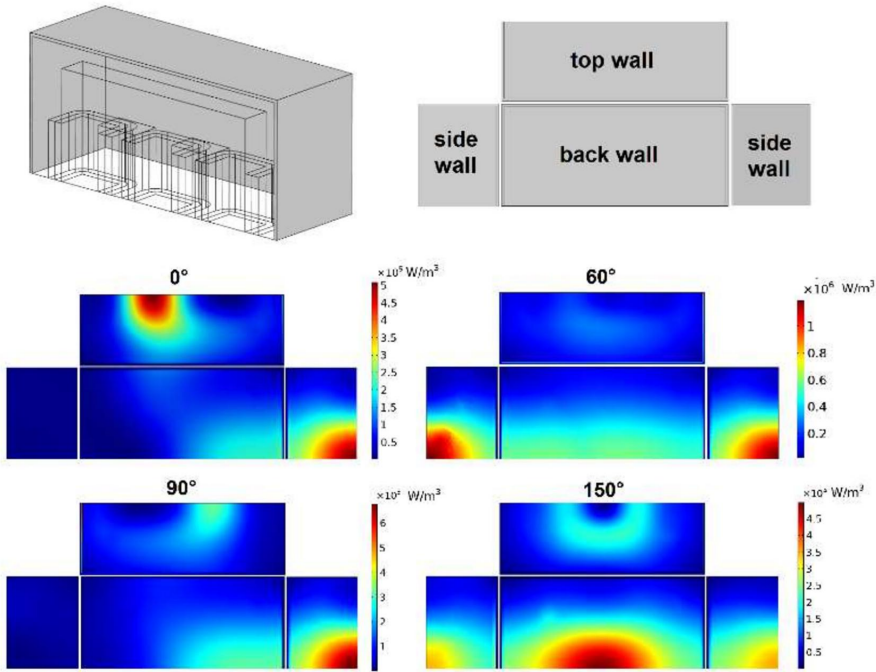


FIGURE 14 The maximum volumetric stray loss density in the tank at 1.2 A DM dc current for the four cases. The upper left figure shows a 3D view of the tank and the upper right figure shows how the tank walls are expanded in a 2D view. One quarter of the model is shown

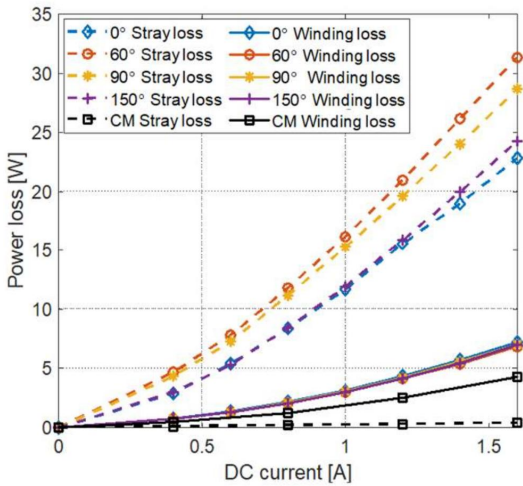


FIGURE 15 Stray loss and winding loss (with both tank and clamping structure) due to DM dc current for the four different cases. For comparison, stray loss and winding loss due to CM are also included

(closing the switch in Figure 2). The stray loss as well as the winding loss at a dc current of 1.6 A are presented in Table 5. As for the previous cases, the winding loss was derived from

the measured current, and the stray loss was estimated by withdrawing the winding loss and the core loss from the total loss.

The delta winding connection resulted in dramatically reduced stray loss (Table 5 compared with Table 4) caused by the dc-bias with the cost of only the modest additional loss in the secondary winding. In addition, the loss difference between the four cases greatly reduced. The simulated example, Figure 17, is given for the 0° case, showing the reduced instantaneous loss with delta winding.

The circulating current in the delta winding was also calculated in the FE analyses, and it was in good agreement with the recorded measured waveform, see Figure 18. The (induced) circulating current counteracted the leakage field generated by the magnetising current, and thereby reduced the stray loss.

5 | DISCUSSION

Traditionally, mitigation measures can be classified into prevention of the creation of GICs and prevention of the transformer core from saturation [20]. The former strategy includes line connected methods [21] and neutral dc blocking devices [22]. For example, a fundamental frequency-blocking filter is used to reduce the fundamental current in the transmission line from inductive coupling, and thereby reduces dc current. A series capacitor can be used to block GICs on line. However, the

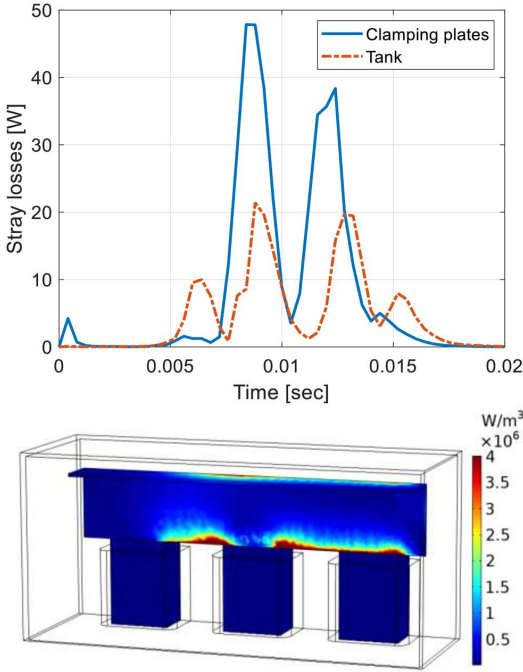


FIGURE 16 The calculated stray loss under DM dc current of case 60°. Upper: the instantaneous stray loss over one period in the tank and the clamping plates. Lower: the maximum volumetric stray loss density in the clamping plates

TABLE 5 Power losses due to DC-bias in DM with delta winding

Mode	θ	Measured power losses (W)		
		Stray loss	Primary winding loss	Secondary winding loss
DM	0°	1.1	4.7	0.6
	60°	0.9	4.4	1.1
	90°	0.9	4.4	0.9
	150°	0.5	4.3	0.5

line connected methods often involve line insulation level and high equipment costs. In contrast, neutral dc blocking devices require much lower voltage rating and less investment. For the counter-saturation strategy, it often suggests using three-phase three-limb transformers to increase reluctance of dc flux [3].

However, for DM dc current, our study shows that the saturation phenomenon is also significant in a three-phase three-limb transformer and that the stray loss can be substantial. Moreover, the neutral blocking device is not a feasible solution since the DM dc current circulates within three phases. Fortunately, most large three-phase transformers used in HVDC link are equipped with delta winding. As discussed in Section 4.3, the

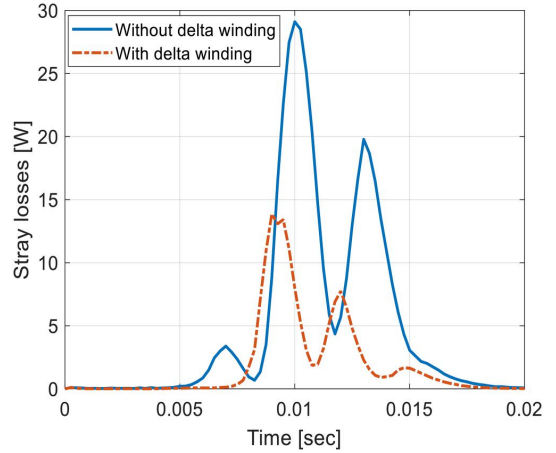


FIGURE 17 The calculated instantaneous stray loss over one period in the tank under 1.2 A DM dc current for the 0° case

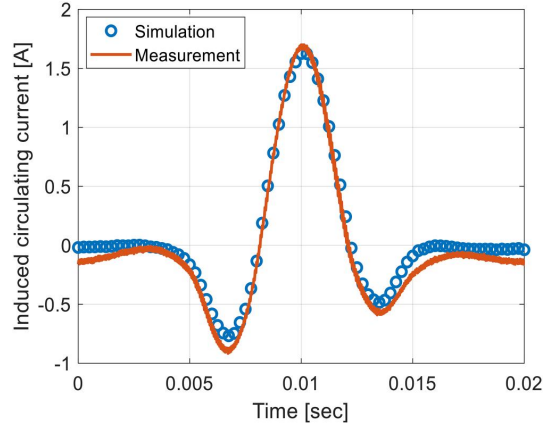


FIGURE 18 Comparison between the calculated circulating current in the delta winding and the measurement over one period in the tank under 1.2 A DM dc current for the 0° case

stray loss can be largely reduced if delta winding exists and proper rating is considered. Otherwise, line connected devices or the control compensation method [23] shall be considered.

6 | CONCLUSIONS

The experimental and modelling study revealed significantly different behaviour in terms of power loss between CM and DM as well as between four DM cases.

- The flux density offset (as well as the maximum flux density) due to DM dc-bias was significantly larger than that in CM (Figure 12 and Table 3), due to the low reluctance path in

DM. Among the four cases, 60° gave the highest offset and thereby the worst case.

- The core loss was not sensitive to dc-bias, regardless of the magnitudes and modes of the applied dc currents (Figure 10 and Table 3).
- The winding loss due to DM dc-bias was significantly larger than that of CM (Table 4 and Figure 15), due to high magnitudes of the magnetising currents as well as their high frequency harmonic contents. For the winding loss, there were only small differences between the different cases.
- The stray losses differed between the four DM cases, where 60° gave the highest loss and 150° gave the lowest loss (Figure 15). The geometry of the tank and the clamping had a dramatic impact on the stray loss.
- The excessive stray loss caused by the DM dc currents was reduced significantly by introducing delta winding (Table 5 and Figure 17).

The results above shows that a three-phase three-limb transformer, which is vulnerable to CM dc currents, is susceptible to DM dc current. The DM dc-bias can constitute a local overheating hazard in the tank and the clamping plates in a power converter connected transformer, particularly if delta winding is not used.

ACKNOWLEDGEMENTS

This work was performed as a part of the project ‘Thermal Modelling of Transformers’ (Norges Forskningsråd project no.: 255178) funded by the Research Council of Norway, Statnett, Hafslund, and Lyse Nett.

CONFLICT OF INTERESTS

The authors declare that there are no conflict of interests.

DATA AVAILABILITY STATEMENT

The data that support the findings of this study are available from the corresponding author upon reasonable request.

ORCID

Wei Wang  <https://orcid.org/0000-0001-6413-2449>

REFERENCES

- Pirjola, R.: Geomagnetically induced currents during magnetic storms. *IEEE Trans. Plasma Sci.* 28(6), 1867–1873 (2000). <https://doi.org/10.1109/27.902215>
- Jiang, Y., Ekström, A.: General analysis of harmonic transfer through converters. *IEEE Trans. Power Electron.* 12(2), 287–293 (1997). <https://doi.org/10.1109/63.558741>
- IEEE guide for establishing power transformer capability while under geomagnetic disturbances, IEEEC57.163 (2015)
- Price, P.R.: Geomagnetically induced current effects on transformers. *IEEE Trans. Power Del.* 17(4), 1002–1008 (2002). <https://doi.org/10.1109/TPWRD.2002.803710>
- Gattens, P., Wagge, R.M.: Investigation of transformer overheating due to solar magnetic disturbances. *IEEE Special Panel Session Report* (1989)
- Bozoki, B., et al.: The effects of GIC on protective relaying. *IEEE Trans. Power Del.* 11(2), 725–739 (1996). <https://doi.org/10.1109/61.489329>
- NERC report: March 13, 1989 geomagnetic disturbances. <http://www.nerc.com/files/1989-Quebec-disturbance.pdf> (1990). Accessed 20 Aug 2020
- Larsen, E.V., Walling, R.A., Bridenbaugh, C.J.: Parallel AC/DC transmission lines steady-state induction issues. *IEEE Trans. Power Del.* 4(1), 667–674 (1989). <https://doi.org/10.1109/61.19259>
- Ulleryd, J., Ye, M., Moreau, G.: Fundamental frequency coupling between HVAC and HVDC lines in the Quebec-New England multiterminal system-comparison between field measurements and EMTDC simulations. In: *International Conference on Power System Technology*, 498–502 (1998). <https://doi.org/10.1109/ICPST.1998.729013>
- Vestergaard, O., Lundberg, P.: Maritime link the first bipolar VSC HVDC with overhead line. In: *AETT HVDC International Conference*, pp. 1–4. (2019). <https://doi.org/10.1109/AETT-HVDC.2019.8740513>
- Sagstad, T.: Power solutions for Johan Sverdrup field in phase 1 and for full field. *Technical Report, Statoil, RE-PM312-00137*. Rev. 1 (2014)
- Wang, W., Nysveen, A., Magnusson, N.: Common and differential mode of dc-bias in three-phase power transformer (2021)
- Magnetic materials-part 2: methods of measurement of the magnetic properties of electrical steel strip and sheet by means of an Epstein frame. IEC 60404-2 (2008)
- Magnetic materials-part 3: methods of measurement of the magnetic properties of electrical steel strip and sheet by means of a single sheet tester. IEC 60404-3 (2009)
- Wang, W., Nysveen, A., Magnusson, N.: Apparatus for loss measurements under multidirectional and dc-bias flux in electrical steel laminations. *Rev. Sci. Instrum.* 91, 084705 (2020)
- Takahashi, Y., et al.: Parallel time-periodic finite-element method for steady-state analysis of rotating machines. *IEEE Trans. Magn.* 48(2), 1019–1022 (2012). <https://doi.org/10.1109/TMAG.2011.2171923>
- Yamada, S., Bessho, K.: Harmonic field calculation by the combination of finite element analysis and harmonic balance method. *IEEE Trans. Magn.* 24(6), 2588–2590 (1988). <https://doi.org/10.1109/20.92182>
- Ausserhofer, S., Biro, O., Preis, K.: Frequency and time domain analysis of nonlinear periodic electromagnetic problems. In: *International Conference on Electromagnetics in Advanced Applications* (2007). <https://doi.org/10.1109/ICEAA.2007.4387279>
- Ngnegueu, T., et al.: Behaviour of transformers under DC/GIC excitation: Phenomenon, impact on design/design evaluation process and modelling aspects in support of design. *CIGRE Session, A2-303* (2012)
- Mousavi, S.A.: Electromagnetic modelling of power transformers for study and mitigation of effects of GICs. *Dissertation, Royal Institute of Technology* (2015)
- Marti, L.: Effects of series compensation capacitors on geomagnetically induced currents. *IEEE Trans. Power. Del.* 29(4), 2032–2033 (2014)
- Wang, Z., et al.: Novel DC bias suppression device based on adjustable parallel resistances. *IEEE Trans. Power. Del.* 33(4), 1787–1797 (2018)
- Trinh, Q.N., Peng, W., Hoong, C.F.: Elimination of DC and harmonic current injection due to grid voltage measurement errors in three-phase grid-connected inverter. In: *IEEE 3rd International Future Energy Electronics Conference and ECCE Asia*, pp. 894–899. (2017)

How to cite this article: Wang, W., Nysveen, A., Magnusson, N.: Power losses in the three-phase three-limb transformer due to common and differential mode of dc-bias. *IET Electr. Power Appl.* 1–11 (2021). <https://doi.org/10.1049/elp2.12113>

ISBN 978-82-326-6658-4 (printed ver.)
ISBN 978-82-326-6345-3 (electronic ver.)
ISSN 1503-8181 (printed ver.)
ISSN 2703-8084 (online ver.)



NTNU

Norwegian University of
Science and Technology